

Laser spectroscopy of fermium isotopes and development of an actinide ion mobility spectrometer

Dissertation

zur Erlangung des Grades

”Doktor der Naturwissenschaften“

im Promotionsfach Chemie

am Fachbereich Chemie, Pharmazie, Geographie und Geowissenschaften
der Johannes Gutenberg-Universität in Mainz

Elisabeth Rickert

geb. in Frankfurt am Main

Mainz, Juni 2023



JOHANNES GUTENBERG
UNIVERSITÄT MAINZ

Dean: personal data

1. Supervisor: personal data

2. Supervisor: personal data

Date of the oral exam: personal data

I hereby declare that I have written this dissertation independently and without any unauthorized outside help, in particular without the help of a doctoral consultant. I have not used any sources other than those indicated and have marked all text passages taken verbatim or in spirit from published or unpublished writings. The dissertation has not been submitted in whole or in part, either in Germany or abroad, in the same or a similar form to an examination authority for the purpose of a doctorate or another other examination procedure. I have not yet completed a doctorate, neither successfully or unsuccessfully.

.....
Place, Date

.....
Elisabeth Rickert

Abstract

Research on heavy and superheavy elements deepens the understanding of the limits of nuclear existence and gives an insight into the underlying structure of the studied atom. Atoms beyond fermium ($Z=100$) owe their existence to nuclear shell effects, which stabilize the nucleus against fission instability evoked by Coulomb repulsion in these proton rich systems. Relativistic effects strongly influence the chemical and physical properties of the heaviest elements, such that these can deviate from the periodicity displayed by the periodic table of elements. Systematic studies on the properties of heavy and superheavy elements are therefore crucial to understand underlying nuclear shell effects and electronic configurations and to benchmark advanced theoretical nuclear and atomic models. However, the experimental access to heavy actinides and transactinides is challenging due to low production yields and often short half-lives. Up to the neutron rich fermium isotope ^{257}Fm , elements can be produced in macroscopic amounts by reactor breeding, while neutron deficient fermium isotopes and elements beyond are usually produced in complete nuclear fusion-evaporation reactions.

To investigate both the electronic and the nuclear structure of an element, laser Resonance Ionization Spectroscopy (RIS) provides a technique, which combines selectivity, sensitivity, and versatility. For spectroscopy on heavy actinides, the RADIATION DETECTED RESONANCE IONIZATION SPECTROSCOPY (RADRIS) method was developed and successfully applied to nobelium. This work covers the laser spectroscopic measurement of the isotope shift of an atomic transition of the fermium isotopes $^{248,249,250}\text{Fm}$ produced online via the α decay of nobelium isotopes. Moreover, isotope shift values obtained from broadband laser spectroscopy on off-line available $^{255,257}\text{Fm}$ are included. Measuring isotope shifts through laser spectroscopy enables the determination of mean-square charge radii (mscr), from which changes in nuclear size and shape can be deduced. The evolution of mscr is extracted on both sides of the deformed neutron shell gap $N=152$. To assess the influence of this gap on the trend of mscr, the experimental data are compared with results of selected nuclear models.

To investigate the electronic structure of actinides, ion mobility spectrometry (IMS) can provide an alternative approach. Previous systematic mobility measurements on monoatomic lanthanide ions revealed the dependence of ion-atom interactions on the underlying electronic configuration and helped to investigate relativistic effects. For an extension of IMS to the actinides, where larger deviations of the configurations from periodicity are expected, an actinide ion mobility spectrometer has been developed within this thesis work. The spectrometer is equipped with a cryogenic drift cell to allow the extraction of ion mobility at varying temperatures and carrier gas pressures. After commissioning, systematic mobility measurements are foreseen on $^{242}\text{Pu}^+$, $^{243}\text{Am}^+$, $^{245}\text{Cm}^+$, $^{249}\text{Bk}^+$ and $^{249}\text{Cf}^+$, where the electronic configuration differs from one another in neighbouring ions. These measurements may provide a deeper insight into the ion-atom interaction potentials of these elements that have not been experimentally addressed so far.

Zusammenfassung

Die Forschung an schweren und superschweren Elementen vertieft das Verständnis für die Existenz von Kernen und deren Grenzen und gibt darüber hinaus einen Einblick in die zugrunde liegende Struktur des untersuchten Atoms. Atome jenseits von Fermium ($Z=100$) verdanken ihre Existenz Kernschaleneffekten, die den Kern gegen die durch Coulomb-Abstoßung hervorgerufene Spaltungsinstabilität in solchen protonenreichen Systemen stabilisieren. Zudem haben relativistische Effekte einen starken Einfluss auf die chemischen und physikalischen Eigenschaften der schwersten Elemente, sodass diese von der Periodizität des Periodensystems der Elemente abweichen können. Systematische Untersuchungen der Eigenschaften schwerer und superschwerer Elemente sind daher von entscheidender Bedeutung, um die zugrunde liegenden Kernschaleneffekte und elektronischen Konfigurationen zu verstehen sowie um Anhaltspunkte für die Weiterentwicklung von Kern- und Atomtheoretischen Modellen zu geben. Der Zugang zu schweren Aktiniden und Transaktiniden ist jedoch aufgrund der geringen Produktionsausbeute und der oft kurzen Halbwertszeit schwierig. Bis zu den neutronenreichen Fermiumisotopen können Elemente in makroskopischen Mengen in Reaktoren erbrütet werden, während neutronenarme Fermiumisotope und schwerere Elemente in der Regel durch vollständige Kernfusions-Verdampfungsreaktionen hergestellt werden.

Um sowohl die elektronische Struktur als auch die Kernstruktur eines Elements zu untersuchen, bietet die Laser-Resonanz-Ionisations-Spektroskopie (RIS) eine modellunabhängige Technik, die Selektivität, Empfindlichkeit und Vielseitigkeit vereint. Für die Spektroskopie an schweren Aktiniden wurde die RADRIS-Methode (RADiation Detected Resonance Ionization Spectroscopy) entwickelt und erfolgreich an Nobelium angewendet. Diese Arbeit umfasst die spektroskopische Messung der Isotopenverschiebung eines Atomübergangs der indirekt on-line erzeugten Fermiumisotope $^{248,249,250}\text{Fm}$. Darüber hinaus werden Isotopieverschiebungswerte von Breitband-Spektroskopie an off-line verfügbaren $^{255,257}\text{Fm}$ einbezogen. Die Messung der Isotopieverschiebungen ermöglicht dabei die Bestimmung der mittleren quadratischen Ladungsradien (mscr), aus denen sich Kerngröße und -form ableiten lassen. Der Verlauf der Ladungsradien wurde auf beiden Seiten der deformierten Neutronenschalenlücke $N=152$ extrahiert. Um den Einfluss dieser Lücke auf die Entwicklung von mscr zu beurteilen, werden die experimentellen Daten mit ausgewählten kerntheoretischen Berechnungen verglichen. Zur Untersuchung der elektronischen Struktur von Aktiniden bietet die Ionenmobilitätspektrometrie (IMS) einen alternativen Ansatz. Frühere Mobilitätsmessungen an monoatomaren Lanthaniden konnten die Abhängigkeit der Ionen-Atom-Wechselwirkungen von der zugrundeliegenden elektronischen Konfiguration offenbaren und ermöglichten die Untersuchung relativistischer Effekte. Für eine Erweiterung der IMS auf die Aktiniden, bei denen größere Abweichungen von der Periodizität zu erwarten sind, wurde im Rahmen dieser Arbeit ein Aktiniden-Ionen-Mobilitätsspektrometer entwickelt. Das Spektrometer ist mit einer kryogenen Driftzelle ausgestattet, welche die Extraktion von Ionen-Atom-Wechselwirkungen bei unterschiedlichen Temperaturen und Gasdrücken

ermöglicht. Nach der Inbetriebnahme sind systematische Mobilitätsmessungen an ${}_{94}^{242}\text{Pu}^+$, ${}_{95}^{243}\text{Am}^+$, ${}_{96}^{245}\text{Cm}^+$, ${}_{97}^{249}\text{Bk}^+$ und ${}_{98}^{249}\text{Cf}^+$ vorgesehen, bei denen sich die elektronische Konfiguration benachbarter Ionen voneinander unterscheidet. Diese Messungen können einen tieferen Einblick in die Ionen-Atom-Wechselwirkungspotentiale dieser Elemente geben, die bisher noch nicht experimentell untersucht wurden.

Contents

1	Introduction	1
2	Theoretical background	5
2.1	Atomic level structure	5
2.1.1	Schrödinger equation ansatz	5
2.1.2	Fine structure	6
2.1.3	Lamb shift	7
2.1.4	Hyperfine structure	7
2.1.5	Isotope shift	8
2.1.6	Magnetic dipole and electric quadrupole moment	9
2.1.7	Relativistic effects on the electronic structure	10
2.2	Nuclear models	11
2.2.1	The Liquid Drop Model	11
2.2.2	The spherical shell model	12
2.2.3	The Nilsson model	13
2.2.4	Shape staggering	14
2.3	Nuclear shell effects	16
2.3.1	Experimental investigation of nuclear shell effects	17
2.3.2	Predictions for shell gaps in the vicinity of $N = 152$	19
2.3.3	Experimental evidence of the $N = 152$ shell gap	21
2.4	Production of nuclei in fusion and separation	23
2.4.1	Fusion evaporation reaction	24
2.4.2	Fusion evaporation production of Fm isotopes	25
2.4.3	Isotope production at SHIP	26
2.5	Laser spectroscopy	27
2.5.1	Atomic transitions	28
2.5.2	Natural linewidth	29
2.5.3	Broadening processes	29
2.5.4	Laser resonance ionization spectroscopy	30
2.5.5	The RADRIS method	32
2.6	Ion mobility spectrometry	33
2.6.1	Diffusion, drift and mobility	34
2.6.2	Gas kinetic theory	35
2.6.3	Ion-neutral interaction potentials	36
2.6.4	The AIMS method	37

Contents

3	Fermium laser spectroscopy	39
3.0.1	RIS studies in the vicinity of $N = 152$	39
3.1	Experimental procedure for fermium laser spectroscopy	42
3.1.1	First laser spectroscopy of ^{255}Fm	42
3.1.2	Indirect production of $^{248,249,250}\text{Fm}$ for RADRIS	44
3.1.3	Laser system of the RADRIS setup	48
3.2	Results for fermium laser spectroscopy	49
3.2.1	Isotope shift measurements of $^{248,249,250}\text{Fm}$	49
3.2.2	Isotope shift values for ^{255}Fm and ^{257}Fm	51
3.2.3	Uncertainties on the centroid position	54
3.2.4	Uncertainties on $\delta\langle r^2 \rangle$	55
3.2.5	Trend in mean-square charge radii $\delta\langle r^2 \rangle$ of $^{248,249,250}\text{Fm}$ and $^{255,257}\text{Fm}$	56
3.3	Consequences of $^{248-250,255,257}\text{Fm}$ spectroscopy results for approved beamtime	62
3.4	Upcoming extension to further Fm isotopes	63
4	Limitations and opportunities of in-gas cell spectroscopy	67
5	The development of an Actinide Ion Mobility Spectrometer	70
5.1	Mobility measurements for electronic-state chromatography	71
5.2	Predictions of the electronic structure of lanthanides and actinides	72
5.3	State-of-the-art ion mobility measurements in lanthanides and actinides	72
5.4	Mobility predictions for singly charged lanthanide and actinide ions	75
5.5	Experimental setup of the ion mobility spectrometer	76
5.5.1	Maintained parts of the old IMS apparatus	77
5.5.1.1	Drift chamber	77
5.5.1.2	Detection section	79
5.5.2	New parts for the AIMS apparatus	79
5.5.2.1	Preliminary considerations	79
5.5.2.2	Developments towards actinide ion mobility spectrometry	81
5.5.2.3	The laser system	83
5.5.2.4	Data acquisition system	85
5.5.2.5	Voltage settings	86
5.5.3	Interim status of AIMS	86
5.6	Possible isotopes for drift measurements	89
6	Summary and outlook	91
7	Appendix	94
7.1	Gate setting for Fm spectroscopy	94

Contents

7.2	Spherical FRDM parametrization for modeling $\delta\langle r^2 \rangle$	95
7.3	Old IMS detection section	96
7.4	Excitation states for selected actinides ($Z=92-100$)	97
	List of Figures	100
	List of Tables	102
	Bibliography	103
	Acknowledgments	131
	Publications	132
	Conferences, Schools and Trainings	132
	Curriculum Vitae	134

Abbreviations and Symbols

Abbreviations

AI	Auto Ionizing state
AIMS	Actinide Ion Mobility Spectrometer
AME	Atomic Mass Evaluation
ATD	Arrival Time Distribution
CE	Conversion Electron
CI	Configuration Interaction
CIPT	Configuration Interaction with Perturbation Theory
CCSD(T)	Coupled Cluster treatment with Singles, Doubles and non-iterative Triples
DAQ	Data Acquisition system
DFT	Density Functional Theory
DM	Droplet Model
EC	Electron Capture
EDF	Energy Density Functional
FRDM	Finite Range Droplet Model
FS	Fine Structure
FSCC	Fock Space Coupled Cluster
FWHM	Full Width at Half Maximum
GSI	Gesellschaft für Schwerionenforschung Darmstadt
HFB	Hartree-Fock-Bogolyubov
HFIR	High Flux Isotope Reactor
HFS	HyperFine Structure
IGRIS	Ion Guide-detected Resonance Ionization Spectroscopy
ILL	Institute Laue-Langevin
IMS	Ion Mobility Spectrometry
IP	Ionization Potential
LDM	Liquid Drop Model
LIF	Laser Induced Fluorescence spectroscopy
LRC	Laser Resonance Chromatography
MBPT	Many-Body Perturbation Theory
MCDF	Multi-Configuration Dirac-Fock
MCSM	Monte Carlo Shell Model
MOT	Magneto-Optical atom Trap
MRCI	Multi-Reference CI
mscr	mean-square charge radii
MS	Mass Shift
NMS	Normal Mass Shift
OES	Odd-Even Staggering
OPO	Optical Parametric Oscillator
ORNL	Oak Ridge National Lab
PIPS	Passivated Implanted Planar Silicon detector

QED	Quantum ElectroDynamics
QMF	Quadrupole Mass Filter
QPIG	QuadruPole Ion Guide
RADRIS	RAdition Detection Resonance Ionization Spectroscopy
RADOP	RAdioactive Decay detected Optical Pumping
RIS	Resonance Ionization Spectroscopy
RISIKO	Resonance Ionization Spectroscopy In COllinear geometry
RFQ	Radio Frequency Quadrupole
RMF	Relativistic Mean-Field
SEM	Secondary Electron Multiplier
SHE	Super Heavy Elements
SHF	Skyrme-Hartree-Fock
SHG	Second Harmonic Generation
SFM	Sum Frequency Mixing
SHIP	Separator for Heavy Ion reaction Products
SMS	Specific Mass Shift
THG	Third Harmonic Generation
TMP	TuboMolecular Pump
UNILAC	UNIversal Linear ACcelerator

Symbols

a	Spin-orbit coupling constant
α	Fine structure constant
A	Atomic mass number
A_{21}	Einstein coefficient for spontaneous emission
A_{HFS}	Magnetic hyperfine coupling constant
B	Magnetic field
B_{12}	Einstein coefficient for absorption
B_{21}	Einstein coefficient for stimulated emission
B_{HFS}	Electric hyperfine coupling constant
β	Deformation parameter
c	Speed of light
C^*	Compound nucleus
D_L	Longitudinal diffusion coefficient
D_T	Transversal diffusion coefficient
Δ	Laplace operator
e	Electron charge
E	Energy
ϵ	Elongation parameter
ϵ_2	Quadrupole deformation parameter
ϵ	Relative kinetic collision energy
ϵ_0	Vacuum permittivity
ϵ_p	Potential well depth

F	Atomic total angular momentum
F_{FS}	Atomic field shift factor
g_I	Landé g-factor
g^l	Orbital gyromagnetic ratio
g^s	Spin gyromagnetic ratio
\mathcal{H}	Hamilton operator
\hbar	Reduced Planck constant $\hbar = \frac{h}{2\pi}$
I	Nuclear spin
$I(\omega)$	Intensity distribution
j	Angular momentum
J	Total angular momentum
K	Ion mobility parameter
K_0	Reduced ion mobility parameter
K	Projection of the nuclear spin upon the symmetry axis
K_{MS}	Atomic mass shift factor
k_B	Boltzmann constant
l	Angular quantum number
λ	Wavelength
m	Magnetic quantum number
m_e	Electron mass
m_p	Proton mass
m_s	Magnetic spin quantum number
μ	Reduced mass
μ_I	Nuclear magnetic moment
μ_K	Nuclear magneton
ν	Frequency
N	Neutron number
N_0	Loschmidt constant
n	Principal quantum number
ω	Angular frequency
$\Omega^{(1,1)}$	Momentum transfer collision integral
Ψ	Wave function
ψ	Wave function
Q	Electric quadrupole moment
Q_α	Alpha decay energy
Q_S	Spectroscopic quadrupole moment
Q_0	Intrinsic quadrupole moment
$Q^{(1)}$	Momentum transfer cross section
r	Position relative to center off mass
R^*	Rydberg Energy
$\langle r^2 \rangle$	Nuclear root-mean-square charge radius
$R_{n,l}(r)$	Radial function
s	Spin quantum number
σ	Cross section
S_{2n}	Two neutron separation energy
S_{2p}	Two proton separation energy

T_{eff}	Effective temperature
$t_{1/2}$	Half-life
τ	Lifetime
θ	Deflection angle in an ion-atom collision
u	Atomic mass unit
$Y_l^m(\vartheta, \varphi)$	Angular spherical harmonics
Z	Proton number

1 Introduction

The periodic table of elements lists to date 118 elements, of which only elements up to uranium ($Z=92$) can be found in appreciable quantities in the earth's crust. The limit of natural abundance lies therefore in the actinides ($89 \leq Z \leq 103$). Elements up to fermium ($Z=100$) can be produced by reactor breeding, while transfermium elements have to be generated either from fusion-evaporation reactions or from nucleon transfer reactions. Hereby, the reaction cross sections decrease with increasing proton number Z while the half-lives shorten. For transfermium nuclei, the Coulomb force of the protons competes against the strong force such that nuclei owe their existence to nuclear shell effects. Analogous to Bohr's electronic shell model, protons and neutrons form shells, whereby the energy spectrum of the nucleons feature large gaps between a filled and the next empty shell [1]. These gaps correspond to the appearance of magic numbers, which are well established at proton and neutron numbers of 2, 8, 20, 28, 50, 82, 128 for spherical nuclei [2]. For heavy elements, deformation of nuclei is well known from experiment and theory [3]. Pronounced deformed neutron shell gaps in the actinides are predicted at $N=152$ and $N=162$ [4]. The $N=152$ shell gap is hereby most pronounced at the proton number $Z=100$ [5]. Investigation on nuclear shell effects can help to pin down the location and extension predicted shell gaps. Thus, experimental measurements can provide a benchmark for nuclear and atomic theory calculations and help to improve the predictions on the location of the "island of stability".

Moreover, the impact of relativistic and Quantum ElectroDynamic (QED) effects increases with Z . Both the nucleus and the electronic shell are affected by that, such that, e.g., the chemical properties of the element may deviate from the naive assumption resulting from their placement in the periodic table. The study of heavy elements can therefore help to understand global atomic properties. One prominent example is the investigation of decay properties of neutron deficient transuranium nuclides, which deepened the understanding of the nuclear deformation and enabled the determination of fission barrier heights [6]. Studying decay properties of superheavy nuclei helps to investigate their underlying nuclear structure explaining the stability and existence of heavy and superheavy nuclei [7].

To investigate the electronic structure and gain insight into nuclear properties like nuclear shape, size, and multipole structure, optical laser spectroscopy has proven to be a powerful, nuclear-model-independent tool [8]. Especially Resonance Ionization Spectroscopy (RIS) is widely used for optical spectroscopy, as

1 Introduction

it is efficient, sensitive, and element selective. Hereby, valence electrons in the atomic shell of the investigated isotope are excited to a resonant intermediate state, before subsequent excitations, which promote the electron beyond the ionization potential. Laser spectroscopy has been thereby applied on a variety of isotopes across the chart of nuclei, from natural occurring isotopes to fission and fragmentation produced to fusion-evaporation produced isotopes. In case of artificial production, ion beam facilities enable on-line access to isotope chains of more than 20 isotopes [8].

Optical laser spectroscopy has thereby proven its power to explore the nuclear structure in different mass regions. For light nuclei between $1 \leq Z \leq 28$, the proton radius puzzle has been tackled by the comparison of a transition study of the Lamb-shift in muonic hydrogen [9] with elastic electron-proton scattering [10]. Moreover, halo nuclei have been substantiated by charge radii increase due to weakly bound neutrons close to the neutron drip line [11]. For medium mass nuclei between $28 \leq Z \leq 82$, shape effects like odd-even staggering caused by a coupling between the proton density and the neutron pair density in ${}_{72}\text{Hf}$ [12] and ${}_{80}\text{Hg}$ [13] were investigated by spectroscopy. Rapidly changing nuclear structure was established in the ${}_{40}\text{Zr}$ region by the study of spectroscopic quadrupole moment Q_S and the change in mean-square charge radii, $\delta\langle r^2 \rangle$, revealing shape transitions at $N=50$ and $N=60$. In heavy nuclei, shape coexistence has been revealed [14]. Recently, optical spectroscopy was successfully applied to nobelium ($Z=102$) in single-atom-at-a-time quantities with the RADIATION DETECTION RESONANCE IONIZATION SPECTROSCOPY (RADRIS) technique [15], [16], opening the path towards laser spectroscopy experiments of the heaviest elements.

Investigation on nuclear shell effects by laser spectroscopy in the region of the actinides can help to gain knowledge on the nuclear structure [17]. Hereby, particularly the change in root-mean-square charge radius $\delta\langle r^2 \rangle^{A'A}$, which can be obtained from isotope shift measurements, has demonstrated its sensitivity to shell effects [8]. Within the framework of this thesis, isotope shift measurements have been performed with the RADRIS technique on the on-line accessible neutron deficient fermium isotopes ${}^{248,249,250}\text{Fm}$ and changes in $\delta\langle r^2 \rangle^{A'A}$ have been extracted. To assess the influence of the $N=152$ shell gap on $\delta\langle r^2 \rangle^{A'A}$, additional isotope shift values have been extracted from the off-line accessible neutron rich isotopes ${}^{255,257}\text{Fm}$, which have been investigated through spectroscopy in a hot cavity ion source.

The atomic and electronic structure are very complex for the actinides [18] and need further investigation. One alternative approach to learn about the chemical properties of heavy elements is the use of ion mobility studies, which give an insight on the electronic configuration and the ion-neutral interaction potential of the studied ion. Moreover, ion mobility studies could provide an alternative way to overcome limitations of the RADRIS technique, which is the state-of-the-art approach for laser spectroscopy on heavy elements [19]. For RADRIS, the isotope of interest is produced by fusion-evaporation reactions. The products pass the

1 Introduction

velocity filter SHIP and are thermalized in a buffer gas cell. After neutralization on a filament, the atoms are re-evaporated for resonance ionization spectroscopy, before the resulting ion is finally guided to a detector. The spectroscopic resolution is hereby limited by the pressure broadening in the buffer gas environment, which is needed for the thermalization of the heavy elements. Furthermore, the transport time of the resonantly ionized isotopes to the detector is limited by the mobility of the ions in the buffer gas. Hereby, the drift velocity is proportional to the ion mobility parameter K , which can be different for different ion species, from macroscopic objects to monoatomic samples. It is convenient to exploit Ion Mobility Spectrometry (IMS) for sample preparation purposes, since it presents a simple, fast, compact, low-cost and moreover highly sensitive, versatile tool [20], that is already established in different areas in analytics.

It is applicable for samples in all aggregate states. Volatile organic compounds from environmental samples can be studied by commercially available IMS devices, e.g., for environmental, process and forensic analysis. Liquid samples can be ionized by, e.g., electrospray ionization, while bulk, solid samples such as soil are made available by vaporization or laser ablation. For life sciences, IMS is widely used for the study of proteins, DNA, sugars etc. Even bacteria can be investigated by mobility studies. Furthermore, the mobility of molecular and elemental ions can be obtained for fundamental research. For molecular ions, the mobility is sensitive to the size and shape of the drifting species. In case of monoatomic ions, the mobility can give insights on the interaction potential of the ion while interacting with the neutral gas atoms. Ion mobility measurements help therefore to assess ion-neutral interaction potentials and give a benchmark for *ab-initio* calculations [21]. Moreover, the mobility is sensitive to the electronic configuration of the drifting species. Especially the change from one to another electron subshell leads to deviations in mobility, as observed in the lanthanide series for ${}_{64}\text{Gd}^+$, which exhibits an occupied $5d$ shell that many other lanthanide ions lack [22]. Even the distinction between meta stable and ground states of the same ion is possible with IMS [23].

In the actinides, relativistic effects have an influence on the valence electrons. While inner $s_{1/2}$ - and $p_{1/2}$ electrons are contracted towards the atomic core, they screen the nuclear potential such that outer lying d and f orbitals expand. Since the electronic structure is very dense [24], the actual and relativistic level ordering may alter from a non-relativistic one [25]. Systematic mobility studies on monoatomic actinide ions may therefore pave the way towards the assignment of electronic configuration of transactinides [26].

After a brief theoretical introduction in Ch. 2, this thesis focuses in Ch. 3 of on-line optical spectroscopy of indirectly produced ${}^{248,249,250}\text{Fm}$ using the RADRES technique. Isotope shift measurements are used to extract the change in m_{scr} . Moreover, broadband scans from the off-line accessible neutron rich isotopes ${}^{255,257}\text{Fm}$ are included to get a measure on the change in $\delta\langle r^2 \rangle^{A'A}$ due to the crossing of the $N=152$ shell gap. The limitations of the used in-gas spectroscopy

1 Introduction

are discussed in Ch. 4. In Ch. 5, the development of an Actinide Ion Mobility Spectrometer is presented. The set-up will be able to perform systematic mobility measurement on various actinide ion species for varying temperatures and carrier gas pressures. Finally, the summary and outlook is given in Ch. 6.

2 Theoretical background

2.1 Atomic level structure

Laser spectroscopy can be used to investigate fundamental properties of chemical elements. It helps to gain knowledge on the electron shell structure as well as on the atomic nucleus. In this chapter, the theoretical background of atomic level structure will be briefly explained. Detailed insight is provided, e.g., in Refs. [27], [28] and [29].

2.1.1 Schrödinger equation ansatz

The most simple example of an atom is the hydrogen atom, consisting of one proton and one electron. The atomic structure of hydrogen and hydrogen-like systems can be described precisely by theory if quantum mechanical effects are taken into account.

For hydrogen, the Schrödinger equation is given by [27]

$$\mathcal{H}\Psi(x, y, z) = -\frac{\hbar^2}{2m_p}\Delta_p\Psi(x, y, z) - \frac{\hbar^2}{2m_e}\Delta_e\Psi(x, y, z) - \frac{e^2}{4\pi\epsilon_0 r}\Psi(x, y, z) = E\Psi \quad , \quad (2.1)$$

Δ_e, Δ_p representing the Laplace operators acting on the electron and the proton, m_p, m_e the electron and proton masses, respectively. Transforming the motion to the center of mass system with a reduced mass of $\mu = \frac{m_e \cdot m_p}{m_e + m_p}$ and using the radial symmetry of the Coulomb potential leads to

$$-\frac{\hbar^2}{2\mu}\Delta\psi - \frac{e^2}{4\pi\epsilon_0 r}\psi = E\psi \quad . \quad (2.2)$$

E is the energy, ψ is the wave function describing the system, r is the position relative to the center of mass at r_0 and $\hbar = \frac{h}{2\pi}$ is the reduced Planck constant. Using spherical coordinates and separating the wave function in a radial and angular spherical harmonics contributions

$$\psi(r, \vartheta, \varphi) = R_{n,l}(r) \cdot Y_l^m(\vartheta, \varphi) \quad . \quad (2.3)$$

provides a solution to equation 2.2. n, l and m are, respectively,

- the principal quantum number $n = 1, 2, 3, \dots$,

which corresponds to the electron shell K, L, M, N, \dots ,

2 Theoretical background

- the angular momentum quantum number $l \leq n$,

which can be noted in spectroscopic notation as sub shell s, p, d, f, \dots and

- the magnetic quantum number $-l \leq m \leq +l$.

The corresponding energy levels $E_{n,l,m}$ only depend on the principal quantum number n , such that for hydrogen [27]

$$E_{n,l,m} = E_n = \frac{\mu e^4}{8\varepsilon_0 h^2 n^2} = \frac{R^*}{n^2} \quad , \quad (2.4)$$

whereby R^* is the Rydberg Energy. This results in a degeneration of the levels, such that due to two possible spin projections of the electron $m_s = \pm 1/2$, there are $\sum_{l=0}^{n-1} 2(2l+1) = 2n^2$ possible energy eigenstates for a given n . For hydrogen like atoms with $Z > 1$ the equation changes to $E_n = \frac{Z^2 R^*}{n^2}$.

2.1.2 Fine structure

The degeneracy of the energy eigenstates is removed by interactions within the atomic system due to the finite mass, non-spherical shape, and magnetic moment of the nucleus as well as relativistic and quantum electrodynamic effects [28].

The latter effects result in the Fine Structure (FS) shift and splitting of the degenerated levels. The main contributions to the FS come from

- **Relativistic corrections** of the mass of the electron due to high velocity close to the nucleus,
- **Spin-orbit coupling**, which leads to Zeeman splitting due to interactions of the magnetic moment of the electron with the magnetic field created by it's motion in the field of the nucleus [29] [27], and
- the **Darwin Term**, which takes into account the quantum oscillations resulting in a position deviation of the electron in the coulomb field of the nucleus.

The angular momenta from the spin s and orbit are combined to a total angular momentum $j = l + s$. An energy shift of the levels

$$\Delta E_{SO} = \frac{a}{\hbar^2}(l \cdot s) = \frac{a}{2}[j(j+1) - l(l+1) - s(s+1)] \quad , \quad (2.5)$$

results with the spin-orbit coupling constant $a = \frac{\mu_0 e^2 \hbar^2}{8\pi m_e^2 r^3}$. In total, the three effects sum up and lead for hydrogen to [28]

$$E_{n,l,m} = E_{n,j} = E_n \left[1 + \frac{\alpha^2}{n} + \left(\frac{1}{j+1/2} + \frac{3}{4n} \right) \right] \quad , \quad (2.6)$$

such that the energy of an electron level depends only on n and j . $\alpha = \frac{e^2}{4\pi\epsilon_0 \hbar c}$ is the fine structure constant.

2 Theoretical background

2.1.3 Lamb shift

Another energy shift results from Quantum ElectroDynamic effects (QED). Since the atom is able to absorb and emit radiation, virtual interactions with quantum vacuum fluctuations and vacuum polarization have to be taken into account, too. This interaction leads to a slight deviation of the electron in the coulomb field of the nucleus. The effect is most pronounced for s electrons, because they are closest to the nucleus. It was first observed by the fine structure study of hydrogen in 1947 [30]. The degeneracy of n and j expected for the QED-effect neglecting Dirac-equation is consequently removed, such that, e.g., $s_{1/2}$ has a lower binding energy in comparison to $p_{1/2}$ [27]. The theoretical and experimental study of the lamb shift in myonic hydrogen and deuterium is a state-of-the-art approach to study QED effects [31], [32].

2.1.4 Hyperfine structure

Since the nucleus is not a point-like particle, its motion, size, shape, and magnetic moments have to be considered.

All nuclei with spin $I \neq 0$ have a nuclear magnetic moment of

$$\mu_I = \frac{g_I \mu_K}{\hbar} I \quad (2.7)$$

with the Landé g -factor of the nucleus g_I and the nuclear magneton μ_K . The interaction of the magnetic field B_e created by the rotating electron cloud with the nuclear magnetic moment μ_I results in

$$E_{HFS} = \mu_I B_e \quad . \quad (2.8)$$

If the resolution is increased sufficiently, hyperfine splitting of the fine structure components can be observed. This effect is due to the angular momentum contribution of the nucleons in the atomic nucleus. Due to the fermionic nature of the nucleons, protons and neutrons, the total angular momentum I is zero for nuclei with an even number of protons and neutrons (even-even), half-integer for even-odd and odd-even nuclei and integer for odd-odd nuclei. The HyperFine Structure (HFS) can be explained by the coupling of I to the electron angular momentum J , resulting in the atomic total angular momentum $F = I + J$, such that even-even nuclei consequently do not exhibit the splitting. For the other cases, the degeneracy of F is lifted by the hyperfine splitting, which can be subdivided in a dipole and quadrupole term $\Delta E_{HFS} = \Delta E_{dipole} + \Delta E_{quadrupole}$ and results in a shift of [8]:

$$\Delta E_{HFS} = A \frac{C}{2} + \frac{B}{4} \frac{\frac{3}{2}C(C+1) - 2I(I+1)J(J+1)}{I(2I-1)J(2J-1)} \quad . \quad (2.9)$$

$A_{HFS} = \frac{\mu B_e(0)}{IJ}$ and $B_{HFS} = eQ_S \left\langle \frac{\partial^2 V}{\partial z^2} \right\rangle$ are the hyperfine parameters with the nuclear magnetic dipole moment μ , the magnetic field generated on the nucleus

2 Theoretical background

due to the motion of the valence electron $B_e(0)$, the spectroscopic quadrupole moment Q_S , and the electric field gradient at the nucleus $\frac{\partial^2 V}{\partial z^2}$. The constant C is given by $C = F(F + 1) - I(I + 1) - J(J + 1)$ [8]. The values of $B_e(0)$ and $\frac{\partial^2 V}{\partial z^2}$ can be calculated with moderate precision or deduced from measured reference values of μ and Q_S .

2.1.5 Isotope shift

In the center-of-mass-frame, corrections to the nuclear motion lead to a mass alteration [28]. In combination with a mass change for several isotopes of the same atom this results in a *mass shift*. Moreover, different isotopes exhibit different core radii, such that the isotope shift provides a measure of the change in the core size or rather in its mean-square charge radius. Deviation from spherical shape of the nucleus results in electromagnetic multipole moments of the nucleus and leads to a so-called *field shift* [33].

Both shifts combine to the isotope shift, a frequency shift of the same atomic transition for different isotopes A and A' , of the same element, which can be expressed by

$$\delta\bar{\nu}^{A,A'} = \bar{\nu}^{A'} - \bar{\nu}^A = \delta\bar{\nu}_{\text{mass shift}}^{A,A'} + \delta\bar{\nu}_{\text{field shift}}^{A,A'} . \quad (2.10)$$

The mass shift takes into account that the equation of motion changes slightly due to the different isotope mass ($m^A \neq m^{A'}$). Considering the reduced mass of the systems, the mass shift can be expressed in a Normal Mass Shift (NMS) and a Specific Mass Shift (SMS) term.

$$\delta\bar{\nu}_{\text{mass shift}}^{A,A'} = K_{\text{MS}} \frac{m^{A'} - m^A}{m^{A'} \cdot m^A} = (K_{\text{NMS}} + K_{\text{SMS}}) \frac{m^{A'} - m^A}{m^{A'} \cdot m^A} . \quad (2.11)$$

K_{MS} , K_{NMS} and K_{SMS} are the constants for the total mass shift, the NMS and the SMS, respectively. The NMS comprises the solution of the Schrödinger equation in the center of mass system for one electron, while the SMS takes the mass polarisation in case of many electrons into account.

For increasing Z , the influence of the mass shift decreases, while the field shift increases quadratically [18]. Therefore, the mass shift can be neglected for heavy elements such as actinides without losing accuracy.

The field shift considers the overlap of the inner electronic shells with the core, which leads to a change in the nuclear charge distribution. In a general case, the field shift is given by [34]

$$\delta\bar{\nu}_{\text{field shift}}^{A,A'} = F_{\text{FS}} \lambda^{A,A'} = F_{\text{FS}} \sum_{i=1}^{\infty} \frac{C_i}{C_1} \delta\langle r^{2i} \rangle^{A,A'} , \quad (2.12)$$

2 Theoretical background

but as contributions of higher moments of the charge distribution are small, they can be safely neglected. In the first order, the isotope shift is given by

$$\delta\bar{\nu}_{\text{field shift}}^{A,A'} = \frac{Ze^2}{6h\varepsilon_0} \Delta|\psi_e(0)|^2 \delta\langle r^2 \rangle^{A'A} = F_{FS} \delta\langle r^2 \rangle^{A'A} \quad , \quad (2.13)$$

where $\delta\bar{\nu}$ represents the change in the transition frequency due to a variation of electron density at the nucleus between the two atomic levels $\Delta|\psi_e(0)|^2$. $\delta\langle r^2 \rangle^{A'A} = \langle r^2 \rangle^A - \langle r^2 \rangle^{A'}$ is the change in the root-mean-square charge radii. Overall, the isotope shift can therefore be expressed by:

$$\delta\bar{\nu}^{A,A'} = K_{MS} \frac{m^{A'} - m^A}{m^{A'} \cdot m^A} + F_{FS} \delta\langle r^2 \rangle^{A,A'} \quad (2.14)$$

with K_{MS} and F_{FS} as atomic mass and field shift factors [35]. Typical values of isotope shifts for light actinides are in the range of several GHz [36].

Precise laser spectroscopy enables systematic studies of differences in the root-mean-square charge radii over a wide range of isotopes. The absolute charge radii can be obtained by elastic electron scattering or X-ray spectroscopy of muonic atoms. Moreover, these scattering experiments can be applied to extract the mass and field shift factors [37]. If K_{MS} and F_{FS} are known for a different transition of the same element (e.g., for stable isotopes), they can be extrapolated to the new transition by a King-Plot analysis [38].

2.1.6 Magnetic dipole and electric quadrupole moment

The atomic nucleus exhibits a magnetic dipole moment evoked by the intrinsic angular momentum of all nucleons and the orbiting motion of the protons. The magnetic dipole moment is therefore given by

$$\mu_I = \sum_i^A \left(g_i^s s_i + g_i^l l_i \right) \quad , \quad (2.15)$$

with the orbital and spin gyromagnetic ratios g^l and g^s . l_i and s_i are the individual orbital angular momentum and the spin, respectively, that couple to the total angular momentum $L = \sum_i l_i$ and the total spin $S = \sum_i s_i$. The magnetic dipole moment allows drawing conclusions about the orbital occupation of the valence nucleons, since in the nuclear shell model the remaining unpaired nucleon is located in an orbit with $j = l \pm s$. The single-particle magnetic moment is defined as follows [39]:

$$\mu = \begin{cases} (j - \frac{1}{2})g_l + \frac{1}{2}g_s = \begin{cases} j - \frac{1}{2} + \mu_p & \text{for odd p} \\ \mu_n & \text{for odd n} \end{cases} & \text{for } j = l + \frac{1}{2} \\ \frac{j}{j+1} \left[(j + \frac{3}{2})g_l + \frac{1}{2}g_s \right] = \begin{cases} \frac{j}{j+1} \left[j + \frac{3}{2} - \mu_p \right] & \text{for odd p} \\ -\frac{j}{j+1} \mu_n & \text{for odd n} \end{cases} & \text{for } j = l - \frac{1}{2} \end{cases} \quad (2.16)$$

2 Theoretical background

If the magnetic moments of nuclei with $I \neq 0$ are measured precisely, information about the nuclear wavefunction can be derived.

In case of deviation from spherical shape, nuclei exhibit an electric quadrupole moment $Q = \int (3z^2 - r^2)\rho(r)d^3r$. A distinction is made between the spectroscopic and the intrinsic quadrupole moment Q_S and Q_0 , respectively, which are linked to each other according to Ref. [40]

$$Q_S = \frac{3K^2 - I(I+1)}{(I+1)(2I+3)} \cdot Q_0 \quad . \quad (2.17)$$

While Q_0 is related to the quadrupole deformation parameter β_2 , only Q_S can be measured in experiments. Depending on the value of Q_0 , the nucleus is either prolate ($Q_0 > 0$), i.e., elongated along the symmetry axis, oblate ($Q_0 < 0$), i.e., compressed along the symmetry axis, or spherical ($Q_0 = 0$). Most nuclei have a prolate shape [41], [42]. In HFS experiments, magnetic dipole and electric quadrupole moments can be measured precisely following Equation 2.9.

2.1.7 Relativistic effects on the electronic structure

With increasing proton number Z , the influence of relativistic effects on the electronic shells gains importance [43]. In a simplified picture, the high velocities of inner-shell electrons orbiting the heavy atomic nucleus lead to a contraction of the s - and $p_{1/2}$ -orbitals. As a result, the nuclear potential is effectively screened and outer lying electron shells such as $p_{3/2}$, $d_{3/2}$ and $d_{5/2}$ expand [44]. Physical and chemical properties as the binding energy of electrons, the valence electron configuration, interatomic forces, bond lengths, enthalpies and the overall chemical behaviour altogether can be affected by this effective shielding [45].

Relativistic Dirac-Fock calculations predict this behaviour [25], which leads to a shift in electronic levels. Without relativistic correction, the electrons gradually fill the electronic shells $1s$, $2s$, $2p$, $3s$, $3p$, $4s$, $3d$, $4p$, $5s$, $4d$, $5p$, $6s$, $4f$, ..., whereby the shells can be occupied by $2n^2$ electrons. As mentioned in Sec. 2.1.1, the electrons within a shell can be distinguished by their quantum numbers n, l, m . If relativistic effects are taken into account, the level ordering can shift due to the contraction of s and $p_{1/2}$ shells and expansion of the outer shells. An example of this behaviour is shown in Fig. 2.1.

The electron orbitals in the relativistic cases split due to $l - s$ coupling to sub shells, whereby the $s_{1/2}$ and $p_{1/2}$ levels are energetically stabilized. Consequently, the $d_{3/2}$, $d_{5/2}$, $f_{5/2}$ and $f_{7/2}$ shells are destabilized. In the case of ${}_{96}\text{Cm}$, the homologue of ${}_{64}\text{Gd}$, the contraction of the $7s_{1/2}$ level in the relativistic calculation leads to a lower orbital binding energy than for the $6d_{3/2}$ and $6d_{5/2}$ level.

One prominent example of the change in ground state due to relativistic effects is the element lawrencium ($Z=103$), which has a $7p \ ^2P$ configuration instead of a $6d \ ^2D$ configuration [46], [47].

2 Theoretical background

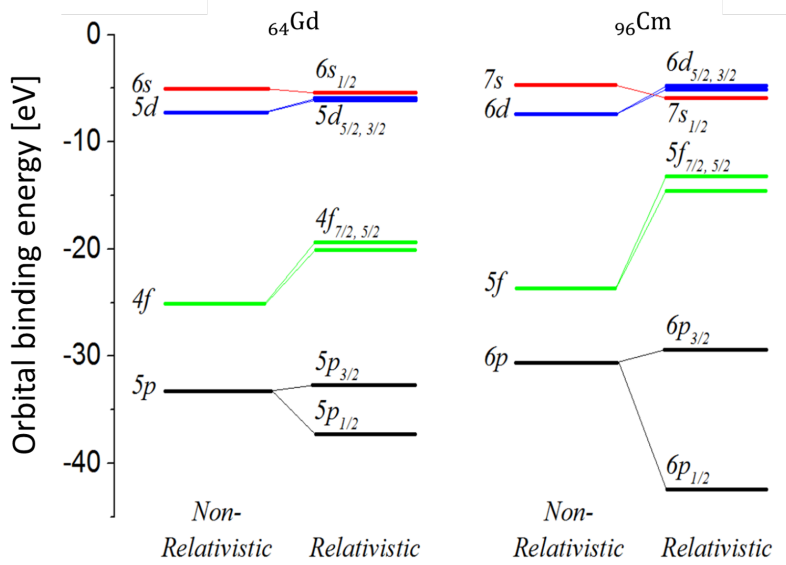


Figure 2.1: Orbital binding energy in non-relativistic calculation and relativistic calculation for ^{64}Gd and its actinide homologue ^{96}Cm , adapted from Ref. [25]. For ^{96}Cm , the $7s_{1/2}$ level is in the relativistic calculation energetically swapped with the $6d_{3/2}$ and $6d_{5/2}$ levels.

2.2 Nuclear models

The theoretical description of the nucleus is a well-investigated topic. Analogous to the electronic shell ansatz, the protons and neutrons in the nucleus form shell structures, which enhance the binding energy. Therefore, the stability of a nucleus can be theoretically described by a liquid drop term and a shell correction term. The first description of shell closures was given through a spherical shell model including a spin-orbit term by Göppert-Meyer [48] and Haxel, Jensen and Suess [49] in 1949. An extension to deformed shapes is given by the Nilsson model. More realistic energy levels, which will not be discussed in detail in this thesis, are obtained by using macroscopic-microscopic models, which consider vibrational and rotational excitations. For more details, see, e.g., Refs. [50] [51], [52], and [53].

2.2.1 The Liquid Drop Model

Originally derived for description of nuclide masses, the first model to describe nuclear properties was the Liquid Drop Model (LDM). As scattering experiments indicated an uniform density and charge distribution of nuclei and a scaling of nuclear sizes with $r \propto A^{1/3}$, the nucleus can be approximated by an incompressible liquid drop, held together by cohesive forces and by surface tension [54]. By introducing the coefficient r_0 , which represents the average length of an interparticle distance, the relation can be expressed by the equation $r = r_0 \cdot A^{1/3}$. r_0 is here in the range of approximately 1.2 fm.

2 Theoretical background

A semi-empirical model to describe the binding energies of liquid-drop-like nuclei is given by the Bethe-Weizsäcker mass formula [55]. The binding energy of a nucleus is given by [54]:

$$\begin{aligned} E_B(Z, A) &= (Z(m_p + m_e) + Nm_n)c^2 - M(Z, A)c^2 \\ E_B(Z, A) &= E_V + E_S + E_C + E_{symm} \pm \delta \end{aligned} \quad (2.18)$$

with the experimentally obtained atomic mass of the nucleus, $M(Z, A)$, the volume term E_V , the surface term E_S , the Coulomb term E_C , the asymmetry term E_a , and the pairing term δ . The parametrization for the different terms differs slightly between different authors. Here, the parametrization of [56] is used. The volume term $E_V = b_V \cdot A$ represents the binding energy due to the strong force between the nuclides, which is proportional to $r^3 = A$. The constant b_V gives the volume energy per particle, which is about 15 MeV. Since nuclides at the surface, which is proportional to $r^2 = A^{2/3}$, are less bound, the surface term $E_S = -b_S \cdot A^{2/3}$ is negative. The value of the surface constant b_S is about 16 MeV. The Coulomb term $E_C = -b_C \frac{Z^2}{A^{1/3}} = -\frac{3}{5} \frac{(Ze)^2}{r_0 A^{1/3}}$ takes the repulsion between the protons into account. Compared to b_V and b_S , b_C is relatively weak with about 0.7 MeV, but due to $E_C \propto Z^2$, the Coulomb term gets very influential for heavy nuclei. The symmetry term $E_{symm} = -b_{symm} \frac{(N-Z)^2}{2A}$ with $b_{symm} \approx 45$ MeV is responsible for preferring equal numbers of protons and neutrons, which is visible in the nuclide chart up to ^{40}Ca . For increasing Z , the symmetry gets lost in favour of neutron rich nuclei.

The last term, $\delta = b_P [(-1)^N + (-1)^Z] \frac{1}{\sqrt{A}}$ with $b_P \approx 6$ MeV, takes the pairing correlations between identical nucleons into account, which lead to an enhanced stability of even-even nuclei.

The Bethe-Weizsäcker mass formula models the experimentally measured values for the binding energy per nucleon well for stable nuclei. However, certain “magic” nucleon numbers show a strong discrepancy compared to the theoretical expectation. The binding energies are minimized, resulting in a stabilization of magic nuclei. To explain this behaviour, the spherical shell model was developed.

2.2.2 The spherical shell model

In the spherical shell model, the nucleons are homogeneously distributed in the nucleus and can be described according to Fermi statistics. The occupation probability of the single particles is given by a Fermi distribution, whereby the surface region around the Fermi energy is smeared due to the pairing force, which couples pairs of neutrons and protons to spin and parity 0^+ . A spin-orbit component of the nucleon-nucleon interaction for spherically symmetric shells leads to the successful explanation of the magic numbers for neutrons at $N = 2, 8, 20, 28, 50, 82, 128$ and for protons at $Z = 2, 8, 20, 28, 50, 82$. The magic numbers correspond to shell closures analogue to the electronic shell structure [57], [2]. At the magic numbers, the energy spectrum of the nucleons between the filled and the next empty shell feature large gaps.

2 Theoretical background

Experimental evidences for the nuclear shell structure are, e.g., the occurrence of many stable isotopes and isotones at magic proton and neutron numbers, respectively, separation energies of protons and neutrons, energies of first excited states, and neutron capture cross section around the shell closure.

The potential, which combines all nucleon-nucleon interactions, is called the mean-field potential. In most cases, the mean-field potential is expressed by a square-well, harmonic-oscillator or a Woods-Saxon potential [58]. A very good guide to the nuclear shell model is given by [1]. The spherical shell model is very powerful in describing lower and middle mass nuclei, but for heavy and superheavy nuclei there are deviations from this model due to deviation of nuclear shapes from spheres. To model these deformed heavy nuclei, the Nilsson model provides an extension of the spherical droplet model.

2.2.3 The Nilsson model

Only one third of nuclei around magic numbers are spherical [42]. Experimental evidences for deviation from spherical shape is found in, e.g., quadrupole moments, which prove that most of the nuclei are prolate [13]. Remaining proton-neutron interaction leads to a mixing of states and deformation. Furthermore, deformed nuclei can form gaps in the single particle spectrum and built deformed shells. Therefore, an extension of the spherical shell model for the description of deformed nuclei was developed by Nilsson [59]. The deformed nuclei are cylindrically symmetric, such that the angular momentum quantum numbers j , l and s have to be replaced by their projection on the symmetry axis K , Ω , Λ and Σ . Analogue to $j = l + s$, $\Omega = \Lambda + \Sigma$ is valid, which is visualized in Fig. 2.2.

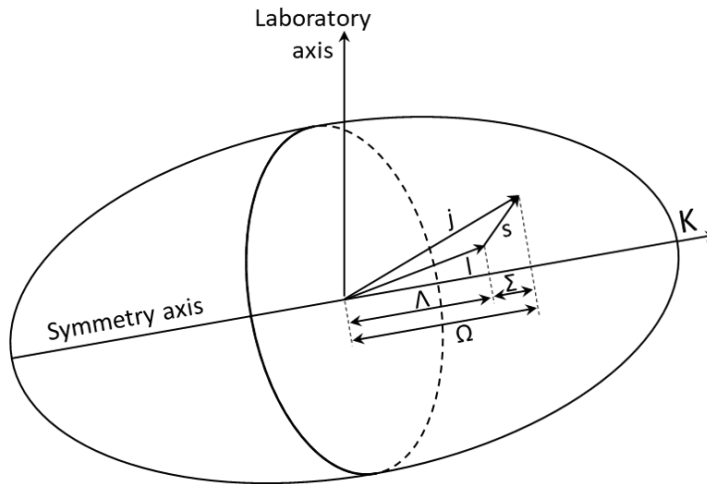


Figure 2.2: Quantum numbers j , l and s and their projection on the symmetry axis K , Ω , Λ and Σ . Picture adapted from Ref. [60].

2 Theoretical background

The oscillator frequencies ω_x , ω_y and ω_z are replaced by ω_\perp and ω_z [61]:

$$\begin{aligned}\omega_x = \omega_y = \omega_\perp &= \omega_0(\epsilon)\left(1 + \frac{1}{3}\epsilon\right) \\ \omega_z &= \omega_0(\epsilon)\left(1 - \frac{2}{3}\epsilon\right)\end{aligned}\tag{2.19}$$

with the elongation parameter ϵ and the oscillator frequency for the spherical harmonic oscillator ω_0 . The principal quantum number n can also be split in two parts $n = n_z + n_\perp$, which are parallel or perpendicular to the symmetry axis, respectively. Therefore, a nuclear orbital in the Nilsson model is fully described by the asymptotic quantum numbers $\Omega^\pi[nn_z\Sigma]$, whereby the parity π is preserved. When the calculated single particle energy $E_{s.p.}$ is plotted versus the deformation, it results in a Nilsson diagram, which shows also shell gaps for deformed nuclei. For neutrons, deformed shells are predicted at $N = 134, 142, 152$ and 162 [60] for an expected deformation around $0.2 - 0.3$ for fermium [62]. Deformed proton shells are predicted and experimentally proven at $Z = 100$ [60], [63]. Figure 2.3 shows the Nilsson diagram for neutrons $N \geq 142$. The abscissa shows hereby the quadrupole deformation parameter ϵ_2 . The spherical shell gaps ($\epsilon_2 = 0$) are shown in blue, the deformed shell gaps in green. The original figure, as well as the Nilsson diagram for protons, can be found in Ref. [60]. Further information on the Nilsson model can be found in Refs. [59], [64] and [65]. The Nilsson model is a phenomenological microscopic model. Other microscopic models use an effective nuclear interaction with a Hartree-Fock ansatz to calculate the mean-field, while relativistic mean-field theory take nucleon-nucleon interactions with meson and photon exchange into account. To obtain more realistic energy levels, vibrational and rotational excitations have to be considered in the models. These so called macroscopic-microscopic models are explained in detail in Refs. [51], [52] and [53].

To improve the theoretical models, increase their predictive power and to understand the underlying physics of the shell structure, experimental data have to be obtained, e.g., on decay characteristics, energies of excited states, nuclear moments, the strength of shell effects, and the location of the shell gaps [66].

2.2.4 Shape staggering

Nuclei can exhibit shape coexistence, which was discovered by isotope shift measurements [14], [67]. Even combinations of spherical, prolate, and oblate shapes are possible in the same nucleus, as observed in lead [68]. A theoretical treatment of shape coexistence in odd-mass nuclei near closed shells and in doubly even nuclei can be found in Refs. [69] and [70], respectively.

As isotope shift measurements give access to changes in the mean-square charge radius $\delta\langle r^2 \rangle$ (see subsection 2.1.5), it gives a clue on the changes in nuclear size.

2 Theoretical background

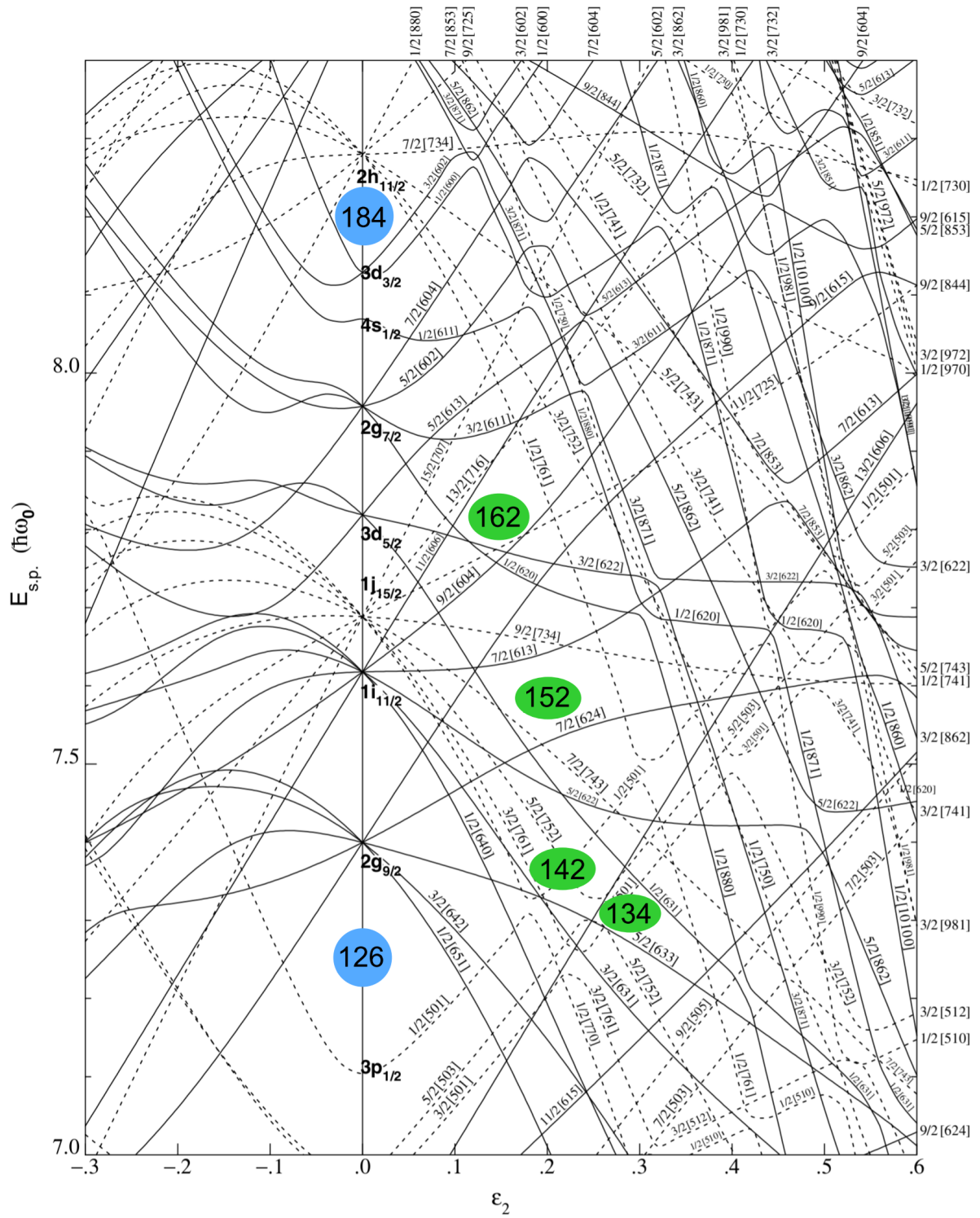


Figure 2.3: Nilsson diagram for $N \geq 126$. The single particle energy is plotted versus the quadrupole deformation parameter ϵ_2 . The picture is adapted from Ref. [60].

2 Theoretical background

These changes can be due to a deformation modification resulting from adding or removing nucleons.

A very prominent example is the so-called Odd-Even Staggering (OES) occurring, where the odd nuclei have a smaller mean-square charge radius than the average of their two even neighbours. This behaviour is attributed to a coupling between the proton density and the neutron pair density. These pairing correlations lead to an increase in binding energy [71]. The reduction of pairing by the blocking effect [72] in a nucleus with odd neutron number leads to a reduced neutron pairing density. Due to the coupling, the proton density is reduced for odd- N nuclei and thus, the charge radius.

In some regions of the nuclear chart, an inversion of the normal odd-even staggering is found. A normal OES can thereby be assigned to even-multipole deformations and inverse OES to odd-multipole deformations [73]

Recently, the shape staggering of mercury isotopes was observed and theoretically explained [13]. The size of the spherical even mass $_{80}\text{Hg}$ isotopes decreases with decreasing N , while the odd mass isotopes have noticeably larger charge radii.

Monte-Carlo-Shell-Model (MCSM) calculations successfully describe this behaviour for a quantum phase transition between deformed states and nearly spherical states, which occurs due to an interplay of monopole and quadrupole nucleon-nucleon interactions. The observed shape staggering is therefore caused by the competition of the deformed and the spherical states.

Odd-even staggering is meanwhile a well-known phenomenon, that has been observed for many isotopes of different atoms [74].

2.3 Nuclear shell effects

Nuclear existence is challenged by the interplay between Coulomb repulsion and the strong nuclear force. For the actinide element fermium ($Z=100$), the Coulomb force between the protons and the effective strong force are in the same order of magnitude, eventually resulting in nuclear fission. Quantum mechanical shell effects of the nucleons help to stabilize heavy and superheavy nuclei against fission (see Sec. 2.2).

Many theoretical models try to describe this behaviour and predict the location of stabilized shells, which may lead to the formation of a region of shell stabilized nuclei, the so called “island of stability” [75]. This island of stability is predicted for superheavy nuclei around $Z=120$ and $N=172$ or 184 , whereas calculations in the hyperheavy region predict enhanced stability around $N \approx 258$ and $N \approx 308$ for proton numbers around $Z=120$ and $Z \approx 160$, respectively [71].

Especially at magic numbers, the single-particle energy spectra of the nucleons exhibit gaps between the filled and the next empty shell. However, the localization of magic shell gaps in heavy nuclei is predicted to be washed out compared to the nuclear shell structure of lighter nuclei [71]. Investigating experimental evidences for shell closures of known actinide nuclei helps to improve the theoretical models

2 Theoretical background

to pin down the location of the island of stability more precisely.

The main focus of this thesis is on the resonance ionization spectroscopy study of the fermium isotopes $^{248,249,250}\text{Fm}$ and $^{255,257}\text{Fm}$, such that the deformed $Z=100$ shell gap [76] and the $N=152$ deformed neutron shell gap can be probed by laser spectroscopy.

In the following sections, the experimental and theoretical evidences for shell gaps are introduced, followed by predictions and experimental evidences of the shell structure in the region around fermium.

2.3.1 Experimental investigation of nuclear shell effects

To study nuclear shell effects, experimental measurements of **(a)** atomic masses have been historically established. Other possibilities to measure the influence of shell effects are **(b)** the systematic study of the energies of excited nuclear states and **(c)** the analysis of a general trend of experimental nuclear charge radii.

(a) Mass spectrometry According to the equivalence of mass and energy [77], measuring the mass of a nucleus gives a direct measure of the nuclear binding energies, such that precision mass spectrometry is sensitive to shell gaps. The effects of the shell can be directly mapped by experimentally measured masses, which agree to expected values from the liquid drop model. Well established is hereby the analysis of nucleon separation energies, especially of two-neutron and two-proton separation energies $S_{2n}(N, Z) = E_B(N, Z) - E_B(N - 2, Z)$ and $S_{2p}(N, Z) = E_B(N, Z) - E_B(N, Z - 2)$.

(b) Excited nuclear states The study of energies of excited nuclear states is mostly obtained by nuclear spectroscopy. In particular, $\alpha - \gamma$ coincidence spectroscopy has proven its power to combine the study of decay properties, the identification of excited states and the investigation of isomeric states [66]. From the study of excited levels it is known that excitation energies, spins and parities follow systematic trends along the isotone lines ($N=\text{const}$) in even- Z odd-mass nuclei and along the isotope lines ($Z=\text{const}$) in odd- Z odd-mass nuclei [66]. A high excitation energy of the first electric quadrupole 2^+ state, E_{2^+} and a small transition probability to the first 2^+ excited state, $B(E2)$ indicate a spherical shell closure as well as a minimum in the quadrupole moment Q_S [78]. Alternatively to $B(E2)$, the ratio of the energies of the first 4^+ and 2^+ states, $R_{4/2}$ state can be used [79].

(c) Charge radii Observing and comparing the change of nuclear charge radii $\delta\langle r^2 \rangle$ derived from isotope shifts can display shell-effect signatures [8]. A characteristic change in the slope of changes in the root-mean-square charge radii $\delta\langle r^2 \rangle$ (“kink”) emerging for neighboring isotones can reveal nuclear shell closures. For magic proton and neutron numbers at $Z= 8, 20, 28, 50, 82$ and $N=2, 8, 20, 28, 50, 82, 128$, a kink in the isotonic, or respectively, isotopic radii trend is well established [80]. A very good overview on the

2 Theoretical background

N and Z dependence of nuclear charge radii obtained from optical and K_α x-ray isotope shifts and absolute radii measured from muonic and electronic scattering experiments is given in Ref. [80].

Since the gaps in the single-particle energy spectrum of nucleons between the filled and the next empty shell are particularly pronounced for magic numbers, the aforementioned studies in the vicinity of doubly magic nuclei could be used to elucidate trends occurring for deformed shell gaps. Prominent examples for the influence of shell effects on experimental parameters are given by measurements on the doubly magic nuclei ^{132}Sn and ^{208}Pb , as presented below.

For ^{132}Sn ($Z=50$, $N=82$), the occurrence of a shell closure is observed by high precision mass spectrometry, the study of E_{2^+} energies and laser spectroscopy across $N=82$. For the mass spectrometry measurement, the mass excess of the tin isotopes $^{127,131-134}\text{Sn}$ was obtained to calculate the two-neutron separation energies and the neutron shell gap parameter $\delta_{2n}(Z, N) = [S_{2n}(Z, N + 2) - S_{2n}(Z, N)]$, which peaks at $N=82$ [81]. Moreover, the comparison to other isotones with $N=82$ revealed that the shell gap is maximal for $Z = 50$. The measured gap size agrees hereby well with the gap size obtained from nuclear theory calculations [82].

The study of the excitation energy of the first electric quadrupole 2^+ state was realized by measuring the single-particle states in ^{133}Sn , which are just outside the double-shell closure of ^{132}Sn [83]. Inverse kinematics were used for a particle-transfer reaction to produce ^{133}Sn , from which the single neutron excitations for ^{132}Sn were extracted, which reveal the shell closure as a large discontinuity of E_{2^+} .

High-precision laser spectroscopic measurements of the isotope shift of the even mass tin isotopic chain $^{108-134}\text{Sn}$ substantiated the effect of the shell closure on the trend of mean-square nuclear charge radii [84]. To extract the mean-square nuclear charge radii, the atomic mass and field shift constants K_{MS} and F_{FS} (see Sec. 2.1.5) were obtained from a King-Plot analysis. A clear kink at $N=82$ was observed, and modeled by the recently developed Fayans energy density functional, indicating that pairing and surface energy-density effects cause the change in charge radii after the shell closure.

A very good overview of the structural evolution around the magic numbers 8, 20, 28, 50, 82, and 126 is given in Ref. [85]. A nice survey of the interplay between nuclear charge radii and other nuclear observables for light nuclei is given by [79].

The doubly magic nuclei feature a spherical shape [86]. Shell effects may be less pronounced for not-magic shell gaps and deformed nuclei. Especially for heavy and superheavy elements, observables of nuclear stabilization may arise at smaller shell gaps in these deformed nuclei [71]. In the actinide region, nuclei are deformed in their ground state [42]. Nuclei in the region around $^{254}_{102}\text{No}_{152}$ are

2 Theoretical background

known to exhibit a prolate deformation of about $\beta_2 \geq 0.24$ [3]. One prominent example is the deformed $N=152$ shell gap (see Sec. 2.3.3).

A measure of the deformation is the quadrupole moment Q_S , which can be obtained by the study of excited nuclear states. In the region of shell closures, the deformation is reduced [42]. Moreover, the appearance of isomers portend deformation. Possibilities for isomer formation are hereby spin trap isomers, which result from a high difference in spin or parity, shape isomers, which originate from different shapes of decaying nuclei and K -isomers, excited states with high spin which form due to the conservation of angular momentum [87]. K -isomers indicate deformation whilst maintaining axial symmetry.

2.3.2 Predictions for shell gaps in the vicinity of $N = 152$

For the shell structure study of heavy and superheavy nuclei by laser spectroscopy, atomic and nuclear structure theory has to treat open shell systems and cope with dense atomic spectra. The Dirac equation is defined with different terms to, e.g., take the interaction between the electrons into account and to consider the strong Coulomb fields [88]. The nuclear density is hereby obtained from nuclear Density Functional Theory (DFT). Within this framework, self-consistent nuclear mean-field models have proven their predictive power [82]. Depending on the used density functionals, various mean-field calculations are known, e.g., Energy Density Functional (EDF) theory, Hartree-Fock-Bogolyubov (HFB) calculations or the Skyrme-Hartree-Fock (SHF) approach.

Within the different models, the parametrizations can be varied to apply a best fit to experimental data for different characteristics of the studied nuclei. In Ref. [82], a very good overview on the change in predicted proton and neutron magic number for a spherical shell closure depending on the used parametrization of different nuclear calculations is given, which is briefly summarized here.

To compare the predictive power of nuclear EDF models with different parametrizations and calculation approaches in Ref. [82], all parametrizations were first used to calculate the ground states of ${}_{108}^{264}\text{Hs}_{156}$, before extrapolating them towards heavier nuclei. Hereby, six possible parametrizations from the non-relativistic Skyrme-Hartree-Fock (SHF) approach (SkM*, SkP, SLy6, SkI1, SkI3, SkI4) and four parametrizations for the Relativistic Mean-Field model (RMF) (NL-Z, PL-40, NL-SH, TM1) were chosen from a huge variety of possible EDF functionals. Hereby, RMF and SHF are competitor models, which are competing with the Gogny force model [89]. For calculations with a Gogny force, the same effective interaction is used to extract direct, exchange and pairing matrix elements, while Skyrme parametrizations use different effective interactions to treat the particle-hole and pairing matrix elements, respectively [90].

For the spherical proton shell gap, most parametrizations agree on $Z=120$, while the parametrizations SkI4, SkM* and SkP from SHF deviate from this prediction

2 Theoretical background

by preferring $Z=114$ or $Z=126$. SkI4, which has been optimized based on systematic fits to the data including exotic nuclei, includes surface properties of the nuclei and allows a free variation of the strength of the spin-orbit force, locates the shell gap at $Z=114$. It contains hereby a minimal relativistic correction within the non-relativistic SHF framework. The standard Skyrme forces SkM* and SkP, which are respectively optimized to model incompressibility and fission properties or to treat pairing self-consistently, favour the shell closure at $Z=126$. For the spherical neutron shell gap, the non-relativistic models tend to predict a magic number at $N=184$, while the relativistic models prefer $N=172$ with a less pronounced gap. The relativistic parametrizations NL-Z and PL-40, which are designed for a best fit to nuclear ground-state properties, but with a focus on small densities at the outer nuclear surface for the latter, predict both $N=172$ and 184 as magical neutron numbers. The force NL-SH, which is adjusted to exotic nuclei, exhibits a shell closure at $N=184$ for nuclei with $Z < 110$. The parametrizations used in SkI4, SKI3 (similar to SKI4 but with a fixed isovector spin-orbit force), NL-Z and PL-40, which give the best result for comparison with ${}^{264}_{108}\text{Hs}_{156}$, predict the most pronounced shell closures. Doubly magic shell closures are located at $(Z=114, N=184)$, $(Z=120, N=172)$ or $(Z=126, N=184)$. In summary, the nuclear calculations of different comparable models exhibit significant deviations depending on the chosen parametrization and thus the assumed interaction [82].

Shell gaps decrease in energy with increasing deformation (see Sec. 2.2.3). In the region around fermium, with a quadrupole deformation of $\beta \approx 0.3$ [44], deformed shell gaps are predicted at $N=134, 142, 152$ and 162 . In the region between $Z=95-111$ and $N=149-162$, especially the deformed shell gaps at $N=152$ and $N=162$ are pronounced according to theoretical calculations [4]. One possibility for a theoretical treatment of the influence of deformation on the single-particle energy levels is given by macroscopic-microscopic calculations [91], which is shortly summarized here. Since the deformation is linked to the appearance of rotational bands, which can be revealed by the study of E_{2+} , the calculations in Ref. [91] were performed to model E_{2+} and different multipole deformation parameters. As in Ref. [82], the calculations were tested on experimentally available data in the region of the heaviest elements. The calculations show minima in E_{2+} at ${}^{254}_{102}\text{No}_{152}$ and ${}^{270}_{108}\text{Hs}_{162}$, which hint towards a weak deformed gap at $Z=102, N=152$ and at $N=162$ and $Z=108$ [91]. Energy gaps of about $\delta_n = 1.5 \text{ MeV}$ at $N=162$ and $\delta_p = 1.3 \text{ MeV}$ at $Z=108$ are obtained for ${}^{270}\text{Hs}$, whereas the gap at $N=152$ is calculated to about 1.2 MeV in ${}^{254}\text{No}$. The gap at $Z=102$ is with about 0.6 MeV smaller than the gap at $Z=100$ with about 0.8 MeV .

The precise measurement of atomic transitions gives access to nuclear properties, which are valuable data to improve theoretical models and to study fundamental symmetries. The interplay of experimental measurements and theoretic calculations of atomic and nuclear properties enables to give a measure on the charge-

2 Theoretical background

density distribution in spherical and deformed nuclei. Precise calculations of charge radii can model the impact of nucleonic corrections on the nuclear charge density, which are needed to augment high precision isotope shift measurements. A mean-field theory approach using quantified nuclear energy density functionals and density-dependent pairing forces, which is also applicable for nuclei deviating from spherical shapes, was recently developed [92]. To benchmark nuclear and atomic theory and refine the models, further experimental studies on deformed sub shell gap at $N=152$ are needed.

2.3.3 Experimental evidence of the $N = 152$ shell gap

Experimental evidence for the deformed shell gap at $N=152$ was provided in 1954 through α -energy studies of ${}_{98}\text{Cf}$ isotopes [93]. To model the influence of the deformed shell gap at the neutron number $N=152$, experimental properties like the mass, the α -decay energy Q_α and half-life, the spontaneous-fission barrier, and the fission lifetime were compared with values expected for a liquid drop model for even-even nuclei between $Z=92-108$ in 1989 by [76].

In the vicinity of the shell gap, a minimum in Q_α was observed. Since shell effects delay the α decay, the half-life is increased in comparison to neighboring isotopes. The increased stability of nuclides featuring a closed proton or neutron shell (or both) lead to an increased fission barrier, which results in an increase of the spontaneous-fission half-life by 15 orders of magnitude in comparison to liquid-drop-model predictions [76]. The systematic study of Q_α between ${}_{89}\text{Ac}$ and ${}_{111}\text{Rg}$ reveals a slight drop in Q_α for $N=152$ in comparison to neighboring isotopes and a more pronounced minimum for $N=162$ in combination with an overall decrease in Q_α with increasing N and overall increase in Q_α with increasing Z [94].

As stated in Sec. 2.3.1, high-precision mass spectrometry gives a direct measure on nuclear binding energies and are suitable to determine shell gaps. The $N=152$ shell gap was probed by high-precision mass measurements of ${}_{102}\text{No}$ and ${}_{103}\text{Lr}$ isotopes at SHIPTRAP [95]. For the isotopes ${}^{252-255}\text{No}$ and ${}^{255,256}\text{Lr}$, the two-neutron separation energies $S_{2n}(N, Z) = E_B(N, Z) - E_B(N - 2, Z)$ and the neutron shell gap parameter $\delta_{2n}(Z, N) = [S_{2n}(Z, N + 2) - S_{2n}(Z, N)]$, were obtained, revealing a local maximum indicating a weak shell gap at $N=152$.

In Fig. 2.4, $\delta_{2n}(Z, N)$ extracted from values of the two-neutron separation energies tabulated in Ref. [5] are given. The deformed shell gap at $N=152$ can be recognized by the maximum in δ_{2n} between Cf ($Z=98$) and No ($Z=102$).

Systematic $\alpha - \gamma$ coincidence decay spectroscopy allows studying the decay properties of isotopes in the vicinity of $N=152$, with simultaneous identification of the excited states and investigation of isomeric states. The excitation energy of the first electric quadrupole state, E_{2+} of even-even nuclei in the region of ${}^{254}\text{No}$ is predicted to be minimal for $N=152$ in nobelium and fermium, indicating

2 Theoretical background

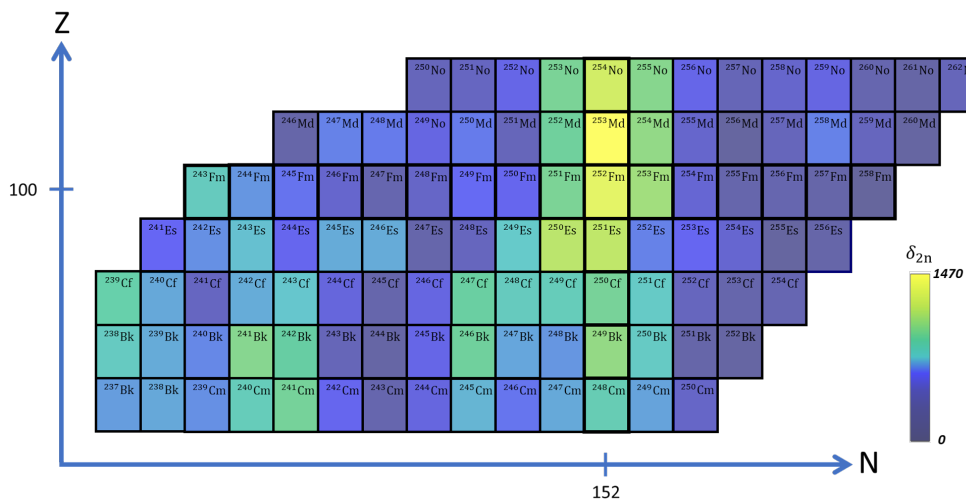


Figure 2.4: δ_{2n} values in the vicinity of the deformed sub shell at $N=152$ reveal the shell gap. The values were obtained from the results of the Atomic Mass Evaluation (AME) database [5].

an increased deformation at the shell gap. Experimental E_{2+} excitation energies were obtained for several isotopes of ${}_{96}\text{Cm}$, ${}_{98}\text{Cf}$, ${}_{100}\text{Fm}$ and ${}_{102}\text{No}$ isotopes around $N=152$ [63], but without data for the isotopes ${}^{252}\text{Fm}$ and ${}^{254,256}\text{No}$ one could not make more comprehensive statements. In 2015, high-resolution α decay spectroscopy on ${}^{256}\text{No}$ enabled the extraction of E_{2+} for ${}^{252}\text{Fm}$ [96], revealing a local minimum and thus a portending a maximal deformation for this nucleus.

Due to the deformation of nuclei in the region around fermium, the appearance of K -isomers is expected. Moreover, spin isomers occur for heavy elements due to the high and low- j orbitals, which coexist close to the Fermi surface [97]. Around $N=152$, in-beam spectroscopy revealed the existence of K -isomers, e.g., in ${}^{250}\text{Fm}$ [98], [63] and ${}^{254}\text{No}$ [98], [99]. Since K is the projection of total angular momentum on the symmetry axis (see Sec. 2.2.3), K -isomers are an indicator of axial symmetry. Further study of K -isomers in ${}^{254}\text{No}$ support the assumption of a prolate axially symmetric shape of that nucleus [100]. An overview of K -isomers of even-even nuclei between ${}_{96}\text{Cm}$ and ${}_{110}\text{Ds}$ is given in Ref. [101]. Moreover, systematic studies of Q_α values and mass spectrometry of long decay chains observed in ${}^{257,259,261,263}\text{Db}$ and ${}^{247m}\text{Md}$ [101] and in ${}^{255,257,258}\text{Rf}$ and ${}^{257,258}\text{Db}$ [66] confirm the $N=152$ shell gap.

Rotational bands upon isomers, found by spectroscopy in fermium, e.g., in ${}^{246}\text{Fm}$ [102], ${}^{248}\text{Fm}$ and ${}^{250}\text{Fm}$ [103], [104], and in nobelium, e.g., in ${}^{252,253}\text{No}$ [105] and ${}^{254}\text{No}$ [100], [106], help to determine spins and parities of the investigated isomers. It was found that the moment of inertia increases with rotational frequency due to disappearing pairing correlations [102]. Moreover, high- K states forming K -

2 Theoretical background

isomers are fed by rotational bands [96]. A list of rotational bands on top of isomeric states between ${}_{82}\text{Pb}$ and ${}_{110}\text{Ds}$ has been published in Ref. [104]. Together, the existence of K -isomers and rotational bands probe the underlying prolate deformation of atomic nuclei in the region around $N=152$, $Z=100$ with $\beta \approx 0.3$ [105], [107]. The predicted ground-state quadrupole deformation from Ref. [3] is given in Fig. 2.5.

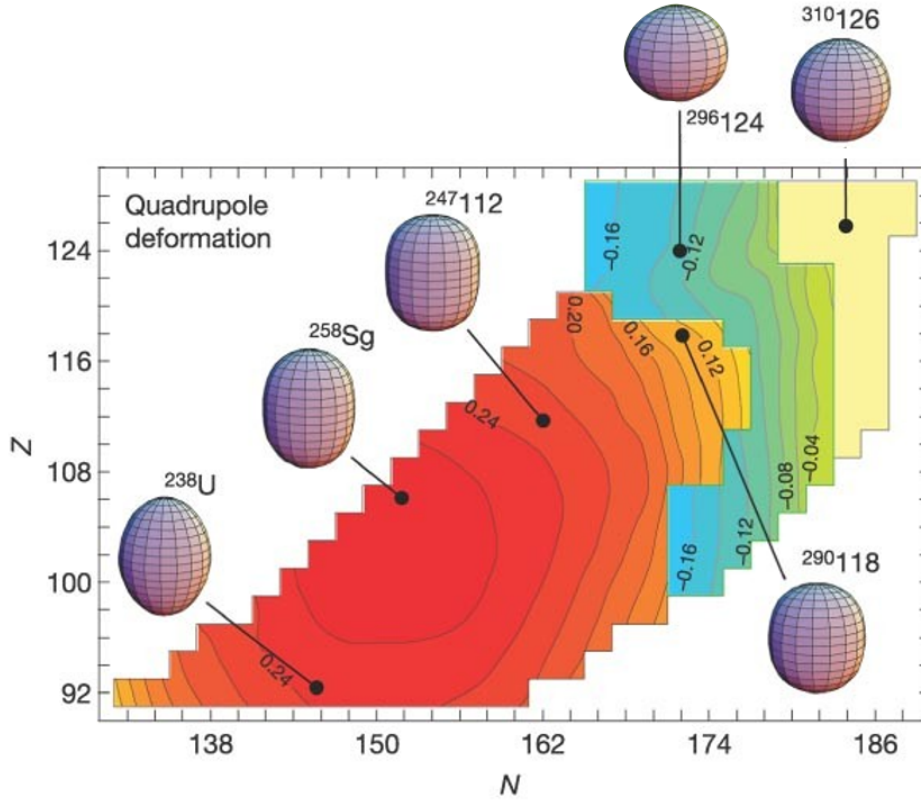


Figure 2.5: Predicted ground-state quadrupole deformation β_2 in the actinide region, taken from Ref. [3]. Prolate shapes ($\beta_2 > 0$) are indicated in red and orange, spherical shapes in yellow and oblate shapes ($\beta_2 < 0$) in blue and green.

2.4 Production of nuclei in fusion and separation

The periodic table of elements lists currently 118 elements [108], of which only elements up to $Z = 94$ occur naturally through the solar r-process [109]. The limit of natural production lies therefore in the actinides, the elements between $Z = 89$, actinium, and $Z = 103$, lawrencium. The transactinides beyond ${}_{103}\text{Lr}$ are called SuperHeavy Elements (SHE). In the region of heavy and superheavy nuclei with a proton number of $Z \geq 100$, the nuclei can only exist due to their

2 Theoretical background

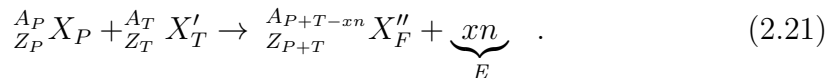
underlying shell structure, which hinders spontaneous fission. Moreover, with increasing Z , relativistic effects on the electronic structure gain importance. In the following sections, the production of actinides by fusion-evaporation reactions and the separation at the velocity filter SHIP at GSI are briefly explained.

2.4.1 Fusion evaporation reaction

Up to $_{100}\text{Fm}$, elements can be produced in high-flux reactors [110]. Beyond $Z=100$, transfermium elements are generated by fusion-evaporation reactions. In general, fusion-evaporation reactions follow the mechanism of nucleon transfer. A projectile P is accelerated to $\approx 0.1\%c$ onto a target T , such that it can overcome the Coulomb barrier of about 5 MeV/u and is captured. c is hereby the speed of light. A compound nucleus C^* may form, that is stable for $10^{-14} - 10^{-19}$ s, which is long compared to the flyby time of the projectiles of about 10^{-22} s. C^* deexcites by evaporation of light ejectiles E to the final product F , the evaporation residue, whereby this process is challenged by spontaneous fission. The total reaction is given by [111]



All projectile nucleons are transferred to the target. Typical ejectiles range from light nuclei to single nucleons, whereby most likely neutrons are evaporated, since they do not have to overcome the Coulomb barrier. The fusion-evaporation reaction follows therefore



There are several possible entrance channels to form the same compound nucleus, which itself can decay to different exit channels. The reaction for any chosen channel can be predicted by a classical two-body potential model, which is derived from the liquid drop model [112]. Whether a fusion-evaporation reaction occurs depends strongly on the individual reaction cross section of the projectile and the target as well as the angular momentum for the fusion. The cross section of a chosen channel is thereby a product of the creation cross section of the compound nucleus and the branching ratio to that channel. The competition between fission and neutron evaporation of C^* has to be taken into account, such that the final production cross section is determined by the product of the fusion cross section and the survival probability [6]. The angular momentum content of the compound nuclear system depends on the bombardment energy, which is determined by the entrance channel of the fusion reaction. The energy dependence of the reaction cross section on the kinetic energy of the projectile is given by so-called excitation functions. HIVAP-code-calculated excitation functions [113], [114] for the fusion-evaporation reactions $^{208}\text{Pb}(^{48}\text{Ca}, xn)^{(256-x)}\text{No}$, which was used for indirect production of ^{250}Fm , are given in Fig. 2.6.

Depending on the excitation energy of the compound nucleus E_{C^*} , fusion-evaporation reactions are classified in two different ranges. Cold-fusion reactions

2 Theoretical background

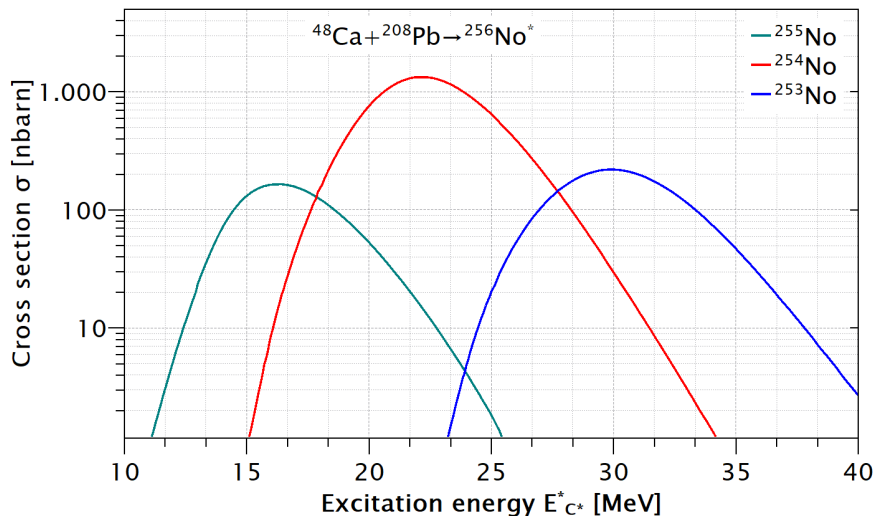


Figure 2.6: Excitation functions for $^{208}\text{Pb}(^{48}\text{Ca},xn)^{(256-x)}\text{No}$ calculated from HIVAP-code [113], [114]. The 1n, 2n and 3n exit channels are shown in green for ^{255}No , red for ^{254}No and blue for ^{253}No , respectively. Figure adapted from Ref. [115].

occur for medium-mass-ion projectiles impinging on Pb or Bi targets [116], resulting in $E_{C^*}^* \approx 10\text{--}20$ MeV. Hot fusion reactions, which are achieved by the fusion of light beams, e.g. ^{48}Ca with actinide targets, lead to an excitation energy of $E_{C^*}^* \approx 30\text{--}40$ MeV [117]. For cold fusion, the fusion reaction has an increased fusion hindrance at the barrier, which is compensated by low excitation energies of the compound nucleus due to the magic character of the target. One to two neutrons are evaporated from the evaporation residue. In hot-fusion reactions, the fusion hindrance at the barrier is lower, but the excitation energy is higher such that the compound nucleus has to evaporate 3-5 neutrons to form the evaporation residue [118]. Regardless of the $E_{C^*}^*$ classification, the production cross section generally decreases with increasing Z [116]. Fusion evaporation reactions for the generation of heavy elements cannot lead to the formation of neutron rich isotopes. For fermium, neutron rich isotopes can be produced by reactor breeding.

2.4.2 Fusion evaporation production of Fm isotopes

Up to fermium, some long-lived actinide isotopes can be produced in macroscopic amounts by reactor breeding. Hereby, macroscopic samples of the neutron-rich fermium isotopes $^{255,257}\text{Fm}$ are bred via neutron capture and subsequent β^- decay, starting from ^{248}Cm . Through this technique, the most neutron-rich fermium isotope presently accessible, ^{257}Fm , is reachable.

Fusion evaporation reactions, as described in Sec. 2.4.1, are another possibility to produce fermium isotopes. Particular cold fusion can be exploited for the production of neutron deficient Fm isotopes up to ^{241}Fm , but is also applicable

2 Theoretical background

for neutron rich Fm isotopes between ^{253}Fm and ^{256}Fm .

However, the direct production cross section of fermium isotopes is very small. The study of excitation functions for the production of different neutron rich Fm isotopes by bombardment of ^{248}Cm with ^{40}Ca and ^{44}Ca at different energies showed a maximum cross section of $20.9 \mu\text{b}$ for ^{252}Fm , $13.2 \mu\text{b}$ for ^{253}Fm , $4.5 \mu\text{b}$ for ^{254}Fm and $0.34 \mu\text{b}$ for ^{256}Fm [119]. Previously used production reactions for neutron deficient fermium isotopes have shown a cross section of about 10 nb for the reactions $^{204}\text{HgS}(^{48}\text{Ca}, 2\text{n})^{250}\text{Fm}$ and $^{202}\text{HgS}(^{48}\text{Ca}, 2\text{n})^{248}\text{Fm}$ [103]. In 1967, the reaction $^{239}\text{Pu}(^{12}\text{C}, 4\text{n})^{247}\text{Fm}$ was successfully implemented with a cross section of $0.2 \mu\text{b}$ [120]. The fusion-evaporation reactions $^{208}\text{Pb}(^{40}\text{Ar}, 2 - 4\text{n})^{246,245,244}\text{Fm}$ show a cross section of $11 \pm 2 \text{ nb}$, 32 nb and 1.7 nb , respectively [102], [121], [122]. The production cross section of ^{244}Fm can be increased to 3.6 nb , when the reaction $^{207}\text{Pb}(^{40}\text{Ar}, 3\text{n})^{244}\text{Fm}$ is used. By changing the lead isotope in the target to ^{206}Pb or ^{204}Pb , even ^{243}Fm and ^{241}Fm are directly accessible in a 3n-exit reaction channel [121], [122].

2.4.3 Isotope production at SHIP

At the GSI in Darmstadt, the velocity filter SHIP (Separator for Heavy Ion reaction Products) [66], [123] enables the production and subsequent separation of heavy fusion-evaporation residues from the primary beam. The SHIP setup starts with a segmented rotating target wheel, on which target foils of typically 0.5 mg/cm^2 are inserted. Through the rotation, a cooling of the target foils and an enlarged beam-on-target surface can be obtained simultaneously. A beam of projectiles is accelerated from the UNiversal Linear ACcelerator (UNILAC) onto the target wheel such that a cold fusion reaction can occur. The primary beam has hereby a kinetic energy of about 5 MeV/u and time-averaged beam intensities of a few 10^{12} ions/s [124]. The separation of the recoiling fusion products from the primary beam is achieved by crossed static electric and magnetic fields of SHIP, which acts as a Wien filter [123]. Quadrupole lenses ensure a focusing of the beam.

For cold fusion of, e.g., ^{254}No , the reaction $^{208}\text{Pb}(^{48}\text{Ca}, 2\text{n})^{254}\text{No}$ is used. The Pb target foils are mounted on the segmented turning wheel comprising 8 PbS segments with a thickness of $440 \mu\text{g/cm}^2$ [126]. The ^{48}Ca beam impinges on the target with a kinetic energy of 4.55 MeV/u at a beam intensity of about $0.7 \text{ particle microampere (p}\mu\text{A)}$, corresponding to $\sim 4.4 \cdot 10^{12}$ particles per second [127]. The reaction cross section σ is in the order of $\sim 2 \mu\text{b}$, such that about 17 particles per second are produced at the target, of which about 4 particles per second arrive at the experimental setup. In comparison, the background rate originating from transfer products is negligible (1 ion/min for a beam intensity of $1 \text{ p}\mu\text{A}$) [128]. A schematic view of SHIP is given in Fig. 2.7.

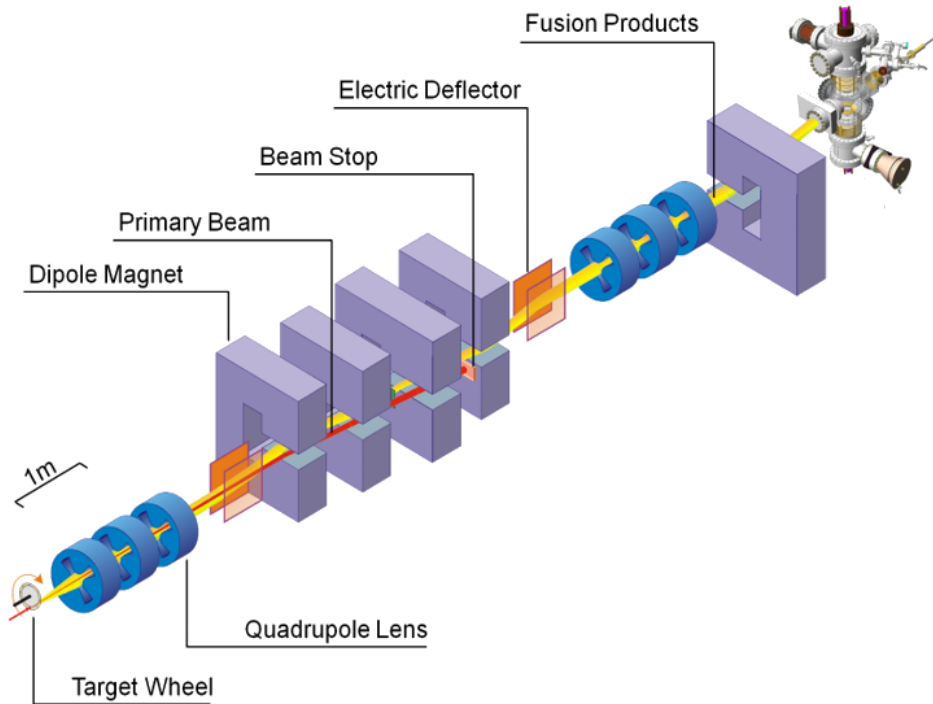


Figure 2.7: Schematic setup of SHIP with the target wheel, the velocity separation of the fusion product from the unwanted species and the RADRIS buffer-gas stopping cell. Picture adapted from Ref. [125]

2.5 Laser spectroscopy

Laser spectroscopy is a well established experimental method, that provides a unique access to observables that are affected by nuclear shell effects [33]. State-of-the-art experiments as in-beam nuclear spectroscopy [16], radioactive decay studies [129], Conversion Electron (CE) spectroscopy [130], and γ -ray measurements [75] are established methods to gain an insight on the nuclear structure. Moreover, laser spectroscopy has proven to be a suitable tool to investigate the electronic structure of various isotopes.

Spectroscopy can be performed in traps or gas cells and ion guides. The investigated ions can be stable, but also far from stability produced by fission, fragmentation, spallation or fusion-evaporation. In the latter cases, the kinetic energy of the ions has to be reduced to enable an appropriate handling for subsequent spectroscopy investigation. Mostly, buffer gas cells are used in combination with solid degraders to thermalize high-energetic recoil nuclei.

In case of spectroscopy in traps, Magneto-Optical atom Traps (MOT) and ion traps like Paul traps have shown their power for high precision spectroscopy.

The most frequently used possibility for spectroscopy of radionuclides is collinear laser spectroscopy, for which the laser light is either co- or counter propagating to the ion beam [8], [131]. Collinear laser spectroscopy enables spectroscopy with

2 Theoretical background

a high accuracy on an excited state, whereby the fluorescence decay from this state can be exploited for the detection. The transition frequency is thereby Doppler shifted, such that either the ion velocity or the laser frequency can be scanned to find the resonance [132]. However, fluorescence detection is challenged by low efficiency and background photons from the scattered laser light [133]. Another possibility is the use of Resonance Ionization Spectroscopy (RIS) or the combination of both: Collinear RIS (CRIS). Resonance ionization spectroscopy exploits the unique atomic level fingerprint and can be applied by exciting the atom of choice either directly to continuum, to an auto ionizing state, or to a Rydberg state (see Sec. 2.5.4). RIS is applicable for studies of nucleides available with low production rates of about 10 s^{-1} and short half-lives of $\sim 1 \text{ ms}$ [134]. Successful experimental setups for in-gas cell spectroscopy are, e.g., RADRIS (see Sec. 2.5.5).

In this section, basics of optical spectroscopy and the RADRIS method will be introduced.

2.5.1 Atomic transitions

Atomic transitions occur between possible discrete electronic levels E and E' of the atom by absorbing or emitting a photon, such that [29]

$$E_{\text{phot}} = h\nu = h\frac{c}{\lambda} = \Delta E = E' - E \quad . \quad (2.22)$$

The photon emission can either be induced or happen spontaneously. Only in the case of induced emission, the resulting photon features the same frequency, phase and direction as the evoking photon. Since the electronic structure is characteristic for every element and even isotope, the respective emission or absorption spectra provide the possibility for element identification.

The change in the population density from the ground state 1 to the excited state 2 in a closed 2-level system is given by [29]

$$\frac{dN_1}{dt} = N_2 A_{21} + N_2 B_{21} \rho(\nu_{21}) - N_1 B_{12} \rho(\nu_{12}) \quad , \quad (2.23)$$

with the Einstein coefficient for spontaneous emission A_{21} and induced emission and absorption B_{21} and B_{12} , respectively, and the density of photons ρ with the transition frequency $\nu_{12} = \nu_{21}$. In case of thermal equilibrium, the state occupation follows a Boltzmann distribution [135]. Exploiting this behaviour, one finds a link between A_{21} and B_{21} [29]:

$$A_{21} = \frac{8\pi h\nu^3}{c^3} B_{21} \quad . \quad (2.24)$$

Generally, the Einstein coefficient of an atomic transition A_i is linked to the lifetime τ_i of the atomic state by $\tau_i = 1/A_i$ and therefore provides a measure on the strength of the transition.

2.5.2 Natural linewidth

Every atomic transition has a non-zero minimal natural line width due to the energy and lifetime uncertainty of the state, which are linked by the Heisenberg uncertainty relationship $\Delta E \cdot \Delta t \geq \frac{\hbar}{2}$. When an excited state deexcites with emission of a photon, the corresponding intensity distribution $I(\omega)$ follows a Lorentz profile:

$$I(\omega) = I_0 \frac{\gamma/2\pi}{(\omega - \omega_0)^2 + (\gamma/2)^2} . \quad (2.25)$$

This results in a Full Width at Half Maximum (FWHM) $\gamma = A_i = \frac{1}{\tau_i}$, which is the natural linewidth at 1/2 of the maximum intensity I_0 at the central angular frequency $\omega_0 = 2\pi\nu_0$ with the natural frequency linewidth ν_0 . Since an atomic transition involves two states i and k , the energy and lifetime uncertainties are combined to give the natural linewidth $\delta\omega_n = \frac{1}{\tau_i} + \frac{1}{\tau_k}$. For a typical lifetime on the order of 10^{-9} to 10^{-6} s the natural linewidths are in the range from 160 kHz to 160 MHz.

2.5.3 Broadening processes

Even with high-resolution spectroscopy, it is often impossible to resolve the natural linewidth of a transition due to broadening processes. One of the main contributions to spectral broadening is the Doppler effect, which emerges from the thermal movement of the atom and is normally on the order of several GHz [35]. Since the atom moves with velocity \vec{v} relative to a detector or a light source with a wave vector \vec{K} , the absorption and emission frequencies in the lab frame, ω_a and ω_e , respectively, change to

$$\omega_e = \omega_a = \omega_0 + \vec{K}\vec{v} . \quad (2.26)$$

Since the direction of the movement is random, the resulting intensity is given by a Gaussian distribution [135]:

$$I(\omega) = I(\omega_0) \cdot \exp\left[-\left(\frac{c(\omega - \omega_0)}{\omega_0\sqrt{2k_B T/m}}\right)^2\right] = I(\omega_0) \cdot \exp\left[-\left(\frac{c(\omega - \omega_0)}{\omega_0 v_m}\right)^2\right] . \quad (2.27)$$

The most probable velocity $v_m = \sqrt{2k_B T/m}$ results from a Boltzmann distribution of the velocities of the involved atoms. The full width at half maximum amounts to [27]

$$\delta\omega_D = \frac{2\omega_0 \cdot v_m}{c} \sqrt{\ln(2)} . \quad (2.28)$$

One can easily see, that the spectral width due to Doppler broadening is influenced by the experimental conditions such as the temperature of the ensemble, the mass of the atom, and the transition frequency. The convolution of the Lorentz profile from the natural linewidth and the Gauß profile from the Doppler broadening results in a Voigt profile [29].

2 Theoretical background

Another broadening process is the intensity or saturation broadening, which is caused by the change in occupation densities due to optical pumping. When intensity exceeds the maximum of the saturation parameter S , defined by the ratio of the excitation rate W_{12} to relaxation rate R_1 , off-resonant contributions to the spectral line increase. The broadened intensity distribution $I_s(\nu)$ can be expressed by [136], [137]

$$I_s(\nu) = \frac{\frac{W_{12}}{R_1} \cdot I(\nu)}{1 + \frac{W_{12}}{R_1} \cdot I(\nu)} = \frac{S \cdot I(\nu)}{1 + S \cdot I(\nu)} \quad (2.29)$$

with the unsaturated intensity $I(\nu)$. If spectroscopy is performed in a gaseous atmosphere, pressure broadening comes into play. Due to collisions of the gas with investigated atoms, the energy levels can broaden. Additionally, elastic collisions between the gas and the atoms lead to a pressure shift. The shift itself depends on the distance r between the two interaction partners 1 and 2, such that

$$h\nu_{12} = |E_1(r) - E_2(r)| \quad . \quad (2.30)$$

The distances r are statistically distributed, such that the mean value is shifted in comparison to the vacuum spectrum. Additionally, photons may be emitted due to relaxations after collisions and thus the effective lifetime of the level is reduced, which increases the linewidth. The collision rate and consequently the broadening depends on the density and temperature of the gas.

Also, the bandwidth of the laser may limit the achievable resolution. Widely-used dye lasers, for example, have a rather large spectral bandwidth up to 10 GHz [138], whereas modern solid-state, optical fiber, and semiconductor lasers can feature bandwidths of down to a few Hz [139].

To reduce the bandwidth of broadband lasers, a wavelength dependent transmission filter like a Fabry-Perot etalon can be used [135].

2.5.4 Laser resonance ionization spectroscopy

For simplicity reasons, only Resonance Ionization Spectroscopy (RIS) of neutral atoms will be explained in more detail, since it is crucial for the laser spectroscopy of Fm isotopes.

Laser resonance ionization spectroscopy is a very efficient, sensitive, and element selective tool used in atomic structure investigations. In either two or three-step ionization schemes, a valence electron is stepwise excited from the ground state over one or more excited states to get over the ionization potential by exposing the atom to laser beams of precisely tuned frequencies. In Figure 2.8, three different possible excitation schemes are shown. Since the energy of the excitation levels scales with the main quantum number $E_n \propto 1/n^2$ (see Eq. 2.4), the transition wavelength for the first step ranges from 300 – 500 nm, while the final excitation step is located in the red to infrared region around 650 – 900nm.

2 Theoretical background

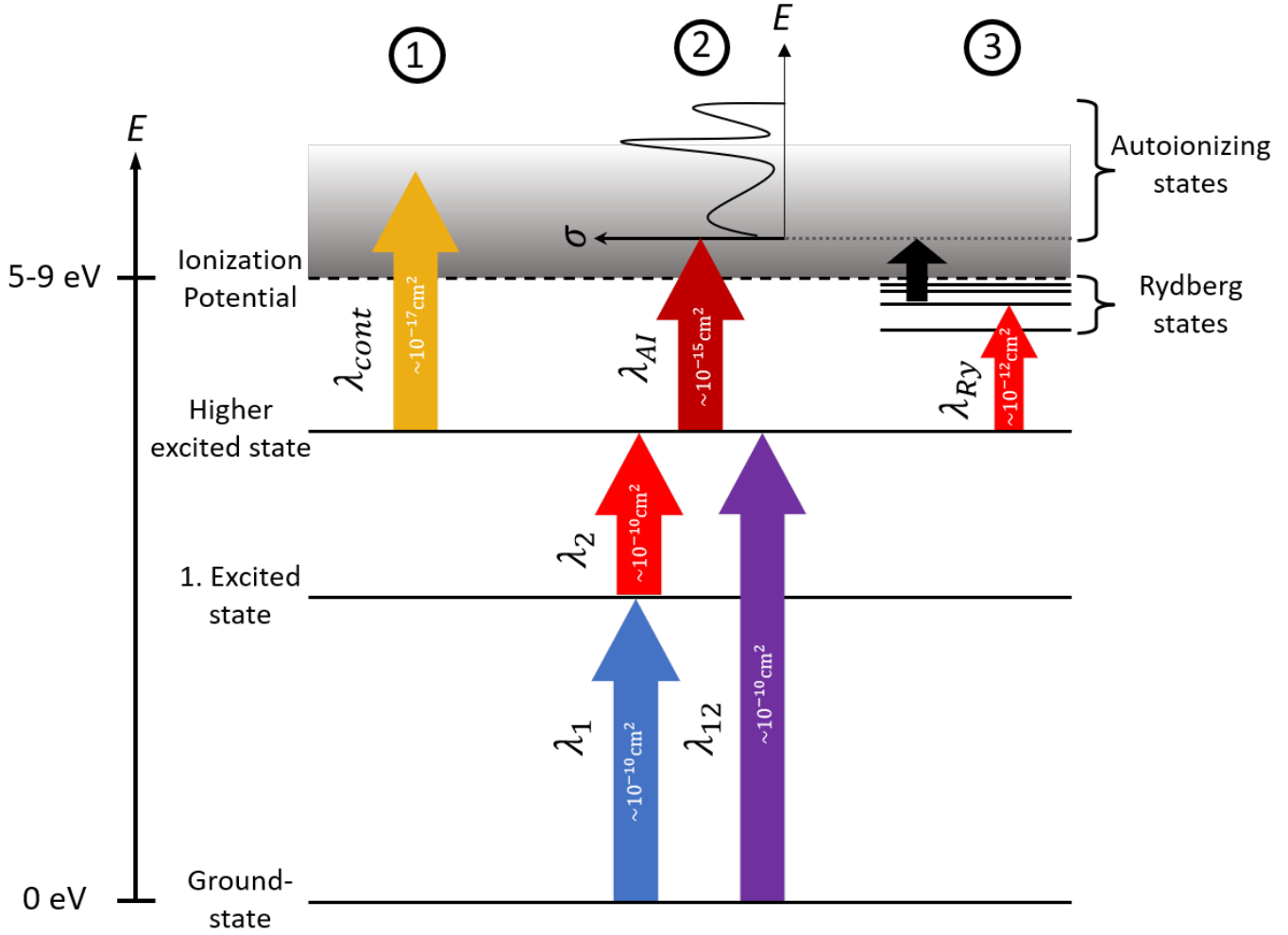


Figure 2.8: RIS: Three different ways for laser ionization. A valence electron is excited in one or more steps to above the ionization potential. The final excitation can be non resonant to the continuum (case 1), or resonant to an auto ionizing state (case 2) or to a Rydberg state close to the IP (case 3). Picture adapted from Ref. [140].

Irrespective of the choice of two or three-step ionization, the ground-state transitions need to be strong such that minimum laser power is needed to saturate the transition. Typically, photon fluxes in the order of about $10^{18} \frac{\text{photons}}{\text{cm}^2 \cdot \text{s}}$ are required, such that pulsed lasers are preferably used to saturate the transition. The timing of the consecutive steps is thereby crucial in particular for strong transitions of lifetimes in the ns regime.

The efficiency of laser resonance is often limited by the final ionizing step. In the case of non-resonant ionization to the continuum (1) the typical absorption cross-section for photons is on the order of $\sigma_{cont} \propto 10^{-17} \text{cm}^2$, which is the least efficient of the three scenarios. However, other possibilities are not applicable for initial level search while studying heavy and superheavy atoms, where knowledge

2 Theoretical background

of excitation schemes is sparse. To increase the ionization probability for case ①, the photon flux can be increased by using high power pulsed laser systems to compensate for smaller cross sections [135].

Another possibility is provided by resonant excitation to so-called Auto Ionizing states (AI, case ②). For multi-electron atoms, electromagnetic correlations between the electrons lead to short-lived resonant states above the ionization potential, which decay to an electron-ion pair. The excitation cross section to an auto ionizing state is roughly two orders of magnitude larger compared to scenario ①.

Even higher cross sections of up to $\sigma_{Ry} \propto 10^{-12} \text{cm}^2$ can be obtained by exciting the electron to high-lying weakly bound states, so-called Rydberg states (case ③). Since they are very close to the IP, ionization can take place by energy transfer by collisions (e.g., by surrounding gas), application of external fields, random pickup of involved photons, or heat transfer in case of a hot surrounding (e.g., due to a hot cavity). Given many Rydberg levels are known, the respective energies can be precisely described by the extended Rydberg-Ritz formula which enables to determine the ionization potential of the element [29], [141].

In this work, two step resonant laser ionization was used for level searches in different Fm-Isotopes. The spectral linewidth of the observed resonances is thereby strongly influenced by the laser bandwidth and broadening effects mentioned in Sec. 2.5.3. For ion mobility studies, the known excitation schemes will be exploited to resonantly ionize neutral actinides of choice to measure their drift behaviour and to conclude their ion mobility in noble gases.

2.5.5 The RADRIS method

To investigate the nuclear structure of heavy elements, laser spectroscopy was implemented at the GSI Helmholtzzentrum für Schwerionenforschung in Darmstadt by the development of the RADIation Detected Resonance Ionization Spectroscopy (RADRIS) technique [142]. It features high efficiency and selectivity for α -decaying nuclides and has proven ideal for nobelium laser spectroscopy [15], [16], [127].

For the RADRIS technique, the actinide isotope of choice is produced on-line in a fusion-evaporation reaction before the recoil nuclei are separated from the primary beam in the velocity filter SHIP (see Sec. 2.4.3). The transmitted fusion products enter the buffer gas stopping cell through an entrance window. The entrance window foil thickness is hereby chosen to have the optimal degrader properties for the incoming fusion products. In the gas stopping cell, the fusion products are thermalized in argon gas of ≈ 90 mbar and guided by electric fields to a catcher filament. On the filament, the ions are accumulated and neutralized. The accumulation time depends hereby on the lifetime of the investigated isotope and, in case of an indirect production reaction by α decay, on the half-life of the respective daughter nuclide. After a sufficient accumulation on the filament, the

2 Theoretical background

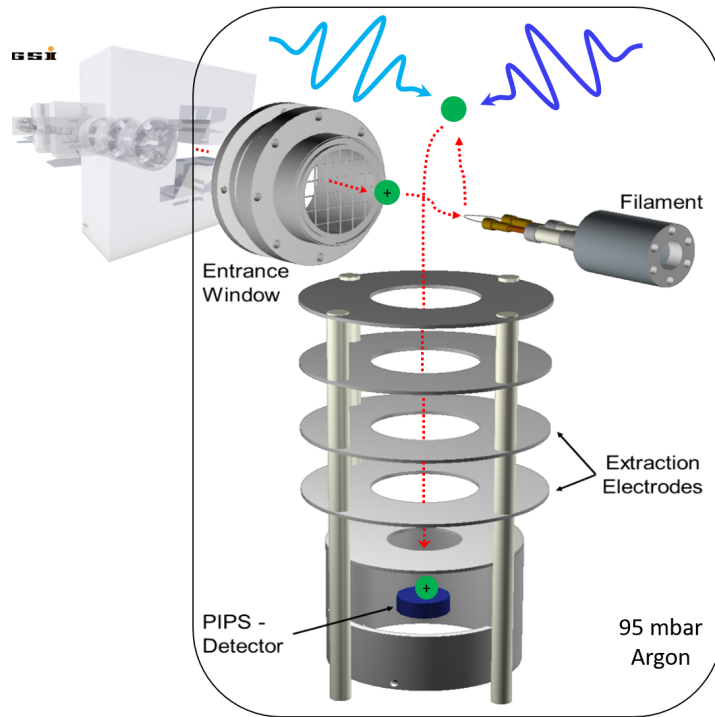


Figure 2.9: Schematic view of RADRIS method. The fusion products enter the gas cell, are thermalized and electrostatically guided to the filament. After neutralization, they are evaporated and two-step ionized. Finally, the photo-ions are guided to the PIPS detector and detected by their characteristic α decay energy. Figure adopted from Ref. [15].

collected neutral atoms are evaporated by a heatpulse and two-step laser resonance ionization spectroscopy is performed. The filament material, but also the desorption temperature is hereby element dependent [143]. In this way produced ions are guided via extraction electrodes to a Passivated Implanted Planar Silicon detector (PIPS), where they are finally detected via their characteristic α -decay energy. During the scan, at each wavenumber, the cycle of collection, ionization, and detection is performed. A schematic view of the RADRIS method is shown in figure 2.9.

To ionize the evaporated atom, a two-step scheme provided by a high-power laser system described in Sec. 3.1.3 is used.

2.6 Ion mobility spectrometry

Ion mobility spectrometry is a very powerful method to study the interaction of (actinide) ions with neutral buffer gas. In the following sections, the theoretical background of ion mobility spectrometry is explained. More detailed information is given in Ref. [144], [20] and [145].

2.6.1 Diffusion, drift and mobility

Ion Mobility Spectrometry (IMS) is a standard method in analytics and has a wide range of application areas from structural chemistry, forensics, homeland security, to environmental analysis [20]. In fundamental research, IMS can be used to elucidate the transport properties of ions in dilute gases and thus, gain insights into the ion-neutral interaction and the electronic configuration of the sample ion.

By measuring the drift time t_D of an ion of choice in a uniform electric field E of a given length L through a given gas environment, the ion mobility parameter K can be obtained. The recurrent acceleration due to the electric field and the deceleration due to collisions with the gas atoms lead to a constant drift velocity [144]

$$v_D = \frac{L}{t_D} = K \cdot E \quad . \quad (2.31)$$

The mobility K is hereby not only dependent on the temperature and the pressure of the gas, but also on the mass and the collision cross section of the sample ions with the gas atoms. The diffusion equation $J = -D|\nabla n_i|$, which describes the ion motion at low ion cloud densities n_i without a temperature gradient, electric or magnetic fields, chemical reactions, has to be generalized to take the mobility into account

$$J = -D|\nabla n_i| + n_i K \cdot E \quad . \quad (2.32)$$

∇n_i is hereby the ion-density gradient, D is the diffusion coefficient, and J is the ion flux. For singly charged ions, this leads to the Einstein equation

$$K = \frac{eD}{k_B T} \quad . \quad (2.33)$$

Overall, the ion motion is a superposition of drift along the field lines, a longitudinal diffusion along the electric field D_L , which leads to a spread in the arrival time distribution and a transversal diffusion D_T which contributes to possible ion losses. Both D_L and D_T are intrinsic parameters, which depend on the electric field. Density and temperature gradients in the drift volume and the Coulomb repulsion between the drifting ions lead to an additional spread of the ion cloud. To allow comparisons of mobilities of different species at different temperatures and pressures, the reduced mobility K_0 is defined as

$$K_0 = K \frac{P}{P_0} \frac{T_0}{T} \quad , \quad (2.34)$$

with the mobility K obtained at pressure P and temperature T , with $P_0 = 1013.25$ mbar = 760 Torr and $T_0 = 273.16$ K. In this way, K_0 is characteristic for given molecular and even elemental ions.

To compare different experiments, which are performed at varying electric field and different pressures, the ratio of the electrostatic field strength to the gas

2 Theoretical background

number density E/N (with $\sum_{i=0}^{\infty} n_i = N$) or the so-called reduced field is defined [144]. E/N can hereby be calculated from Ref. [146]

$$\frac{E}{N} = \frac{\Delta V}{LN_0} \left(\frac{P_0}{P} \right) \left(\frac{T}{T_0} \right) , \quad (2.35)$$

with the length of the drift tube L , the Loschmidt constant $N_0 = 2.68678 \cdot 10^{25} \text{ m}^{-3}$, and the potential difference over the drift region ΔV .

2.6.2 Gas kinetic theory

In general, the mobility is a function of E/N . Since the gas can be assumed to be isotropic, K can be expanded to [144]

$$K(E) = K(0) \left[1 + \alpha_1 \left(\frac{E}{N} \right)^2 + \alpha_2 \left(\frac{E}{N} \right)^4 + \dots \right] , \quad (2.36)$$

with higher order corrections α_1 and α_2 .

To conclude approximate results on the behaviour of v_D at different reduced fields and gas mixtures, the collision cross section Q is introduced. All possible ion-neutral collisions are covered by set of $Q^{(l)}$, whereby usually a classical mechanics description with the index $l = 1$ is sufficient. It describes the momentum transfer by elastic collisions

$$Q^{(1)} = 2\pi \int_0^{\infty} (1 - \cos \theta) b db , \quad (2.37)$$

with the impact parameter b and scattering angle θ in an ion-neutral collision with [147]

$$\theta = \pi - 2b \int_{r_a}^{\infty} \left[1 - \frac{b^2}{r^2} - \frac{V(r)}{\varepsilon} \right]^{-1/2} \frac{dr}{r^2} . \quad (2.38)$$

Here, r_a is the distance of closest approach, $V(r)$ is the ion-neutral interaction potential and ε the relative kinetic energy of the collision.

The interaction potential $V(r)$ takes a general form of

$$V(r) = \pm \frac{C_n}{r^n} , \quad (2.39)$$

for which C is a constant, $n = 2$ is the ion-dipole interaction, $n = 3$ the ion-quadrupole, $n = 4$ the ion-induced dipole, and $n = 6$ the ion-induced quadrupole interaction [144].

According to the Viehland and Mason theory [148], the mobility can be calculated from the reduced mass $\mu = \frac{mM}{m+M}$, the effective temperature T_{eff} , and the first order approximation of the momentum transfer collision integral $\Omega^{(1,1)}$:

$$K = \frac{3}{16} \frac{e}{N} \sqrt{\frac{2\pi}{\mu k_B T_{eff}}} \frac{1 + \alpha}{\Omega^{(1,1)}(T_{eff})} , \quad (2.40)$$

2 Theoretical background

with the mass of the ion and of the neutral counterpart m and M , respectively, the Boltzmann constant k_B , and a correction factor α . Since α is relatively small, it is negligible for heavy ions [149]. $\Omega^{(1,1)}(T_{eff})$ is a function of the effective temperature, according to

$$\Omega^{(1,1)}(T_{eff}) = \frac{1}{2(k_B T_{eff})^3} \int_0^\infty Q^{(1)}(\varepsilon) \exp(-\varepsilon/k_B T_{eff}) \varepsilon^2 d\varepsilon \quad . \quad (2.41)$$

The effective temperature T_{eff} is given by

$$\frac{3}{2} k_B T_{eff} = \frac{3}{2} k_B T + \frac{1}{2} M v_D^2 (1 + \beta) \quad , \quad (2.42)$$

whereby the correction factor β can be neglected in first order, such that the random energy of ions is given by a thermal motion part and an electric field part, which becomes less and less important with increasing ion mass m [20].

For molecular ions, the mobility parameter K reflects the size and shape of the ion [145]. In the case of monoatomic ions, K becomes sensitive to the ion mass, for lighter ions drifting in much heavier neutral gas. For heavy monoatomic ions, it becomes sensitive to the momentum transfer collision integral $\Omega^{(1,1)}$ [144]. In a simple hard-sphere model, the collision integral is given by $\Omega^{(1,1)}(T_{eff}) = \pi(r_{ion} + r_{gas})^2$ [20]. It was thought that mobility measurements can provide a measure on the ionic radii r_{ion} , but experimental results show that ion mobilities are dominated by ion-neutral interaction potentials [150].

2.6.3 Ion-neutral interaction potentials

The ion-neutral interaction potential $V(r)$ can only be given approximately by modelling the potential width and depth. This can be either deduced from experiment or predicted via *ab-initio* calculations [21]. A good approximation of $V(r)$ is in general given by an $(n, 6, 4)$ potential with one repulsion and two attraction terms:

$$V(r) = \frac{C_n}{r^n} - \frac{C_6}{r^6} - \frac{C_4}{r^4} \quad (2.43)$$

with the constants n , C_n , C_6 and C_4 . The term $\frac{C_n}{r^n}$ describes the short term repulsion energy, whereby n usually takes the value 8, 10, 12, or 16. The repulsion is also called Pauli repulsion, since the overlapping electronic shells of the ion and the neutral gas atom lead to large distortions of the charge density due to the Pauli exclusion principle. As a result of the electron shell distortion, the nuclear charges of the collision partners are not sufficiently screened and repel each other, which is described by the $\frac{C_n}{r^n}$ term. For $n = \infty$ the model would follow a rigid sphere model, as described in Ref. [20] [144] and [150].

As mentioned in Sec. 2.6.2, the $-\frac{C_6}{r^6}$ term describes the charge-induced quadrupole attraction plus the London dispersion attraction. The $-\frac{C_4}{r^4}$ term stands for the attraction between the charged ion and the dipole induced to the

polarizable neutral atom. For low temperatures and weak electric fields the inverse fourth power term dominates the mobility, as the collisions here occur at large distances in comparison to collisions in high electric fields at high temperatures with higher kinetic energies.

2.6.4 The AIMS method

Ion mobility spectrometers are in principle gas chromatographs coupled to mass spectrometers [151]. In the most simple case, the mass spectrometer consists of an ion-source, a mass analyser and an ion detector, whereby an ion source is placed in the carrier gas in case of IMS.

For ion mobility spectrometry investigations of singly charged lanthanide ions, a spectrometer was developed [150], which was adapted to be suitable for ion mobility studies across the actinides within the framework of this thesis. The setup was redesigned to be an Actinide Ion Mobility Spectrometer (AIMS). The mobility spectrometer consists of a drift chamber and a detection part, which is depicted in the schematic view of the AIMS setup in Fig.2.10.

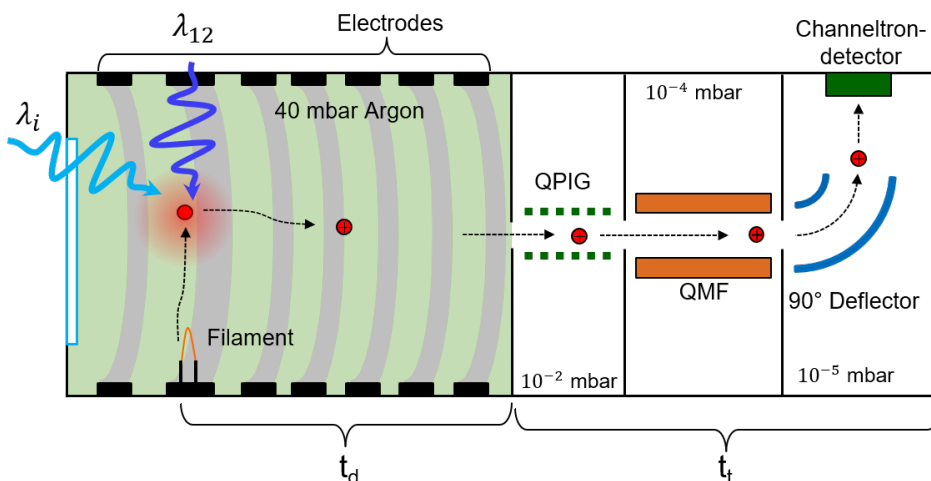


Figure 2.10: Schematic view of AIMS method. The atom is evaporated from the metal foil and resonantly ionized by two laser beams. The ion drifts through the gas in the electric field provided by the ring electrodes. After extraction through the nozzle, the ion is transported by a Quadrupole Ion Guide to a Quadrupole Mass Filter. The filtered ions are deflected to the channeltron detector.

Depending on the investigated actinide isotope, the ions can be produced off-line from thin metal foils by two-step ionization or the on-line produced ions enter the drift cell through an entrance window and are stopped in the buffer gas. In the drift chamber, the ions drift through the gas along the field lines towards the extraction nozzle. Due to the individual mobility, different ion species get separated in time from each other (see Sec. 2.6.1). After the extraction through the nozzle, the ions are guided to the detector. This is done by using a QuadruPole

2 Theoretical background

Ion Guide (QPIG), in which the ions are cooled in the surrounding gas, such that a proper centering of the ions is ensured. A Quadrupole Mass Filter (QMF) is used to select the mass-to-charge ratio of the wanted ion species, which are deflected by a 90° deflector towards the detector. Finally, the ions are detected by a channel electron multiplier detector (channeltron).

Since QPIG, QMF, deflector and detector are placed in a differential pumping section, the transit time t_t from extraction to detection is about two magnitudes smaller than the drift time t_d , such that it can be safely neglected [150]. The mean arrival time t_a is therefore approximately given by the drift time t_d by $\langle t_a \rangle = \langle t_d + t_t \rangle = \langle t_d \rangle + \langle t_t \rangle \approx \langle t_d \rangle$.

A more detailed description of the major components of this IMS apparatus is given in Sec. 5.5.

3 Fermium laser spectroscopy

Fermium was discovered in aerosols from the upper earth atmosphere after the thermonuclear explosion of the first hydrogen bomb in 1952 together with Einsteinium ($Z=99$) [152] by chemical isolation of the collected isotope ^{255}Fm ($t_{1/2} = 20.07$ h) by Ghiorso et al. [153]. Shortly after the discovery of ^{255}Fm , ^{254}Fm ($t_{1/2} = 3.24$ h) was produced by reactor breeding, starting from ^{239}Pu over ^{252}Cf and ^{254}Es [154], [155]. Independently, the first fusion evaporation reaction to produce fermium, $^{238}\text{U}(^{16}\text{O},4n)^{250}\text{Fm}$, succeeded [156]. Today, 20 fermium isotopes are known, between ^{241}Fm and ^{260}Fm , spanning half-lives from $370 \mu\text{s}$ (^{258}Fm) to 100.5 days (^{257}Fm) [157], [158]. The neutron deficient fermium isotopes thereby have to be produced by fusion evaporation reactions as described in Sec. 2.4.2, while the neutron rich isotopes ($N \leq 154$) can be bred in reactors with a high neutron flux.

Laser spectroscopy has the potential to give an insight in the nuclear structure by localizing shell gaps on the basis of observing sudden changes in nuclear moments or charge radii. An insight into the nuclear structure can be also obtained by $\alpha-\gamma$ coincidence spectroscopy [66].

The studied fermium isotopes allow us to probe the deformed $Z=100$ shell gap [76] and the $N=152$ deformed neutron shell gap by laser spectroscopy.

In the following sections, state-of-the-art RIS studies in the vicinity of $N=152$ are presented, then the laser spectroscopy procedure on fermium isotopes is explained, the results for $^{248,249,250}\text{Fm}$ are presented, and the extension of the experimental method to further fermium isotopes is discussed.

3.0.1 RIS studies in the vicinity of $N = 152$

While resonance ionization spectroscopy studies are well established for light nuclei even far from stability, RIS on heavy actinides is challenging due to a complex atomic level structure, short half-lives and limited availability. The reported atomic levels are sparse and need to be investigated, while theoretical atomic calculations become complicated due to open shell treatment [18].

The first successful on-line resonance ionization spectroscopy experiment in the vicinity of the deformed shell gap at $N=152$ was performed on $^{254}_{102}\text{No}$ [15]. Based on the discovered optical transition, laser spectroscopy studies have been performed in 2018 on $^{252,253,254}\text{No}$ ($Z=102$). Moreover, hyperfine spectroscopy of ^{253}No was performed, providing a measure on the hyperfine parameters

3 Fermium laser spectroscopy

Spectroscopic result	A_{HFS} [GHz]	B_{HFS} [GHz]
	0.734(46)	2.82(69)
Nuclear properties	μ [μ_N]	Q_S [eb]
	-0.527(33)(75)	+5.9(1.4)(0.9)
Isotope	$\delta\nu^{254,A}$ [GHz]	$\delta\langle r^2 \rangle^{254,A}$ [fm ²]
²⁵⁴ No ₁₀₂	0	0
²⁵³ No ₁₀₂	6.72(18)	-0.070(2)(5)
²⁵² No ₁₀₂	10.08(69)	-0.105(7)(7)

Table 3.1: Nobelium RIS results from Ref. [126].

A_{HFS} and B_{HFS} . The hyperfine structure coupling parameters B_e/J and $(\partial^2 V/\partial z^2)$, the field shift constant F_{FS} , and the mass shift constant K_{MS} have been calculated using different calculation techniques, including Configuration Interaction (CI) with the single-double coupled cluster method, CI combined with Many-Body Perturbation Theory (MBPT), relativistic Fock Space Coupled Cluster (FSCC) and Multi-Configuration Dirac-Fock (MCDF) calculation [127]. This enabled subsequently the extraction of nuclear magnetic moment μ , the spectroscopic quadrupole moment Q_S , and the changes in mscr $\delta\langle r^2 \rangle$ between the nuclei, enabling a complementary measure of the deformation of ^{252,253,254}No isotopes [126]. The obtained changes in the mean-square-charge radii enabled studies of changes in the nuclear size and shape [126], [127]. The comparison of the change of mscr to calculated values from self-consistent nuclear Density Functional Theory (DFT) showed good agreement. The results of the nobelium studies from Ref. [126] are given in Tab. 3.1.

Off-line in-source hot cavity laser spectroscopy was carried out for the neutron rich einsteinium isotopes ^{253,254,255}Es ($Z=99$) at the Resonance Ionization Spectroscopy in Collinear geometry (RISIKO) mass separator in Mainz. In the RISIKO setup, samples are heated in an atomiser. The evaporated neutral atoms are laser ionized, mass separated by a dipole magnet and finally detected by a Secondary Electron Multiplier (SEM). More details on the RISIKO mass separator are given in Ref. [159]. For einsteinium spectroscopy, a sample was provided from Oak Ridge National Laboratory (ORNL), containing ≈ 0.2 ng ²⁵³Es, ≈ 0.4 ng ²⁵⁴Es and ≈ 4 pg ²⁵⁵Es. In Mainz, the sample was dried on zirconium foil, then placed in the atomiser and spectroscopically analysed at RISIKO. The experiment enabled hyperfine structure studies of ^{253,254,255}Es and the extraction of the isotope shift. Moreover, the spins of ²⁵⁴Es and ²⁵⁵Es were assigned and the nuclear magnetic dipole moment μ and the spectroscopic quadrupole moment Q_S was extracted [160], [161]. However, changes in mean-square charge radii

3 Fermium laser spectroscopy

could not be extracted due to missing atomic theory calculations for the mass and field shift parameters K_{MS} and F_{FS} .

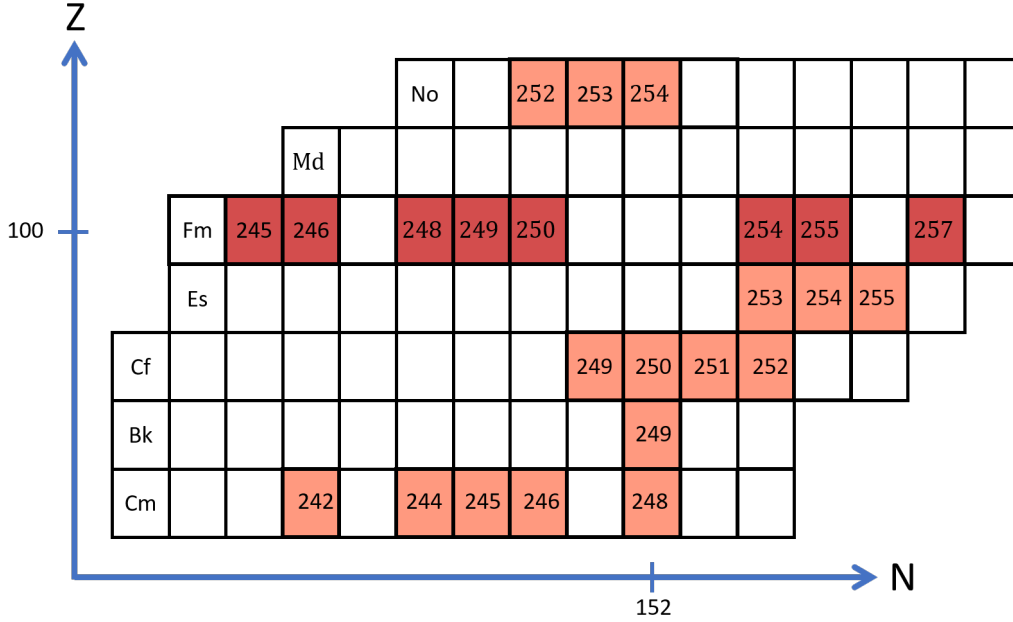


Figure 3.1: Part of the nuclear chart showing actinides around $N=152$ investigated by RIS. Different colours indicate the different states of RIS investigations: The fermium isotope chain including data from this work is highlighted in dark red.

$^{249-252}\text{Cf}$ ($Z=98$) isotopes in the vicinity of the $N=152$ shell are off-line accessible in mg quantities. Very recently, RIS performed at RISIKO on high-lying Rydberg states in $_{98}\text{Cf}$ helped to improve the determination of the first ionization potential of the element in 2022 [162]. Moreover, the isotope shift of the isotopic chain $^{249-252}\text{Cf}$ across the $N=152$ deformed shell gap was measured. However, no detailed quantitative analysis of the isotope shift could be performed due to a spectral resolution of about 2 GHz [162], which was limited by the Doppler broadening in the hot cavity and the laser bandwidth. Therefore, the hyperfine structure of ^{249}Cf and ^{251}Cf could also not be resolved. Nevertheless, the way towards high-resolution spectroscopy studies was paved. Even more recently, the spectral linewidth could be lowered to about 100 MHz for californium spectroscopy by using an injection-locked Ti:Sa laser [163]. Three atomic transitions were studied for the extraction of hyperfine parameters, nuclear magnetic dipole moments, spectroscopic quadrupole moments and variations in the isotope shift data. The change in mean-square charge radii could not be extracted due to missing theory input. Anyway, the variations in the isotope shift data have not revealed a kink at $N=152$. To gain a better overview on the evolution of mean-square charge radii in californium, both input from atomic

theory and from experiment for more neutron deficient californium isotopes are needed.

Earlier laser spectroscopy studies have been performed on the curium isotopes ^{242}Cm , $^{244-246}\text{Cm}$ and ^{248}Cm [164], [152] and on ^{249}Bk [165], [152], but no isotope shift studies have been performed to draw the change in m_{scr} from them. In Fig. 3.1, the spectroscopied actinides around $N=152$ are depicted. For elements with $Z > 102$, the atomic level search is still ongoing.

3.1 Experimental procedure for fermium laser spectroscopy

As mentioned in Sec. 2.3.3, rotational bands and K -isomers, which portend a quadrupolar deformation, are known to exist for the isotopes $^{247,248,250,251,252,254,256}\text{Fm}$ [118], [104], and $^{248,250,256}\text{Fm}$ [103], [101], respectively. The deformation parameter β_2 is derived to be $\beta_2 = 0.28$ for ^{252}Fm [104] and $\beta_2 = 0.296$ for ^{250}Fm [44], while the change for neighboring isotopes amounts to $\Delta\beta \sim 0.02$ [44]. The hypothetic doubly magic nucleus ^{284}Fm is expected to feature a spherical shape.

To study the vicinity of deformed nuclei with the $Z=100$ sub shell gap and the $N=152$ deformed neutron shell gap, laser spectroscopy of ^{100}Fm isotopes provides a suitable tool. To gain an insight into the mean-square charge radii of the neutron deficient fermium isotopes $^{248,249,250}\text{Fm}$ in the vicinity of the $N=152$ shell gap, isotope shift measurements are performed on an atomic transition found in previous laser spectroscopy studies [136]. In the following sections, the production of different fermium isotopes, spectroscopic investigations of the $5f^{12}7s7p\ 5G_6^0$ state and conclusions based on the measurements are described.

3.1.1 First laser spectroscopy of ^{255}Fm

In 2003, laser spectroscopy was successfully applied to measure atomic transitions of ^{255}Fm for the first time [136]. Since no atomic levels were known above ^{99}Es back then, the measurements marked also a test for the predictive power of theoretical atomic calculation [134]. A 1.7 ng ^{255}Fm radionuclide sample was produced at the High Flux Isotope Reactor (HFIR) at ORNL. About 2×10^{10} ^{255}Fm atoms were electrochemically deposited on tantalum filaments and sputtered with a 1 μm titanium layer. The primed tantalum samples were spectroscopically analyzed in Mainz with a setup called Ion Guide-detected Resonance Ionization Spectroscopy (IGRIS). IGRIS was a modification of RADRIS using mass-selected ion detection to be able to perform spectroscopy on ^{255}Fm ($t_{1/2} = 20.1\text{ h}$). The atomic level structure was scanned between 24703–25990 cm^{-1} with a tunable dye laser (FL2002) pumped by a

3 Fermium laser spectroscopy

Nd:YAG(Continuum Powerlite 8050). The non-resonant second step at 351/353 nm was provided by a pulsed excimer-pumped laser (EMG104 MSC). The level search revealed two transitions at an excitation energy of $\bar{\nu}_2 = 25099.8 \pm 0.2 \text{ cm}^{-1}$ and $\bar{\nu}_1 = 25111.8 \pm 0.2 \text{ cm}^{-1}$. The levels were classified by comparisons to relativistic Multi-Configuration Dirac-Fock (MCDF) calculations. For the ground state, the configuration $5f^{12}7s^2 \ ^3H_6^e$ was assigned. The excited levels were assigned to the $5f^{12}7s7p \ ^5I_6^0$ and $^5G_5^0$ term, respectively. Moreover, a wave number scan revealed five further levels at 27389 cm^{-1} , 27466 cm^{-1} , 28158 cm^{-1} , 28377 cm^{-1} , and 28391 cm^{-1} , with a respective uncertainty of 1.5 cm^{-1} [166].

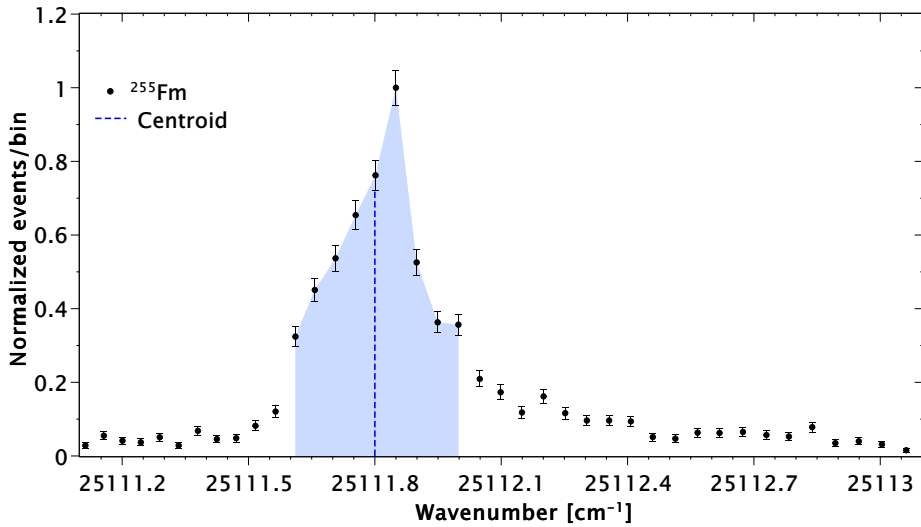


Figure 3.2: Scan over $5f^{12}7s7p \ ^5G_5^0$ transition of ^{255}Fm , taken from Ref. [134], [166]. The centroid (dashed blue line) was located at $25111.8 \pm 0.2 \text{ cm}^{-1}$. The stated uncertainty of the center position is shown in light blue around the centroid.

The hyperfine structure resulting from the unpaired neutron (see Sec. 2.1.4) could not be resolved due to a broad bandwidth of the scanning laser. With an assigned spin of $I = 7/2^+$ [167] and an respective angular momentum of $J = 6$ and $J = 5$ for the ground state and the excited state [44], 21 hyperfine components are expected. The sample contained also about $2 \times 10^9 \ ^{257}\text{Fm}$ atoms, too little for successful spectroscopy with that approach at the time. Therefore, no comparison of the centroid position of the transition of $^{255}_{100}\text{Fm}$ and $^{257}_{100}\text{Fm}$ was obtained. The scan over the $5f^{12}7s7p \ ^5G_5^0$ transition of $^{255}_{100}\text{Fm}$ taken from Ref. [134], [166] is depicted in Fig. 3.2.

Recent atomic theory calculations predicted the hyperfine constants A_{HFS} and B_{HFS} in ^{255}Fm for the transition $5f^{12}7s7p \ ^5G_5^0$ to [44]: Moreover, the calculations provided values for the field shift parameter F_{FS} and thus allowed the evaluation of changes in the nuclear mean charge radii (see Sec. 3.2.5).

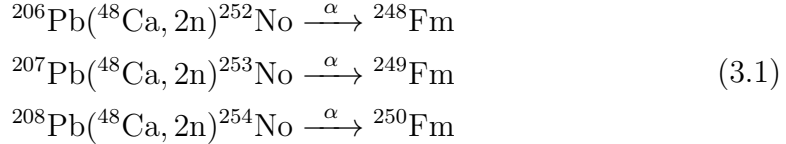
3 Fermium laser spectroscopy

$\bar{\nu}_{\text{expt}}$ [cm ⁻¹]	$\bar{\nu}_{\text{theor}}$ [cm ⁻¹]	$A_{\text{HFS,theor}}$ [MHz]	$A_{\text{HFS,expt}}$ [MHz]	$B_{\text{HFS,theor}}$ [MHz]	$B_{\text{HFS,expt}}$ [MHz]
25111.80	25494	195 g_I	-690 -730	-1823 Q	-1700 -390

Table 3.2: Hyperfine parameters for $5f^{12}7s7p\ ^5G_5^0$ transition of ^{255}Fm , taken from Ref. [44].

3.1.2 Indirect production of $^{248,249,250}\text{Fm}$ for RADRIS

In the RADRIS beamtime in 2020 at the GSI in Darmstadt, laser spectroscopy was performed on the previously assigned level $5f^{12}7s7p\ ^5G_5^0$ of ^{248}Fm , ^{249}Fm , and ^{250}Fm . The transition was known from previous studies of ^{255}Fm (see Sec. 3.1.1). The laser was scanned around this values to determine the isotope shift. While the neutron rich fermium isotopes ^{255}Fm and ^{257}Fm can be produced by reactor breeding, neutron deficient fermium isotopes are typically produced by fusion evaporation reactions (see Sec. 2.4.2). To increase the production rate of the isotopes $^{248,249,250}\text{Fm}$ at SHIP, different indirect production schemes were applied. Different Pb isotope target foils react in a two neutron evaporation reaction with a $^{48}\text{Ca}^{10+}$ beam to No, which decays by α decay to the respective fermium daughters according to:



The cross section for the production of $^{252,253,254}\text{No}$ in the above-mentioned fusion reactions is about $0.5\ \mu\text{b}$, $1.3\ \mu\text{b}$ and $2\ \mu\text{b}$, respectively [126]. The evaporation residue is guided by SHIP (see Sec. 2.4.3) to the RADRIS gas cell, where it is thermalized in 90 mbar argon gas of high purity ($\geq 99.9999\%$). This avoids efficiency losses due to neutralization from charge transfer and molecule formation with contaminants. The potentials of the filament, the cross-piece, the opposing electrode and the first guiding electrode have two possible configurations to switch between “collection mode”, to accumulate the thermalized fusion evaporation residues onto the filament and the “detection mode” guiding to the PIPS detector [168], [142]. In this latter way, the respective nobelium mother isotope is collected onto the filament and decays via α decay to the corresponding fermium daughter with a half-life of 2.44 s (^{252}No), 1.62 min (^{253}No) and 51.2 s (^{254}No). The α -recoiling fermium ions are thermalized in the surrounding buffer gas and recollected on the filament. The voltages of the respective modes are tabulated in Tab. 3.3, a technical drawing of the RADRIS setup is given in Fig. 3.3..

During the accumulation on the filament, the beam is on, the potential settings

3 Fermium laser spectroscopy

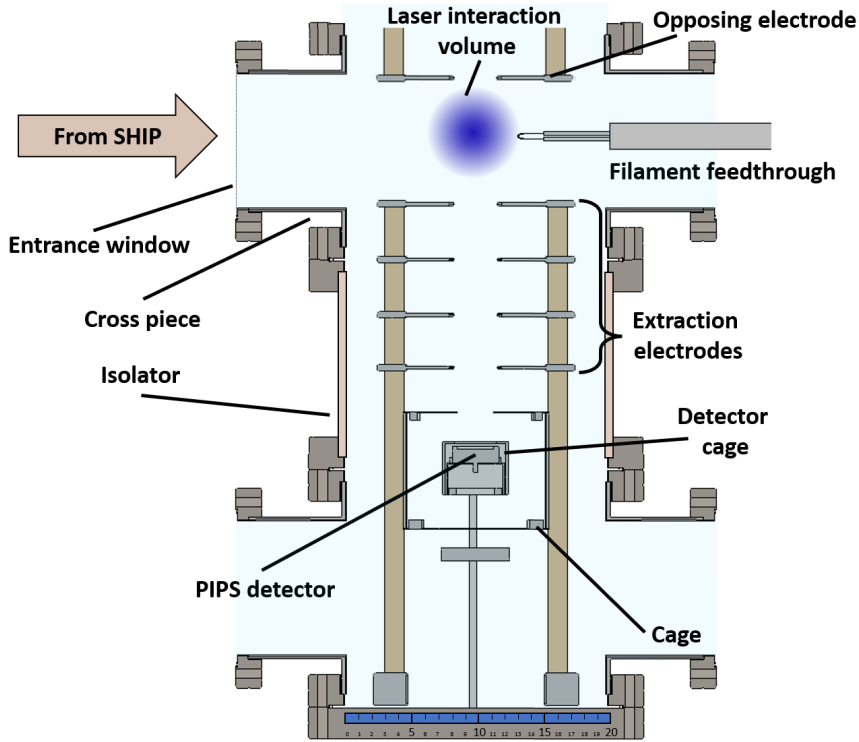


Figure 3.3: Technical drawing of the RADRIS cell. The filament, the cross-piece, the opposing electrode and the first guiding electrode can be varied between collection and a guiding mode, see Tab. 3.3.

Configuration	Collection mode [V]	Detection mode [V]
Filament	300	1015
Cross piece	746	1025
Opposing electrode	746	1025
Electrode 1	749	1000
Electrode 2	800	800
Electrode 3	605	605
Electrode 4	580	580
Cage	245	245
Detector cage	0	0

Table 3.3: RADRIS electrode settings for collection mode and detection mode. Values taken from Ref. [142]

are in collection mode, the lasers are blocked and the resistive heating of the filament is off. The filament used for fermium spectroscopy consists of a ~ 3 cm long 1×0.025 mm² hafnium foil strip, which provides a low work function and low

3 Fermium laser spectroscopy

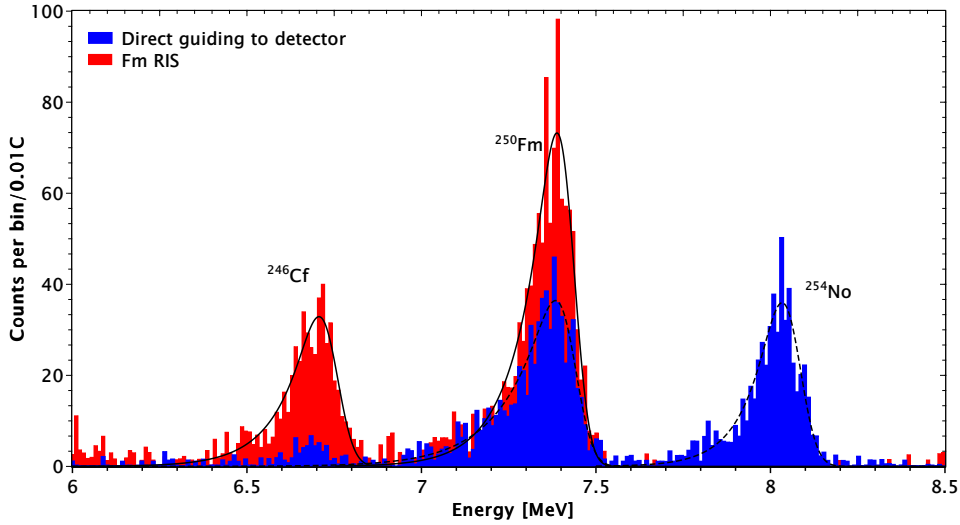


Figure 3.4: α spectra for ^{250}Fm production on the PIPS detector, generated from summing up all performed scans (about 40 h). In a direct guiding scenario, ^{254}No and ^{250}Fm are detected (in blue). For resonance ionization spectroscopy of ^{250}Fm , α peaks of ^{250}Fm and ^{246}Cf are obtained (in red). The α spectra are fitted with the convolution of a Gaussian and the weighted sum of two left-sided exponentials, see Sec. 7.1, shown in solid and dashed lines for direct guiding and fermium spectroscopy, respectively.

desorption temperatures resulting in a negligible amount of surface ions [143]. The collection time on the filament to breed $^{248,249,250}\text{Fm}$ depends on the half-life of the respective fermium isotope, which is higher than the breeding half-life of the nobelium mother. The optimized accumulation time T_a is therefore set to 30 s, 120 s and 30 min for the different fermium isotopes, respectively. After the collection, a number $\#N$ of ionization and guiding cycles to the detector are performed. For each of the cycles with a duration of T_i the atoms are evaporated by a 0.3 s long heatpulse, which heats the filament to a temperature of about 1450 °C. As mentioned in Sec. 2.5.5, the desorption temperature is element dependent, such that, e.g., for nobelium it is set to 1350 K \approx 1620 °C [15]. The potentials of the components involved in the accumulation are in guiding mode, the beam is off and the laser shutters are open. Thus, possible background arising from transfer product passing through SHIP should be suppressed and only RIS ions should be guided to the PIPS detector. After the detection mode cycles, a waiting time T_w ends each RADRIS cycle, before the accumulation for the next wavenumber starts. In Fig. 3.4, the α decay spectra for the reaction $^{208}\text{Pb}(^{48}\text{Ca}, 2n)^{254}\text{No} \xrightarrow{\alpha} ^{250}\text{Fm}$ is given.

For a direct guiding of the fusion evaporation reaction products to the detector, ^{254}No and ^{250}Fm are observed. In a fermium RIS setup, ^{250}Fm and its α decay daughter ^{246}Cf are detected. A schematic picture of the RADRIS cycle is given in Fig. 3.5.

3 Fermium laser spectroscopy

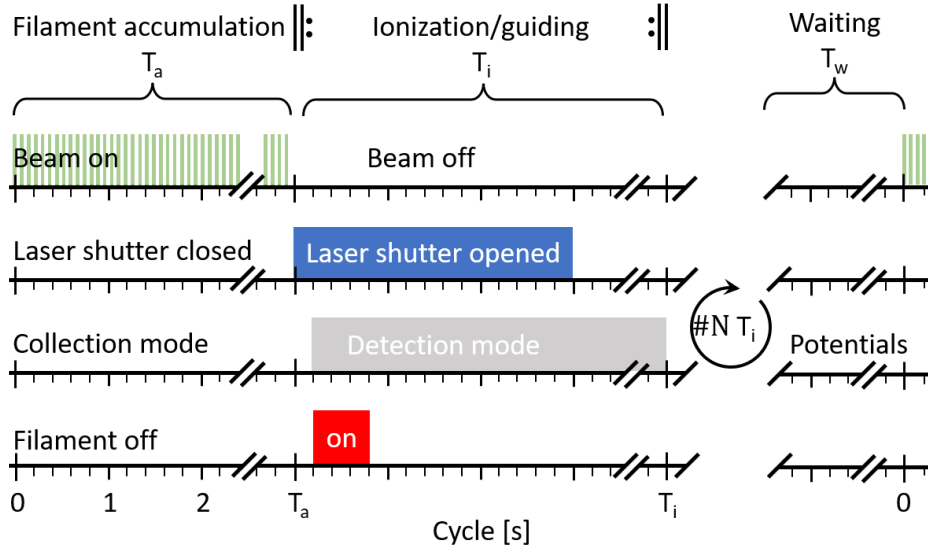


Figure 3.5: Schematic picture of the RADRIS cycle for RIS on fermium. For the “collection” mode, the accumulation time T_a before the ionization and guiding is set to 30 s for ^{248}Fm , 120 s for ^{249}Fm and 30 min for ^{250}Fm . For the “detection mode”, the RIS cycle is repeated several times with an individual duration of T_i , whereby the number of repetitions $\#N$ varies between the different isotopes. Before the new cycle, a waiting period of T_w is included. The total time of the “detection mode” $T_{\text{tot}} = \#N T_i + T_w$ is set to 25 min, 30 min and 2.5 h for ^{248}Fm , ^{249}Fm and ^{250}Fm , respectively. Picture adapted from Ref. [168].

By varying the wavenumber of the first step of the laser ionization scheme, a scan is performed across the transition. The wavenumber is varied in a random manner to avoid systematic errors. The total measurement time T_{tot} for one point takes at least $5 t_{1/2}$. The first fermium isotope measured on-line by laser spectroscopy was ^{250}Fm with a half-life of 30 min. The measurement time per data point was set to 2.5 h. For ^{248}Fm with a half-life of 34.5 s, 25 min per data point were used. For ^{249}Fm , the time to collect one data point was set to 30 min for a half-life of 2.6 min. The second step for the laser ionization is provided by an eximer laser at 351 nm (see Sec. 3.1.3), such that the ionization potential at 6.39 ± 0.13 eV can be exceeded [169].

To ensure the proper operation of SHIP and an stable beam delivery, the fusion evaporation residue production is checked regularly by a direct guiding to the PIPS detector. Moreover, the direct collection of the fusion products on the detector enables to set a suitable α -energy gate for the scan of the resonance. The α -decay branching ratio is 55% for ^{252}No , 66.7% for ^{253}No and 90% for ^{254}No , such that the effective fermium production cross section corresponds to 275 nb, 867.1 nb and $1.8 \mu\text{b}$ for the different isotopes, respectively, if all fermium daughters are collected.

3.1.3 Laser system of the RADRIS setup

The laser hut at GSI houses three excimer lasers (Lambda Physik, LPX240i, LPX210i and LPX220) and three tunable dye lasers (Lambda Physik, FL series, bandwidth 0.2 cm^{-1}), two of each were used for spectroscopy of fermium. The entire laser system is pulsed at a repetition rate of 100 Hz, whereby the pulse lengths of the excimer lasers are about 18 ns. The scanning of the resonance was performed with a single dye laser, which was pumped by the LPX240i excimer, while the non-resonant second step was provided by the excimer laser LPX220. The synchronization of the dye lasers with the excimer laser is ensured by synchronization units (Lambda Physik, LPA 97), whereby a pulse generator (Berkeley Nucleonics Corporation, Model 555) applies the required and synchronized triggers to the synchronization units. The use of dye lasers hereby enables to reach a broad range of wavelengths that can be covered according to the choice of dye.

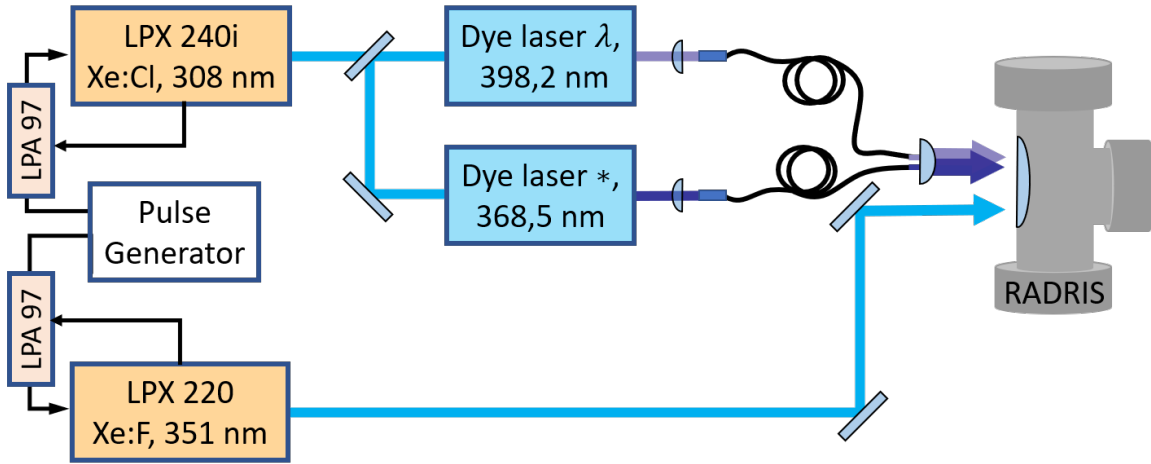


Figure 3.6: Schematic picture of the RADRIS laser system. A pulse generator ensures a proper timing of the first and second ionizing step. LPX240i pumps two dye lasers, which are guided via fiber to cell, while LPX220 is guided directly by mirrors to RADRIS.

LPX240i is a Xe:Cl gas operated excimer laser, which provides an emission wavelength of 308 nm with a power of 50 mJ per pulse. It is used to pump two dye lasers at the same time, so that 20-25 mJ can be coupled into each of them. The dye lasers are operated with Excalite-398 dye solved in p-dioxane (0,1 g/l) to provide laser light between 384 – 420 nm [170] for spectroscopy at up to $500\ \mu\text{J}$ energy per pulse. To be able to scan across the resonance in sufficiently narrow steps, a Fabry-Perot etalon is implemented in the first dye laser to reduce the bandwidth from 0.2 cm^{-1} to 0.05 cm^{-1} for narrowband scans. Another dye laser with a bandwidth of 0.2 cm^{-1} is set to $27137,09\text{ cm}^{-1}$ to match an auto ionizing state of fermium found in 2019 (see Sec. 3.2.2). The laser light from the dye lasers with a power of $\leq 500\ \mu\text{J}$ is coupled to UV grade optical multimode fibers

and guided to the buffer gas stopping cell. At the filament position, a 3 cm² large spot is formed by a lens system for spectroscopy at laser pulse energies $\leq 150\mu\text{J}$. The second step provided by the LPX220 excimer laser is transported by high reflective mirrors with a transmission efficiency of about 45% to the RADRIS cell. To ensure a decent overlap with the first step, the beam is expanded by a cylindrical telescope to a spot of 25×35 mm² and back reflected after passing through the gas cell by a rectangular high reflective mirror onto the same beam path, such that the laser light passes the cell four times [142].

The non-resonant second step is provided by a Xe:F operated excimer laser LPX220, which provides a wavelength of about 351 nm. After transportation by a mirror system to the RADRIS cell, it delivers a laser power of at least 30 mJ per pulse. Overall, the spectral resolution of the RADRIS method is limited by pressure broadening described in Sec. 2.5.3 to about 500 MHz. The applied wavelengths are monitored by a wavemeter (High Finesse, WS7/30). A more detailed description of the laser system is given in Ref. [127].

3.2 Results for fermium laser spectroscopy

3.2.1 Isotope shift measurements of ^{248,249,250}Fm

For nuclei with even proton and neutron numbers and zero spin, the isotope shift $\delta\bar{\nu}^{A,A'} = \bar{\nu}^{A'} - \bar{\nu}^A$ of the studied transition provides direct information on the nuclear size and possible deformation. Thus, only odd fermium isotopes ($Z=100$) exhibit a hyperfine structure, from which magnetic and electric hyperfine constants can be derived. The transition from the $5f^{12}7^2\ ^3H_6^e$ ground state to the excited state $5f^{12}7s7p\ ^5G_5^0$ was studied for the isotopes ^{248,249,250}Fm to investigate the isotope shift.

For each measurement point on a chosen wavenumber, the α events collected on the PIPS detector in the set α -energy gate were counted. A normalization with respect to the beam current integral is needed, since the formation rate of fusion products is proportional to this quantity and the primary beam intensity fluctuates during on-line measurements. Therefore, the accumulated charge integral registered at the beam dump is taken into account to normalize the number of registered events on the PIPS detector to 0.01 C, which corresponds to $6.24 \cdot 10^{16}$ ⁴⁸Ca projectiles per second.

The even-mass isotope ²⁵⁰Fm with a half-life of $t_{1/2} = 30$ min was the first isotope, on which spectroscopy was performed. The laser pulse energy amounted to 150 μJ . To estimate the influence of the laser power on the line shape, the photon flux density can be calculated by:

$$\Phi_1 = \frac{n_1}{A_l} = \frac{E_b}{h\bar{\nu}_1} \frac{1}{A_l} . \quad (3.2)$$

The area of the laser beam is $A_l = 3.0(5)$ cm² (see Sec. 3.1.3) and the photon energy at $\bar{\nu}_1 = 25112$ cm⁻¹ amounts to $h\bar{\nu}_1 = 5.0 \cdot 10^{-19}$ J. With the laser pulse

3 Fermium laser spectroscopy

energy of $E_b = 150 \mu\text{J}$, the photon flux density results to $1.0(4) \cdot 10^{14}$ photons/cm². This can be compared to saturation behaviour studies in Ref. [136]. Originally, these studies were conducted to assess Einstein coefficients A_{ki} of the $5f^{12}7s7p^5I_6^0$ and $5G_5^0$ -to-ground-state transitions of ^{255}Fm . Einstein coefficients on the order of $3.6(7) \cdot 10^6$ /s and $3.6(6) \cdot 10^6$ /s were obtained for these transitions, respectively, which are in good agreement with predictions from Multi-Configuration Dirac Fock (MCDF) calculations [136]. To avoid a saturation broadening, different model assumptions generally show that E_b should be below $100 \mu\text{J}$ per pulse, which corresponds to $1.3(7) \cdot 10^{14}$ photons/cm² in the geometry such as in Ref. [136]. Its centroid extracted with a voigt fit and located at $\bar{\nu}_{250} = 25112.80 \text{ cm}^{-1}$. The uncertainty of the centroid position is assumed to be 0.04 cm^{-1} (see discussion in Sec. 3.2.3).

To avoid power broadening for ^{248}Fm ($t_{1/2} = 34.5 \text{ s}$), the spectroscopy was performed with pulse energies $< 70 \mu\text{J}$, which results in a photon flux density of $5(3) \cdot 10^{13}$ photons/cm². The centroid is located at $\bar{\nu}_{248} = 25113.12 \pm 0.04 \text{ cm}^{-1}$. ^{249}Fm ($t_{1/2} = 2.6 \text{ min}$) is an odd- N isotope with 149 neutrons, such that hyperfine splitting occurs. The study of excited states in ^{249}Fm confirmed a spin parity of $I = 7/2^+$ for the ground state of ^{249}Fm [171]. Due to high angular momenta of $J = 6$ in the atomic ground state and $J = 5$ in the excited state of ^{249}Fm , 21 hyperfine levels are expected in the resonance. In the RADRIS beamtime 2020, a narrowband scan was performed, which did not resolve the variety of expected levels and suffered from low count rate. Therefore, the measurement was repeated in 2021, showing poor agreement to the data taken in 2020. Both data sets suffer from the low number of detected events. Since the time required per data point amounts to 1 h, the laser power varies during the measurement resulting in an additional uncertainty. The two different narrowband scans are depicted in Fig. 3.7.

Since the hyperfine structure could not be resolved and the remaining beamtime was limited, a broadband scan was performed instead. The centroid of the ^{249}Fm broadband scan is located at $\bar{\nu}_{249} = 25113.0 \pm 0.1 \text{ cm}^{-1}$. Measured spectra for the individual isotopes are depicted in Fig. 3.8, together with the best fit to the data. Since the pressure broadening effect on the line profile follows Lorentz profile, while the laser line profile can be assumed a Gaussian profile, the overall line shape of the resonances results in a Voigt profile. Therefore, the resonances of the even fermium isotopes ^{248}Fm and ^{250}Fm were fitted with a Voigt profile. Since the laser bandwidth of the broadband scan for the odd- A isotope ^{249}Fm dominates the pressure broadening, a Gaussian fit is used to extract the weighted center of gravity of the hyperfine structure, which could not be resolved.

The centroid of ^{250}Fm with $N=150$ neutrons can be taken as a reference point for the isotope shift evaluation. In Tab. 3.4, the centroids and the respective isotope shifts of $^{248,249,250}\text{Fm}$ are tabulated.

3 Fermium laser spectroscopy

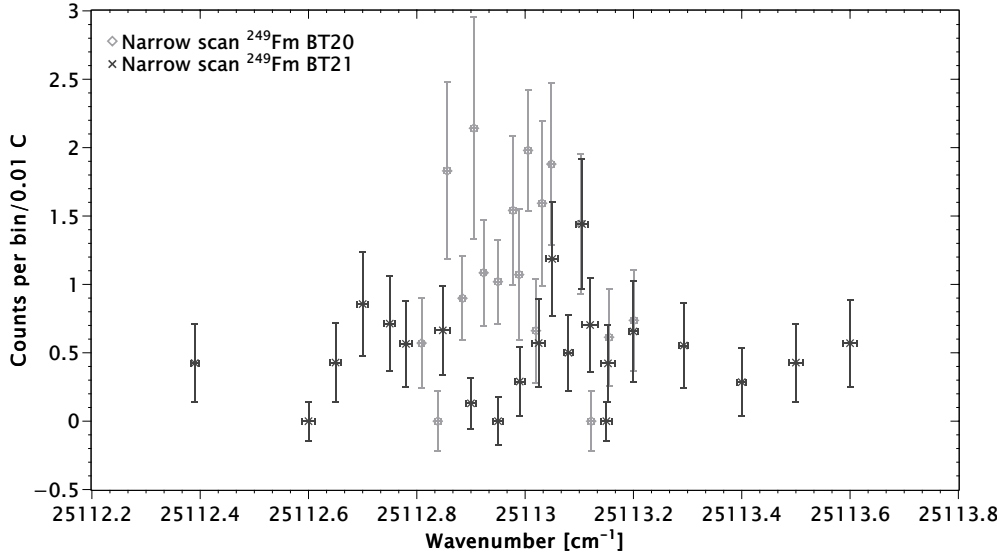


Figure 3.7: Two narrowband scans over $5f^{12}7s7p\ ^5G_5^0$ atomic state of ^{249}Fm . The two measurements are not consistent and the hyperfine structure is not resolved.

Isotope	Centroid [cm^{-1}]	$\delta\bar{\nu}^{250,A'}$ [cm^{-1}]	$\delta\bar{\nu}^{250,A'}$ [GHz]
$^{248}_{100}\text{Fm}$	25113.12 ± 0.04	0.32 ± 0.02	9.6 ± 0.7
$^{249}_{100}\text{Fm}$	25113.00 ± 0.1	0.20 ± 0.09	5.8 ± 2.5
$^{250}_{100}\text{Fm}$	25112.80 ± 0.04	0.00 ± 0.02	0.0 ± 0.7

Table 3.4: Centroids of the fermium isotopes $^{248,249,250}\text{Fm}$ and isotope shift with respect to ^{250}Fm . Isotope shift uncertainties do not include systematic errors.

3.2.2 Isotope shift values for ^{255}Fm and ^{257}Fm

Apart from the on-line investigated isotopes $^{248,249,250}\text{Fm}$, results for previously investigated fermium isotopes from off-line samples can be taken into account. Isotope shift values for neutron-rich isotopes enable to extract the change in mean-square charge radii across the $N=152$ shell gap. As stated in Sec. 3.1.1, the centroid of the spectrum of ^{255}Fm is known from prior studies from Sewtz et al. [172] and amounts to $\bar{\nu}_{255} = 25111.80 \pm 0.2 \text{ cm}^{-1}$. Furthermore, off-line spectroscopy on ^{257}Fm was performed in 2019 during a RIS measurement campaign on einsteinium at RISIKO at JGU [161]. The used sample was produced in the HFIR reactor at ORNL [173]. Apart from $^{253,254,255}\text{Es}$, the sample contained isotopes from plutonium, americium, curium, berkelium, and californium as byproducts from the breeding process [160] as well as minor amounts of $^{254-257}\text{Fm}$. After chemical separation at the TRIGA site of the chemistry department in Mainz, the sample size contained $\leq 5 \times 10^7$ atoms ^{257}Fm ($t_{1/2} = 100.5 \text{ d}$). This allowed both broad and narrowband scans on ^{257}Fm .

3 Fermium laser spectroscopy

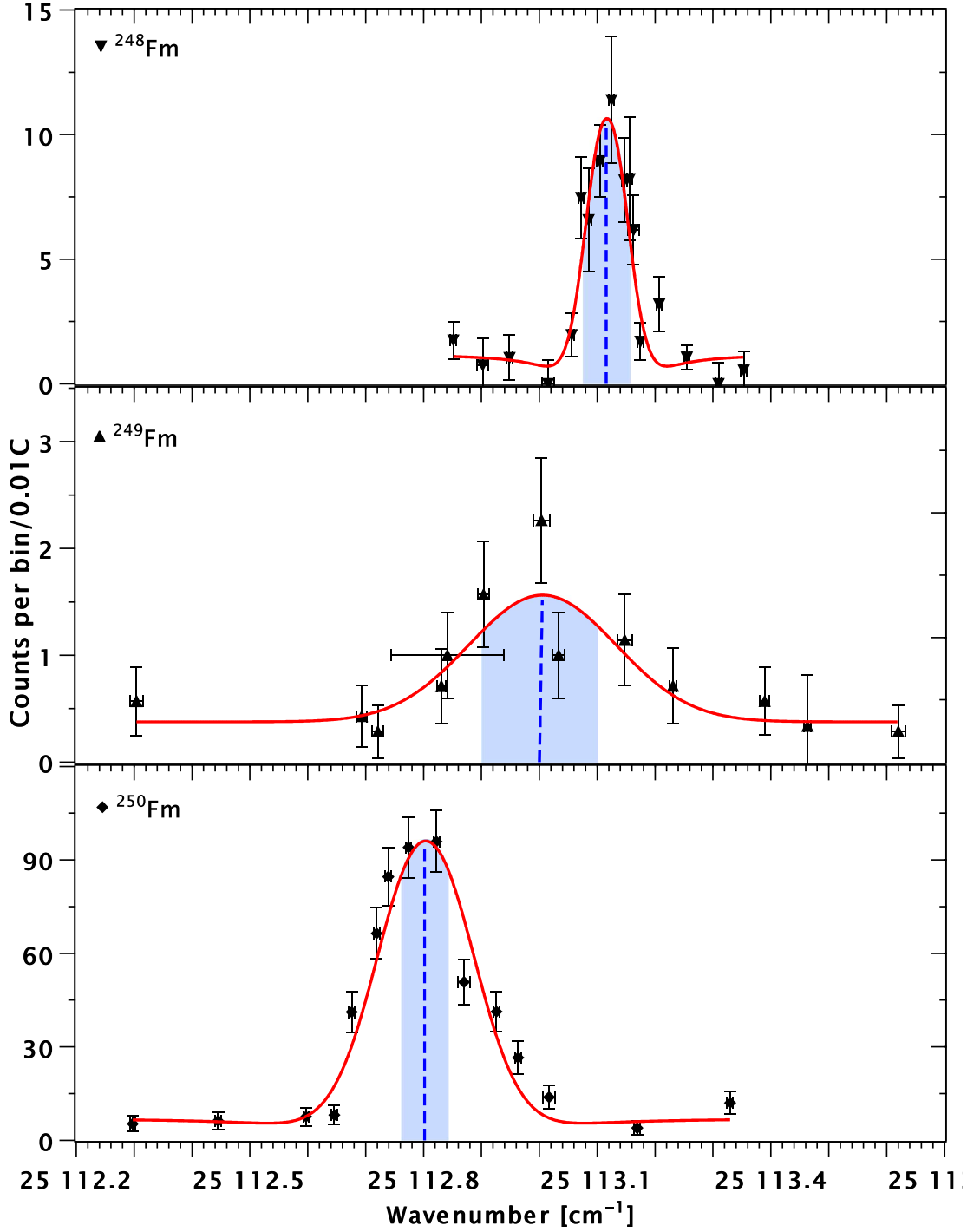


Figure 3.8: Scan over $5f^{12}7s7p\ 5G_5^0$ state of $^{248,249,250}\text{Fm}$. The centroids were located at $25113.12 \pm 0.04\ \text{cm}^{-1}$, $25113.12 \pm 0.1\ \text{cm}^{-1}$ and $25112.80 \pm 0.04\ \text{cm}^{-1}$, respectively. The respective stated uncertainty is shown in light blue around the centroid. Laser pulse energies for the different isotopes were $< 70\ \mu\text{J}$, $100\ \mu\text{J}$ and $150\ \mu\text{J}$, respectively. The data of the even isotopes are fitted with Voigt profiles, ^{249}Fm was fitted with a Gaussian (for details see text).

3 Fermium laser spectroscopy

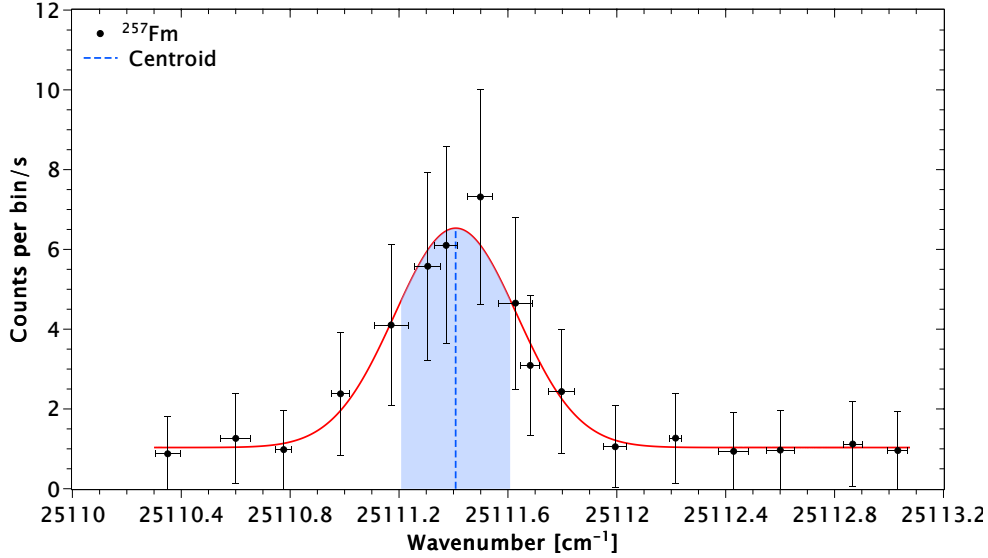


Figure 3.9: Broadband scan over $5f^{12}7s7p\ ^5G_5^0$ state of ^{257}Fm . The hyperfine structure is unresolved. The centroid is located at $25111.41 \pm 0.2\ \text{cm}^{-1}$. The stated uncertainty is shown in light blue around the centroid. The data were fitted with a Gaussian, shown by the red line.

For the narrowband scan, two Fabry-Perot etalons were used, nonetheless the hyperfine structure could not be resolved due to Doppler broadening of about 2.5 GHz in the hot cavity of the RISIKO setup [174]. In this work, the broadband scan is presented, while the narrowband scan will be covered by J. Warbinek in the framework of her PhD thesis together with a narrowband scan of ^{255}Fm [175]. In Fig. 3.9, the broadband scan of ^{257}Fm is given. The respective centroid is located at $\bar{\nu}_{257} = 25111.41\ \text{cm}^{-1}$. The uncertainty is set conservatively to $\pm 0.2\ \text{cm}^{-1}$, the same as for ^{255}Fm . The centroids and isotope shifts of ^{255}Fm and ^{257}Fm respective to ^{250}Fm are given in Tab. 3.5.

Isotope	Centroid [cm^{-1}]	$\delta\bar{\nu}^{250,A'}$ [cm^{-1}]	$\delta\bar{\nu}^{250,A'}$ [GHz]
$^{255}_{100}\text{Fm}$	25111.80 ± 0.2	-1.00 ± 0.2	29.8 ± 6.0
$^{257}_{100}\text{Fm}$	25111.41 ± 0.2	-1.39 ± 0.2	41.6 ± 6.0

Table 3.5: Centroids of the fermium isotopes 255 and ^{257}Fm and isotope shift with respect to ^{250}Fm . Laser pulse energies for the isotopes are 50 mJ and 10 mJ, respectively.

3.2.3 Uncertainties on the centroid position

Uncertainties in the determination of the centroid wavenumbers of the different isotopes were mainly caused by systematic uncertainties. Since the spectroscopy was performed in the gas-filled RADRIS cell, the pressure broadening (see Sec. 2.5.3) is an uncertainty component that effects the width of the overall line shape of the resonances. According to Ref. [176], the pressure shift at RADRIS is about 10.8 MHz/mbar, such that for 90 mbar is on the order of ~ 1 GHz. Due to spectroscopy at room temperature, the Doppler broadening of the on-line investigated isotopes amounts to about 250-300 MHz [127]. The centroid position can be extracted irrespective of the respective resonance width, whereby the uncertainty of the centroid position increases.

For ^{249}Fm , the used Gauß fit is only used to extract the weighted center of gravity of the hyperfine structure, not to derive hyperfine structure parameters. To account for this, 25% of the FWHM is added to the centroid position error. For all isotopes, the step size of the resonance scan was 0.03 cm^{-1} , such that the measurement granularity is $\pm 0.015\text{ cm}^{-1}$ around each data point. The pressure shift can be assumed to be 500 MHz to give a conservative estimation on this systematical error. For extracting the uncertainty of the isotope shift $\delta\bar{\nu}^{250,A'}$, the pressure shift can be neglected, since it cancels out in relative terms of the same measurement conditions. Power broadening is present only for the ^{250}Fm spectrum with laser pulse energies of $150\ \mu\text{J}$ (see Sec. 3.2.1). Apart from the laser power, all settings for ^{250}Fm and ^{248}Fm were the same, such that the increased FWHM of ^{250}Fm , which is on the order of $\text{FWHM}_{250} \approx 2.4 \times \text{FWHM}_{248}$ can be solely attributed to the power broadening. However, the uncertainty caused by the power broadening is smaller than the uncertainty arising from the laser bandwidth. For broadband scans, the laser bandwidth is 0.2 cm^{-1} (6 GHz), which can be reduced to 0.05 cm^{-1} (1.5 GHz) when an etalon is implemented for narrow-band scans. 20% of the laser bandwidth are taken into account to contribute to the wavenumber measurement uncertainty. It is known that the used wavemeter drifted about 400 MHz during the whole measurement campaign, which is also considered in the wavenumber measurement uncertainty. Compared to this effect, the laser frequency stability during the ionization is assumed to have a minor contribution to the wavenumber uncertainty, even though the respective measurement time per data point of 25 min, 30 min and 2.5 h for $^{248,249,250}\text{Fm}$ allows a drift in the wavenumber, measured by the wavemeter. The different uncertainties are tabulated in Tab. 3.6. The total uncertainty is given by the root of the sum of squared statistical errors plus the systematic error.

Gate setting and charge collection uncertainties lead to only very minor changes in the centroid position, as indicated in the error bars in Fig. 3.8, which amount to less than 10% of the stated uncertainty. Further uncertainties arise from the filament heating process. Due to the heating, the filament bends in the RADRIS cell, such that the overlap with the pulsed ionizing laser beams may not be optimal. The laser power itself is hereby unstable, since the dye faded over time and

3 Fermium laser spectroscopy

Uncertainty [cm^{-1}]	^{248}Fm	^{249}Fm	^{250}Fm
Wavemeter measurement	(0.0167)	(0.042)	(0.0167)
± 0.5 Granularity	(0.015)	(0.015)	(0.015)
Model uncertainty 25%FWHM		(0.075)	
Pressure shift	[0.0167]	[0.0167]	[0.0167]
Total uncertainty	0.04	0.1	0.04

Table 3.6: Uncertainties of the $5f^{12}7s7p$ state resonance for $^{248-250}\text{Fm}$. The statistical errors are given in parentheses ($\text{}$), the systematic errors in square brackets [$\text{}$]. For the isotope shift uncertainty, the systematic error can be neglected compared to the typical statistical uncertainty of a few GHz.

needed to be replaced regularly. Moreover, the heating of the filament leads to an uneven temperature distribution with the hottest point at the tip of the filament. Any misalignment of the pyrometer results in a higher desorption temperature than intended, which is even more prone to error due to the bending of the filament. A variation in the desorption temperature contributes to a fluctuation in evaporated isotopes. Moreover, the resulting atom cloud size is effected by the desorption temperature, however, this effect is presumably small. Since the pyrometer position was routinely checked, this effect is indistinguishable from a fluctuation in the production of No-mother isotopes, which is accounted for in the y-error bars in Fig. 3.8.

3.2.4 Uncertainties on $\delta\langle r^2 \rangle$

The uncertainties of the centroid propagates to the uncertainties on $\delta\langle r^2 \rangle$. Moreover, the uncertainty of the atomic coupling factors K_{MS} and F_{FS} have to be considered. Since these uncertainties alter with the distance to the reference isotope and depend on the factor $\frac{m^{A'} - m^A}{m^{A'} m^A}$, which changes its size and sign according to the chosen reference isotope, they contribute to the systematic uncertainties. For the calculation of $\delta\langle r^2 \rangle$, only the field shift term F_{FS} of the isotope shift from Eq. 2.14 is taken into account, while the mass shift K_{MS} is neglected. As the mass shift is composed from the normal and specific mass shift (see Sec. 2.1.5), the uncertainty estimation of K_{MS} can be divided in these two parts, too. The normal mass shift due to the reduced mass correction is given for a given transition by $K_{NMS} = \bar{\nu}[\text{cm}^{-1}]/1836.1 \cdot \text{u}$, which amounts to $K_{NMS} = 13.7\text{cm}^{-1} \cdot \text{u} = 410 \text{ GHz} \cdot \text{u}$ for $\bar{\nu} = 25112\text{cm}^{-1}$ [34]. u is hereby the atomic mass unit. Non-relativistic Hartree-Fock calculations reveal, that the specific mass shift K_{SMS} is on the order of K_{NMS} for s - p and s^2 - sp transitions. For transitions which involve d or f electrons, K_{SMS} can be on the order of

3 Fermium laser spectroscopy

$10 \times K_{NMS}$ [34]. To give a conservative estimate, the uncertainty of K_{MS} is therefore assumed to be about $\Delta K_{MS} = 5 \times K_{NMS} \approx 200 \text{ GHz} \cdot \text{u}$.

The uncertainty of the field shift constant F_{FS} originates from the uncertainty in the atomic calculations, which amounts to $\Delta F \approx 10\%F$. The systematic error is therefore calculated by

$$\Delta\delta\langle r \rangle_{+10\% \text{ sys}}^{A,A'} = \frac{\delta\bar{\nu}}{1.1 \cdot F} \quad \text{or} \quad \Delta\delta\langle r \rangle_{-10\% \text{ sys}}^{A,A'} = \frac{\delta\bar{\nu}}{0.9 \cdot F} \quad , \quad (3.3)$$

which results in a slightly asymmetric error band. Another possibility to obtain the systematic error is given by the equation

$$\delta\langle r \rangle_{\text{sys}}^{A,A'} = \sqrt{\left[\frac{\Delta F \delta\bar{\nu}}{F^2} \right]^2 + \left[\frac{\Delta K_{MS} (m^{A'} - m^A)}{F m^{A'} m^A} \right]^2 + \left[\frac{\Delta F K_{MS} (m^{A'} - m^A)}{F^2 m^{A'} m^A} \right]^2} \quad , \quad (3.4)$$

whereby the last term can be neglected, since only ΔK_{MS} is included while K_{MS} is set to zero. Following this procedure, a symmetric systematic error is obtained, which is equal to the smaller error band of $\Delta\delta\langle r \rangle_{\pm 10\% \text{ sys}}^{A,A'}$ from Eq. 3.3 for the treated isotopes. The respective systematic uncertainties are given in Tab. 3.8. Following the approach in Ref. [44], the isotope shift is directly dependent on the deformation and not only indirectly by the respective increase in volume, which affects the deformation. The expected deformation effect amounts hereby to about -0.003 fm^2 , which is considerably smaller than the uncertainties arising from the centroid position and can thus be neglected.

3.2.5 Trend in mean-square charge radii $\delta\langle r^2 \rangle$ of ${}^{248,249,250}\text{Fm}$ and ${}^{255,257}\text{Fm}$

From the isotope shift, the changes in the root-mean-square charge radii (mscr) $\delta\langle r^2 \rangle$ can be extracted according to Sec. 2.1.5. Studying $\delta\langle r^2 \rangle$ allows observing features of isotopic and isotonic general trends, may unveil non-traditional magic numbers and may disclose the influence of deformations [17]. However, atomic mass shift and field shift parameters are needed to compute $\delta\langle r^2 \rangle$ from the isotope shift $\delta\bar{\nu}^{A,A'}$. Mass shift and field shift parameters are not experimentally available in fermium, since no stable reference isotopes exist. A King-Plot analysis is therefore impossible. As an alternative, K_{MS} and F_{FS} can be derived from theory calculations. This approach has also been successfully used to extract the mscr for nobelium isotopes [126].

Since the contribution of the mass shift to the isotope shift gets negligible for high Z [177], the mass shift part of Eq. 2.14 can be neglected for fermium ($Z=100$). Therefore, the isotope shift can be approximated by

$$\delta\bar{\nu}^{A,A'} = F\delta\langle r^2 \rangle^{A'A} \quad . \quad (3.5)$$

3 Fermium laser spectroscopy

The uncertainty arising from this approximation is discussed in Sec. 3.2.4.

Recent calculations using the Configuration Interaction with Perturbation Theory (CIPT) method were performed in Ref. [44] to model the electronic structure of ^{255}Fm . This new approach provided a measure on the field shift constant F_{FS} and the nuclear quadrupole deformation parameter β and suggested an alternative form of Eq. 3.5:

$$\delta\bar{\nu}^{A,A'} = F\delta\langle r^2 \rangle^{A'A} + d\Delta\beta \quad . \quad (3.6)$$

d is hereby an isotope-dependent constant to scale the change in deformation between neighbouring isotopes $\Delta\beta$. In Tab. 3.7, the isotope shift parameters derived in Ref. [44] for the $5f^{12}7s7p\ ^5G_5^0$ atomic state of ^{255}Fm are listed.

β	$\Delta\beta$	F [$\text{cm}^{-1}/\text{fm}^2$]	d [cm^{-1}]
≈ 0.3	≈ 0.02	-3.14	0.397

Table 3.7: Isotope shift parameters for $5f^{12}7s7p\ ^5G_5^0$ transition of ^{255}Fm , taken from Ref. [44].

To obtain the changes in mscr from the isotope shift $\delta\bar{\nu}^{A,A'}$, Eq. 3.5 and the field shift constant F_{FS} from Tab. 3.7 were used.

In Tab. 3.8, the values and uncertainties for $\delta\langle r^2 \rangle$ of the on-line accessible fermium isotopes $^{248,249,250}\text{Fm}$ and the off-line measured isotopes $^{255,257}\text{Fm}$ are given. The reference isotope for the fermium isotopes is ^{250}Fm .

Isotope	Centroid [cm^{-1}]	$\delta\langle r^2 \rangle^{250,A'}$ [fm^2]	$\Delta\delta\langle r^2 \rangle_{\text{stat}}^{250,A'}$ [fm^2]	$\Delta\delta\langle r^2 \rangle_{\text{sys}}^{250,A'}$ [fm^2]
$^{248}_{100}\text{Fm}$	25113.12 ± 0.04	-0.102	$\pm (0.010)$	$^{+0.0010}_{-0.0012}$
$^{249}_{100}\text{Fm}$	25113.0 ± 0.1	-0.066	$\pm(0.027)$	$^{+0.0007}_{-0.0008}$
$^{250}_{100}\text{Fm}$	25112.8 ± 0.04	0.00		
$^{255}_{100}\text{Fm}$	25111.8 ± 0.2	0.317	$\pm (0.064)$	$^{[-0.0031]}_{[+0.0037]}$
$^{257}_{100}\text{Fm}$	25111.41 ± 0.2	0.442	$\pm (0.064)$	$^{[-0.0043]}_{[+0.0052]}$

Table 3.8: Centroid positions of the fermium isotopes $^{248,249,250}\text{Fm}$ and $^{255,257}\text{Fm}$, from which changes in mean-square charge radii are extracted with respect to ^{250}Fm . Statistical and systematic uncertainties from Sec. 3.2.4 are given in parentheses and square brackets, respectively.

A theoretical approach to describe the trends of charge radii along isotopic sequences is given by the Droplet Model (DM), a refinement of the Liquid Drop Model (LDM) [178]. In contrast to the semi-empirical LDM, a Hamiltonian defined for the DM, which is derived by expanding the volume, surface, and Coulomb

3 Fermium laser spectroscopy

energies in Taylor series around the standard LDM values [50]. Equivalent radii of neutron and proton distributions are obtained by minimizing the macroscopic energy of the system [179]. As a result, neutron rich nuclei tend to build a neutron skin due to surface tension and a slightly larger neutron distribution. Moreover, the repulsive Coulomb force is predicted to lead to a small amount of bulk redistribution [179], resulting in a central depression. To compare the experimental trend in $\delta\langle r^2\rangle^{A'A}$ to the theoretical expectations from the Droplet Model, the Finite Range Droplet Model (FRDM) from Bardichevsky and Tondeur [178] is used, which applies for spherical nuclei and gives a measure on $\delta\langle r^2\rangle_{\text{sph}}$. Hereby, the second parametrization is chosen, which demonstrated its power in modeling the behaviour of $\delta\langle r^2\rangle$ of even neutron deficient $_{84}\text{Po}$ isotopes between $A = 202 - 210$ [180]. Since these polonium isotopes are deformed in their ground state, the chosen parametrization can be used for the deformed fermium isotopes. A more detailed description of the chosen parametrization, the used constants and the calculation of the FRDM values is given in Sec. 7.2.

The extracted values of $\delta\langle r^2\rangle$ between the measured fermium isotopes $^{248,249,250}\text{Fm}$ and $^{255,257}\text{Fm}$ are shown in Fig. 3.10. The expected values from the spherical droplet model are included for comparison as the slope of $\delta\langle r^2\rangle_{\text{sph}}$.

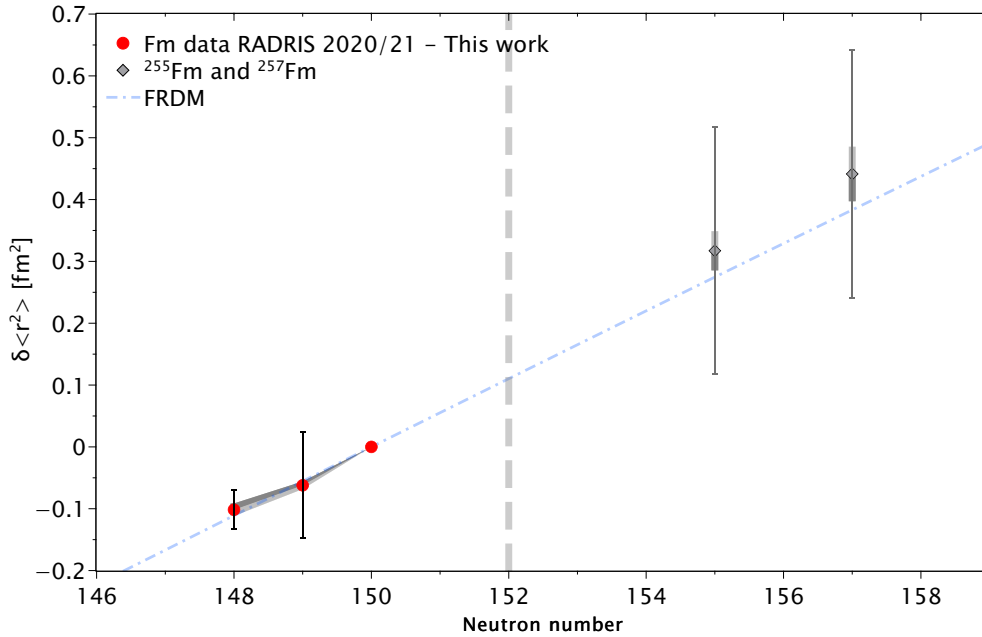


Figure 3.10: Change of msqr $\delta\langle r^2\rangle$ of $^{248,249,250}\text{Fm}$ and $^{255,257}\text{Fm}$. ^{250}Fm is chosen as the reference isotope. The spherical droplet model is given in blue, the 10% error band from the uncertainty in F_{FS} is given in dark and light grey. The $N=152$ shell gap is marked by the grey dashed line.

To account for the deformation of fermium isotopes, a deformation dependent

3 Fermium laser spectroscopy

term can be included in the Droplet Model [181]:

$$\langle r^2 \rangle = \langle r^2 \rangle_{\text{sph}} \left(1 + \frac{5}{4\pi} \langle \beta_2^2 \rangle + \langle \beta_3^2 \rangle + \dots \right) , \quad (3.7)$$

whereby the third and higher order deformation terms can usually be neglected. Therefore, the change in mscr can be modeled by:

$$\delta \langle r^2 \rangle = \delta \langle r^2 \rangle_{\text{sph}} \left(1 + \frac{5}{4\pi} \langle \beta_2^2 \rangle \right) , \quad (3.8)$$

which is both valid for soft and rigid deformation. The investigated fermium isotopes are assumed to feature a constant deformation of $\beta = 0.3$ [44], such that this approximation is applicable.

Apart from the Droplet Model, nuclear Density Functional Theory (DFT) calculations can be used to model the behaviour of the change in $\delta \langle r^2 \rangle$ (see Sec. 2.3.2). In the framework of nobelium spectroscopy, Skyrme-Hartree-Fock (SHF) calculations have been provided for a theoretical assesment of mscr trends [127]. Calculations using the mean-field DFT Skyrme parametrization SV-min were performed for actinide isotopes with an even number of protons and neutrons, including fermium [182]. This parametrization is especially suited to treat heavy and superheavy nuclei in a mean-field approach [183]. To model the change in mscr with beyond-mean-field methods, which include the treatment of pairing correlations and particle-vibration couplings [184], [185], DFT calculations with the Skyrme EDF parametrization UNEDF1 have been provided [182]. UNEDF1 combines self-consistent nuclear mean-field theory with Skyrme functionals and relativistic EDF [185].

In Fig. 3.11, the different theoretical models are drawn for comparison with the experimental data in reference to the spherical FRDM. In the first panel, the change in mscr obtained from isotope shift in experimental fermium data is shown in comparison to the spherical FRDM (blue). Moreover, the change in the slope of the deformed DM ansatz from Eq. 3.8 is included (red). The quadrupole deformation was set to $\beta_2 = 0.3$, as in Ref. [44]. All five fermium isotopes agree with both the spherical and the deformed DM model, whereby this is mainly caused by the large uncertainty of the two neutron rich isotopes. The accuracy of the used FRDM parametrization with experimental data in heavy nuclei is given with 0.2% in Ref. [179]. No firm conclusion to the spherical FRDM can be drawn. The assumption of a quadrupole deformation of about $\beta_2 = 0.3$ is in good accordance with the data, but can also be neglected since the difference between the FRDM and the deformed DM is only minor. Overall, the measured data agree with a constant deformation, as predicted by microscopic-macroscopic [42] and beyond-mean-field EDF calculations [186].

In the second panel of Fig. 3.11, the comparison of the experimental data to the mean-field Skyrme parametrization SV-min is given. Here, all measured

3 Fermium laser spectroscopy

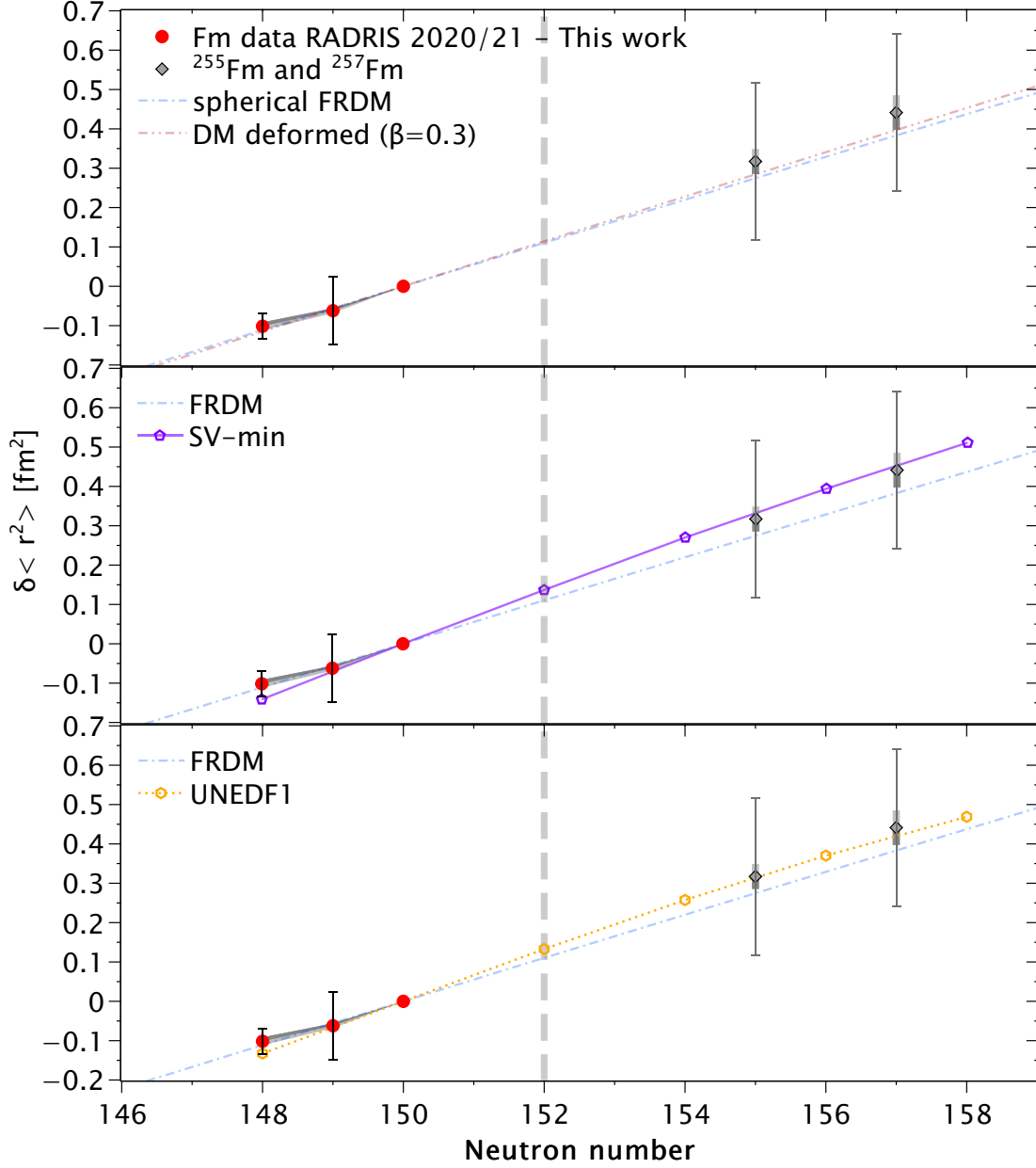


Figure 3.11: Different theoretic models to model the change of mscr $\delta\langle r^2 \rangle$ of $^{248,249,250}\text{Fm}$ and $^{255,257}\text{Fm}$. ^{250}Fm is the reference isotope.

First panel: $\delta\langle r^2 \rangle$ of $^{248,249,250}\text{Fm}$ and $^{255,257}\text{Fm}$ in comparison to FRDM (blue) and the deformed DM for an presumed deformation of $\beta = 0.3$ (red).

Second panel: Comparison of mean-field Skyrme parametrization SV-min calculation with the experimental data. Theoretic values provided from Ref. [182].

Third panel: Comparison of beyond mean-field Skyrme parametrization UNEDF1 calculation with the experimental data. Theoretic values provided from Ref. [182].

The $N = 152$ shell gap is marked in grey dashes. The 10% error band from the uncertainty in F_{FS} is given in dark and light grey. For more details see text.

3 Fermium laser spectroscopy

isotopes agree well with the trend of predicted mscr data. The largest deviation between the experimental value and the SV-min value is located at ^{248}Fm . The difference between the predicted FRDM value and the SV-min value is hereby comparably small ($\approx 0.04 \text{ fm}^2$). It should be noted, that no SV-min values were provided for odd- A isotopes, including ^{255}Fm and ^{257}Fm . To obtain a better comparison between experimental data and modeling values, both the indication of uncertainties and the coverage of odd- N isotopes is required. For an extension of optical spectroscopy to further fermium isotopes (see Sec. 3.4), updated SV-min calculations have been provided covering these issues [187].

In the third panel of Fig. 3.11, the beyond-mean-field parametrization UNEDF1 is given in comparison to the experimental data. Again, the largest deviation between the predicted UNEDF1 value and the experimental data is obtained for ^{248}Fm and amounts to minor $\approx 0.02 \text{ fm}^2$. For the UNEDF1 calculations, neither uncertainties nor predictions for odd- N fermium isotopes are given, which would help to estimate model specific deviations. Moreover, the experimental uncertainties of $^{255,257}\text{Fm}$ should be reduced to be more sensitive to nuclear structure effects.

Overall, the investigated isotopes $^{248,249,250}\text{Fm}$ are in good agreement with the spherical FRDM, the deformed FRDM and two DFT Skyrme calculations (SV-min and UNEDF1). Hereby, the odd isotope ^{249}Fm features an unresolved hyperfine structure splitting. The uncertainty of the centroid position $\delta\bar{\nu}^{249,250}$ affects the uncertainty of $\delta\langle r^2 \rangle^{249,250}$, such that a sound statement on the odd-even staggering can presently not be made. Since the transition $\bar{\nu} = 28185 \pm 1.5 \text{ cm}^{-1}$ reported in Ref. [166] features a larger HFS splitting, spectroscopy of ^{249}Fm at this transition can simplify the extraction of nuclear moments. The uncertainties of the neutron rich isotopes ^{255}Fm and ^{257}Fm are the limiting factor that hampers a better assessment of the theoretical models. A more precise re-measurement will help to gain a better insight on the change in mscr after the deformed shell gap at $N=152$. Moreover, nuclear theory input to the given models to provide model uncertainties and to include more odd- A fermium isotopes, as well as further theoretical approaches would help to model the behaviour of $\delta\langle r^2 \rangle$. An extension to more exotic fermium isotopes on both sides of the $N=152$ shell gap with high resolution spectroscopy is needed to gain a wider perspective of the systematic trends in mscr of fermium isotopes.

In Fig. 3.12, the obtained change in mscr $\delta\langle r^2 \rangle$ of fermium isotopes are shown in comparison to other even Z isotopes in the actinides. The figure is adapted from Ref. [127], [126] and includes theoretical trends of the two different parametrizations of DFT calculations, SV-min (solid) and UNEDF1 (dotted). The measured fermium isotopes, as the nobelium isotopes, agree well with the Droplet Model, such that they are in accordance with an assumed constant deformation. This finding indicates that the evolution of nuclear charge radii is dominated by

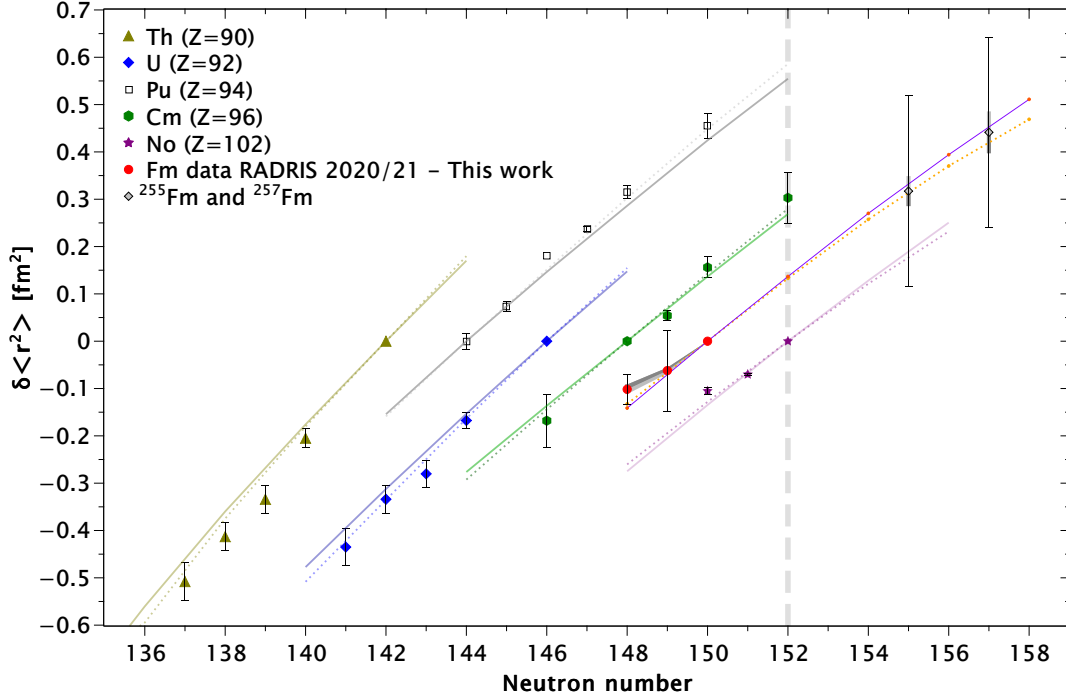


Figure 3.12: $\delta \langle r^2 \rangle$ for $^{248,249,250}\text{Fm}$ and ^{255}Fm and for even Z nuclei in the actinides. Two different parametrizations of DFT calculations, SV-min (solid) and UNEDF1 (dotted), are included for all elements. For fermium, additionally the spherical droplet model (dashed/dotted) and the deformed droplet model (dashed/dotted/dotted) is included. The $N = 152$ shell gap is marked in grey dashes. The 10% error band from the uncertainty in F_{FS} for the investigated fermium isotopes is given in dark and light grey. Adapted from Ref. [127], [126].

bulk properties for heavy nuclei. Single-particle orbitals seem to contribute only slightly to the nuclear charge radii of heavy elements. Deviations of the trend in other actinide isotopes to the Droplet Model may be caused by a change in nuclear deformation throughout the isotope chain of the respective element or the contribution of a central depression of the charge distribution [188].

3.3 Consequences of $^{248-250,255,257}\text{Fm}$ spectroscopy results for approved beamtime

The findings of this thesis motivated an application for further beamtime at GSI. Apart from the level search in ^{255}Lr , isotope shift measurements in ^{251}No and K -isomer studies in ^{254}No , beamtime for the investigation of more on-line accessible fermium isotopes was requested for experiment U321. Hereby, the isotopes ^{245}Fm ($t_{1/2} = 4.2\text{ s}$), ^{246}Fm ($t_{1/2} = 1.54\text{ s}$) and ^{254}Fm ($t_{1/2} = 3.2\text{ h}$) were foreseen for spectroscopic investigation. ^{245}Fm and ^{246}Fm were produced in the reaction

3 Fermium laser spectroscopy

$^{208}\text{Pb}(^{40}\text{Ar}, 2-3\text{n})^{246,245}\text{Fm}$ (see Sec. 3.1.2). The RIS study on these short-lived nuclei was only possible due to the development of a short RADRIS cycle [168]. Furthermore, a rotatable multidetector setup consisting of three silicon detectors was developed, enabling the simultaneous measurement of different wavenumbers for spectroscopy of long-lived nuclides. This development was part of the PhD thesis of J. Warbinek [175]. The isotope ^{254}Fm with a half-life of $t_{1/2} = 3.2$ h became therefore accessible.

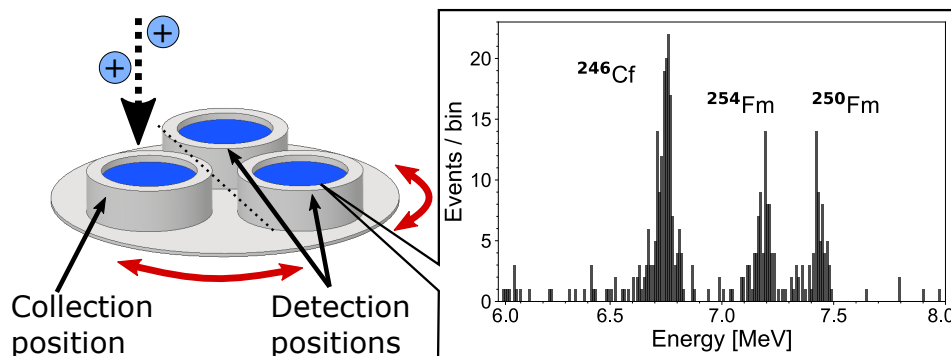


Figure 3.13: Schematic drawing of the rotatable multi-detector setup. The laser ions (blue) are collected to the PIPS detector on axis. The α spectrum of accumulated ^{254}Fm on one of the detectors in detection mode is shown on the right for a measurement time of approximately 5 days. Picture taken from Ref. [168].

A possibility to get access to ^{254}Fm is indirect production by using the 10% Electron Capture (EC) branch of ^{254}No to ^{254m}Md , which in turn decays by EC ($t_{1/2} = 28$ m) to ^{254}Fm . As a consequence, the resulting α spectrum shows both ^{254}Fm and ^{250}Fm from the α decay of ^{254}No . The rotatable multidetector setup was used for RIS on ^{254}Fm . One of the detectors was set on-axis to the collection position for a breeding time of 3600 s, before evaporation and laser ionization took place. Seven of these collection cycles were performed, accumulating the ions the PIPS detector in collection mode before the detectors were rotated. Thus, the subsequent decays can still be recorded, while the collection for the next measurement point takes place on the next detector, which is placed on-axis with the chamber. A schematic drawing of the rotatable detector setup for ^{254}Fm spectroscopy is given in Fig. 3.13.

For more short-lived nuclides, the single detector setup also used for $^{248,249,250}\text{Fm}$ spectroscopy can be modified to a movable double-detector setup to improve the overall efficiency by $\approx 65\%$. A detailed description of both the rotating detector and the movable double-detector is given in Ref. [168].

3.4 Upcoming extension to further Fm isotopes

In order to improve the understanding of the influence of the deformed $N=152$ shell gap on fermium isotopes, more isotopes across the shell gap have to be

3 Fermium laser spectroscopy

studied. Previously inaccessible isotopes, neutron deficient and neutron rich, short and long-lived, far off the shell gap, have to be tackled by newly developed detection concepts, to enable experiments at atom-at-a-time quantities. On-line and off-line laser spectroscopy experiments with direct and indirect production schemes and off-line production methods have to be combined and methodologically pushed forward.

^{255}Fm and ^{257}Fm are two more neutron rich fermium isotopes, on which recently narrowband off-line spectroscopy was performed at RISIKO. The samples were produced by reactor breeding. A ^{257}Fm sample obtained as a by-product from ^{252}Cf breeding for einsteinium spectroscopy at the High Flux Isotope Reactor (HFIR) at Oak Ridge National Laboratory (ONRL) was made available for spectroscopy at RISIKO in Mainz after it was not needed any longer for an investigation at Florida State University (see Sec. 3.2.2). ^{255}Fm was bred from a 290 pg (6.8×10^{11} atoms) ^{254}Es sample, which was irradiated with a high neutron flux at the research reactor at Institute Laue-Langevin (ILL) in Grenoble, France. After one week of irradiation and 4 days of cool down, the sample was shipped to the department of chemistry – TRIGA site at Mainz university, where α spectroscopy detected 1.0×10^9 atoms of ^{255}Es ($T_{1/2} = 39.8$ d) in secular equilibrium with its β^- decay daughter ^{255}Fm ($T_{1/2} = 20.1$ h). After chemical separation, four ^{255}Fm samples ranging from 2 to 9×10^6 atoms were deposited on a zirconium metal foil, which were inserted sequentially to the RISIKO Mass separator. Results of the narrowband spectroscopy on $^{255,257}\text{Fm}$ will be presented in Ref. [187], [175]. To investigate neutron deficient fermium isotopes, direct on-line production can be used, as described in Sec. 3.3 and Sec. 3.1.2.

In the framework of the expansion of fermium spectroscopy [187], calculations with different Energy Density Functional calculations are being provided by different theory groups. Hereby, Hartree-Fock-Bogolyubov (HFB) calculations with the functional Gogny D1M [189] and Skyrme-Hartree-Fock (SHF) calculations using the Fayans pairing functional Fy(IVP) [190] are performed at the mean-field level (see Sec. 2.2.2), [187]. To obtain values for $\delta\langle r^2 \rangle$ from HFB calculations, potential energy surfaces are modeled with blocked quasi-particles which match the reported spin and parity of the investigated isotope. For odd fermium isotopes, an equal filling approximation is applied to estimate the binding energy of the quasi particles, whereby the lowest energy is determined by a blocking of possible existing levels around the Fermi energy. Overall, a phenomenological configuration mixing is taken into account to consider possible deformation of the potential energy surface. For Fy(IVP) calculations, the used parametrization is an extension of the Fayans pairing functional customized for the treatment of heavy nuclei, allowing different proton and neutron pairing strength. A paper combining the spectroscopy measurements on the isotopes ^{245}Fm , ^{246}Fm , ^{248}Fm , ^{249}Fm , ^{250}Fm , ^{254}Fm , ^{255}Fm and ^{257}Fm with these nuclear theory calculations is currently in preparation [187].

3 Fermium laser spectroscopy

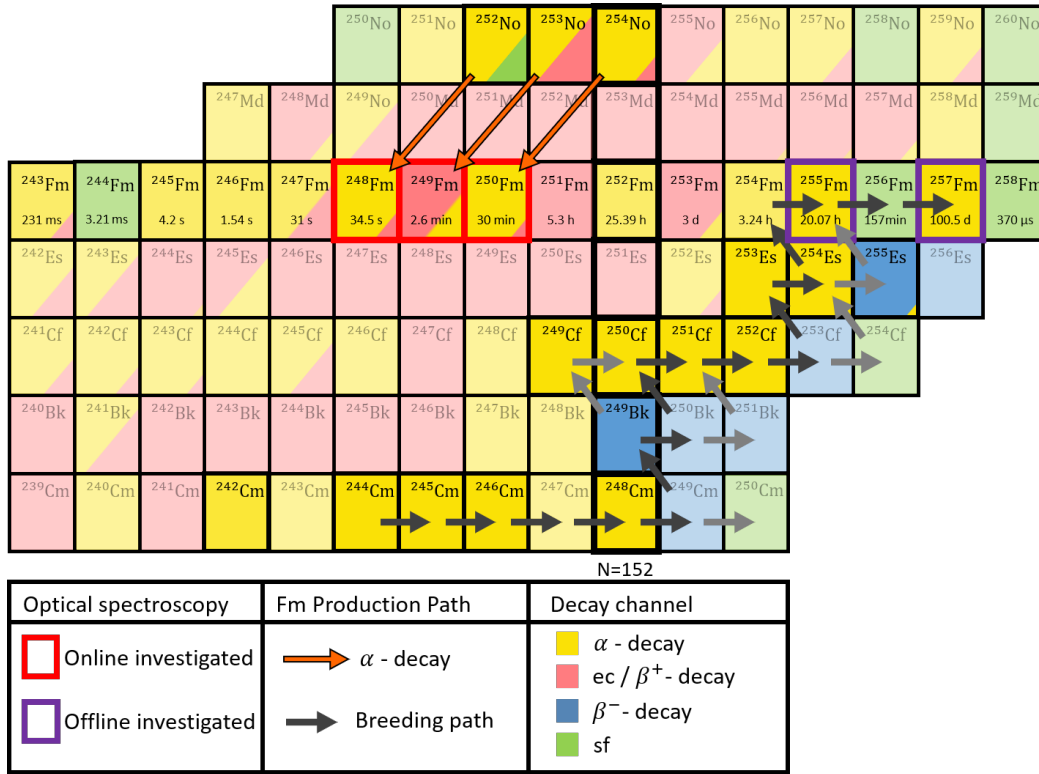


Figure 3.14: Production mechanism for the investigated fermium isotopes. On-line investigated Fm isotopes are marked with red borders, off-line investigated isotopes with violet borders. The production path is indicated by arrows. The decay path of the respective isotopes is colour coded. Previously spectroscopied isotopes are shown in full colour, fermium isotopes are shown in semitransparent colour. The half-lives $t_{1/2}$ of Fm isotopes and their No mother isotopes are given at the bottom of the boxes. Isotopes with $N=152$ neutrons are marked with slightly broader borders.

Two limiting factors for possible spectroscopy at RADRIS are the half-life $t_{1/2}$ and the decay mode for detection. For on-line spectroscopy, production rates on the orders of several hundred nb are required. Moreover, $t_{1/2}$ has to be between a few seconds and several hours. In the improved RADRIS setup from Ref. [168] the isotopes ^{245}Fm , ^{246}Fm , ^{248}Fm , ^{249}Fm , ^{250}Fm and ^{254}Fm are suitable for on-line spectroscopy. A picture of the different production mechanisms for on-line and off-line accessible fermium isotopes is given in Fig. 3.14.

Another principally suitable isotope for on-line spectroscopy at RADRIS is ^{243}Fm , with a short half-life of $t_{1/2} = 231$ ms. The short RADRIS cycle, developed in Ref. [168] for spectroscopy of short-lived ytterbium isotopes, was successfully implemented for ^{154}Yb with a half-life of $t_{1/2} = 0.4$. The limiting factor is hereby the production cross section (see Sec. 2.4.2), which is not specified in Ref. [121], but presumably small. Therefore, spectroscopy on ^{243}Fm is not yet possible. The same applies for ^{247}Fm ($t_{1/2} = 31$ s), which

3 Fermium laser spectroscopy

could be detected due to a 64% α decay branch to ^{243}Cf , which features a production cross section of $0.2 \mu\text{b}$ for the reaction $^{239}\text{Pu}(^{12}\text{C},4\text{n})^{247}\text{Fm}$ [120]. Another possibility to obtain ^{247}Fm is the indirect production by the reaction $^{207}\text{Pb}(^{50}\text{Ti},2\text{n})^{255}\text{Rf} \xrightarrow{\alpha} ^{251}\text{No} \xrightarrow{\alpha} ^{247}\text{Fm}$ demonstrated by Ref. [191].

For the isotopes ^{251}Fm and ^{253}Fm , the limited production is not the only complication for spectroscopy at RADRIS. Alternatives to the production mechanisms in Sec. 2.4.2, as the use of the alternative fusion evaporation $^{238}\text{U}(^{18}\text{O},5\text{n})^{251}\text{Fm}$ with cross section of 4000 nb [192] or the indirect production of ^{253}Fm from a double β^+ or EC decay of $^{207}\text{Pb}(^{48}\text{Ca},2\text{n})^{253}\text{No}$ [193] does not improve the situation. The recoil energy of ^{251}Fm is hereby with 6.9 MeV comparatively small [192]. The α -decay branch of ^{251}Fm and ^{253}Fm is about 5% and 12% to ^{247}Cm or ^{249}Cm , respectively. The half-life of ^{251}Fm amounts to 5.2 h , such that this isotope is principally suitable for spectroscopy investigations with the rotating multi-detector setup. However, ^{253}Fm with a half-life of 3 days is neither ideal for either on-line studies with the current or improved RADRIS setup from Ref. [168], nor for off-line studies with the RISIKO setup. Without further extensions of the respective spectroscopy setup, a spectroscopic investigation of ^{253}Fm is not practical.

For off-line spectroscopy, the isotopes ^{254}Fm , ^{255}Fm and ^{257}Fm are suitable, as mentioned above. The isotope ^{252}Fm ($t_{1/2} = 25.39 \text{ h}$) is a very interesting candidate for off-line spectroscopy, but is not available in sufficient quantities for in-source spectroscopy, e.g., at the RISIKO setup. Moreover, on-line production is possible, e.g., by the reaction $^{238}\text{U}(^{18}\text{O},4\text{n})^{252}\text{Fm}$ with a cross section of 750 nb [194] or $^{248}\text{Cm}(^{44}\text{Ca},^{40}\text{S})^{252}\text{Fm}$ with a cross section of $20.9 \mu\text{b}$ [119]. Another possibility for the production of ^{252}Fm is the indirect production through the electron capture decay of ^{252}Md , which in turn can be produced in the reaction $^{238}\text{U}(^{19}\text{F},5\text{n})^{252}\text{Md}$ of about 500 nb and a low recoil energy of 7.3 MeV [192]. Therefore, spectroscopic experiments on ^{252}Fm are challenging and require further advancing of detection methods.

4 Limitations and opportunities of in-gas cell spectroscopy

Gas-filled cells, as the RADRIS cell, are a widely used tool to stop and thermalize high-energy products from nuclear reactions for subsequent laser spectroscopic experiments. Both gas stoppers and ion guides are well established for the on-line investigation of various isotopes [8]. Gas stopping cells can be operated with various gases at various pressures to thermalize fusion products with energies of up to several GeV. In resonance ionization spectroscopy in a gas cell, mostly argon buffer gas is used to enable the recombination of the fusion products [8]. While the resolution of resonance ionization spectroscopy in gas stopper cells is hampered by pressure broadening, the use of gas ion guides can improve the situation. Here, the fusion products generated in a gas filled cells are evacuated in a gas-jet, in which spectroscopy is performed. Due to the homogeneous low-pressure and low-temperature environment in a hypersonic gas-jet, the spectral resolution can be improved to a few hundred MHz [195]. Proof-of-principle experiments on actinium isotopes around the $N=126$ shell closure were performed with the gas-jet technique in [196]. A detailed description of a high-resolution gas-jet setup for spectroscopy in a supersonic gas flow created by a de Laval nozzle is given in [160]. Other possibilities for RIS in gas-filled optical cells are Laser Induced Fluorescence spectroscopy (LIF) [197], RAdioactive Decay detected Optical Pumping (RADOP) [198] and Ion-Guide-detected Resonance Ionization Spectroscopy (IGRIS) [199], which differs only by the detection method from RADRIS [125]. In comparison to other possibilities for resonance ionization spectroscopy experiments apart from RIS in gas cells as hot cavity in-source spectroscopy (e.g [159]), collinear RIS (e.g. [200]), RIS in magneto-optical atom traps (e.g. [201]) or ion traps (e.g. [202]), the spectral resolution in a gas stopping cell is always hampered by pressure broadening. The pressure and nature of the chosen buffer gas affects hereby intrinsically the spectral resolution. For the RADRIS setup, the choice of argon as inert buffer gas at a pressure of about 90 mbar is crucial to achieve the required stopping forces for the high energy fusion evaporation products in the limited volume of the experimental chamber. Feasibility studies on ^{245}Fm in 95 mbar argon in comparison to 125 mbar helium and a reduced voltage gradient setting to avoid discharges resulted in a relative efficiency loss of about 40% [19].

Moreover, the drift properties of the ions through the buffer gas are a limiting factor for the transportation time to detector and the overall efficiency. In the

4 Limitations and opportunities of in-gas cell spectroscopy

current RADRIS setup with an argon buffer gas pressure of 90 mbar and a potential gradient of ≈ 29 V/cm from the filament to the grounded detector, the transportation time for 84.13% of the investigated ^{154}Yb ions ($t_{1/2} = 0.4$ s) is 0.33 s in argon [168]. The relative ion transport efficiency is thereby not significantly influenced when the gradient is halved, but reduced to 50% for 25% of the nominal voltage settings given in Tab. 3.3 [19].

Another limiting factor is the stopping distribution of the fusion evaporation residues (recoils) arriving in the RADRIS cell [195], which, in combination with diffusion processes, results in a broadened arrival time distribution of the recoils on the detector. A fast potential switching of the filament by inserting a fast high-voltage switch enabled the implementation of a short RADRIS cycle, which is still limited by a waiting time of 0.2s between the potential switch and the filament heating pulse to allow a settling down of the stopped recoil ions [168]. A further shortening of the cycle might be possible in other inert buffer gases such as helium or neon [19]. In Fig. 4.1, the mobility and diffusion limited arrival time spectra of directly to the PIPS detector guided ytterbium ions is shown, taken from [168].

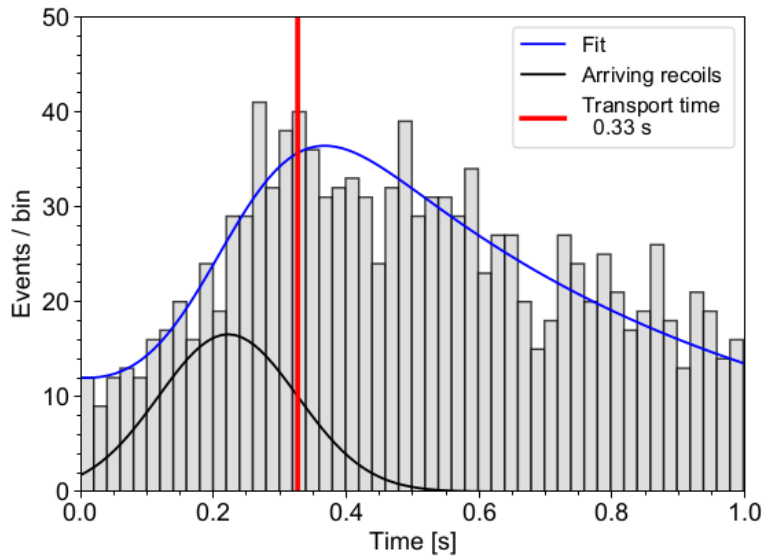


Figure 4.1: Mobility and diffusion limited arrival time spectra for Yb ions on the PIPS detector, taken from [168]. In black, the assumed Gaussian time distribution for the ions to reach the detector is shown. The blue curve shows the fit of the increased width of the ^{154}Yb ions and their subsequent decay products stopping distribution due to diffusion processes.

While the drift behaviour of ions in gas is a tedious side effect for spectroscopy investigations at RADRIS, it can on the other hand be used for systematic mobility studies of ion species. These mobility studies help to gain an insight into

4 Limitations and opportunities of in-gas cell spectroscopy

the interaction potentials of the ion drifting in neutral buffer gas. Moreover, the mobility can be used to investigate the electronic structure of the drifting species. Since the extension of resonance ionization spectroscopy to lawrencium, the heaviest actinide with $Z=103$ and further to super heavy elements is very challenging, mobility measurements may provide an alternative way to access the electronic configuration of the ion under investigation [45], [203]. Finally, an alternative way of optical spectroscopy can be obtained by combining resonant laser excitation with mobility measurements, which at the same time represent an electronic state chromatography measurement [26], [204]. Since the ions can be investigated directly, no neutralization on a filament is needed giving access to even more short lived ion species and avoids adsorption losses, such that investigations for atom-at-a-time quantities are feasible. Therefore, mobility studies for electronic structure investigation are especially interesting in the region of super-heavy elements, where production cross sections decrease with increasing Z . In the following chapter, the development of an actinide ion mobility spectrometer is presented. This spectrometer will be mainly used for mobility measurements at different pressures, electric fields and temperatures to study interaction potentials, which helps to benchmark theoretical “standard” *ab-initio* calculations.

5 The development of an Actinide Ion Mobility Spectrometer

Gas phase chemistry with single atoms has helped to characterize the chemical properties of superheavy elements as copernicium ($Z=112$) [205] and flerovium ($Z=114$) [206]. Ion Mobility Spectrometry (IMS) may provide an alternative to probe superheavy ions. IMS is a powerful tool to investigate electronic configurations of ions by their difference in mobility (see Sec. 2.6.1). Moreover, IMS studies provide benchmark data for theoretical *ab-initio* calculations to deepen the understanding of ion-atom interaction potentials. Large scale structure calculations of open-shell atoms and ions are mostly performed with computation packages, as described in Ref. [207] for open d- and f-shell elements. In addition, diffusion coefficients, the mobility, collision integrals and momentum transfer cross sections can be predicted with a relatively high accuracy from the ion-atom interaction potential [149] even for meta-stable ionic states.

The study of actinides and transactinides is an especially interesting field of research, since relativistic effects cannot be neglected any longer. Ion mobility studies can help to set a measure for these effects and thus provide an alternative to historical deductions like adsorption enthalpy measurements and molecule formation studies in aqueous solution or gas phase and final comparison to lighter homologues [208] [209].

As explained in Sec. 2.1.7, relativistic effects have an influence on the valence electrons, which occupy the $5f$ -, $6d$ -, and $7s$ -orbitals in the actinides. Previous IMS measurements in the lanthanide and actinide region were very limited in resolution. Therefore, a new cryogenic drift cell has been developed, which is presented in this chapter. In the following sections, results from lanthanide and actinide ion mobility measurements, the experimental setup of the ion mobility spectrometer and developments towards ion mobility measurements in the actinides are described.

5.1 Mobility measurements for electronic-state chromatography

The measurement of mobility and diffusion coefficients by obtaining the drift time of ions through a gaseous atmosphere in electrostatic fields is a widely investigated technique. Around 1960, the drift tube spectrometer was developed, such that ion-neutral interactions were obtained for positive and negative ions in inert noble gases (He, Ne, Ar, Kr, Xe), reactive gases like H₂, N₂, O₂, CO, CO₂, H₂O, NO and CH₄ and admixtures of reactive gases in inert gases for varying E/N [210]. Thereby, mobility measurements have been performed for a variety of ionic species, from monoatomic ions [147] to complex proteins [211].

Already in 1988, the sensitivity of ion mobility measurements on the electronic configuration was observed by mobility studies on $^{56}\text{Ba}^+$ in helium. The measurements showed a 9% deviation from the mobility of $^{55}\text{Cs}^+$ due to the presence of the occupied $6s$ orbital in Ba^+ [212], which Cs^+ lacks in its ground state [210]. More recent studies of lanthanide ion mobilities were able to prove the sensitivity on changes between singly to fully occupied s orbitals, as observed in a 13.8%-difference between the mobility of $^{70}\text{Yb}^+$ ($6s4f^{14}$) and $^{71}\text{Lu}^+$ ($6s^24f^{14}$) in helium [213]. When studying different excited states and ground states of the same ionic species, large discrepancies can arise depending on the electronic configuration of the state enabling electronic-state chromatography. This was first proven for mobility measurements of the first-row transition metal ions $^{22}\text{Ti}^+$ to $^{30}\text{Zn}^+$ in helium. The differences in K_0 were largest for different electronic configurations in the same ion ($3d^n$ and $3d^{n-1}4s$), only minor between $3d^{n-1}4s$ states, and not resolvable for $3d^n$ states [23]. Hereby, the temperature may have to be varied to distinguish the investigated excited state and the ground state. This principle can be extended to other chemical elements to enable the distinction between metastable ionic states and their ground states. In $^{29}\text{Cu}^+$, the configurations $[\text{Ar}]d^{10}$ and $[\text{Ar}]3d^94s^1$ drifting in helium exhibit a mobility deviation of about 33% [214] due to the occupied s orbital in the meta-stable state. In the same work, the dependency to resolve the excited state with respect to the temperature and the E/N value and the nature of the chosen carrier gas was demonstrated, but revealing also an impact of the laser power, the ion source geometry, and carrier gas impurities.

Overall, these experimental findings corroborate the assumption that ion-atom interaction potentials and thus ion mobilities are highly sensitive to the underlying electronic configurations of the measured species [45]. An extension of mobility measurements towards electronic-state chromatography and state-selective ion chemistry is already being implemented.

5.2 Predictions of the electronic structure of lanthanides and actinides

The sensitivity of mobility measurements to the underlying electronic configuration of the drifting species enables the investigation of relativistic effects, which may influence the electronic level structure (see Sec. 2.1.7). This makes systematic mobility measurements an ideal tool to study the electronic configuration of actinides from Ac ($Z=89$) to Lr ($Z=103$). The level structure in the actinides is very dense [24], such that the diversity in electronic configurations, interatomic forces, bond lengths, enthalpies and the chemical behaviour altogether is increased [45]. Moreover, the levels form terms, whereby several terms build a configuration, such that the hierarchy of different configurations is not trivial due to configuration mixing and a level has to be identified with the help of theoretical calculations [125]. Only since 1945 the actinides are known to fill the $5f$ shell of electrons [215], which makes them homologue to the lanthanide series ($Z=57-71$), where the $4f$ shell is filled. In comparison to the lanthanides, the actinides ground state configurations show more variation [152].

This behaviour is visualized in Fig.5.1a and 5.1b. In the case of singly charged ions, the electric configuration obtained from theoretical Multi-Configuration Dirac-Fock calculations (MCDF) varies even further, as predicted by [46] and depicted in Fig. 5.1c and 5.1d. Ionic radii calculations for lanthanides and actinides are also given by [46], but excluded here since experimental mobility data are primarily influenced by the ion-atom interaction (see Sec. 2.6.2) [125]. The region between Pu^+ and Cf^+ with $Z=94$ and $Z=98$, respectively, is especially interesting since the electronic configuration differs between the neighbouring ions. In the lanthanide series, systematic ion mobility studies have already been carried out [150], [22]. The results proved that ion mobility studies are highly sensitive to the underlying electronic configurations (see Sec. 5.3). Therefore, ion mobility studies are foreseen to be performed in the actinide region.

5.3 State-of-the-art ion mobility measurements in lanthanides and actinides

As the electronic structure of actinides is quite complex and the availability is limited (see Sec. 2.4.1), initial mobility studies were performed on isotopes from the homologue lanthanide series in 2009 [150], [22]. Systematic low-field mobility measurements were carried out on six different monoatomic lanthanide ions with the ion mobility spectrometer described in Sec. 5.5. $^{151}_{63}\text{Eu}$, $^{156}_{64}\text{Gd}$, $^{159}_{65}\text{Tb}$, $^{165}_{67}\text{Ho}$, $^{nat}_{68}\text{Er}$ and $^{174}_{70}\text{Yb}$ were examined by mobility measurements in argon gas. In principle, any pure inert gas can be chosen as a carrier gas to avoid the formation of chemical compounds. However, small admixtures of reactive gases can be useful for further mobility interaction studies [125]. In this case, argon gas was chosen,

5 The development of an Actinide Ion Mobility Spectrometer

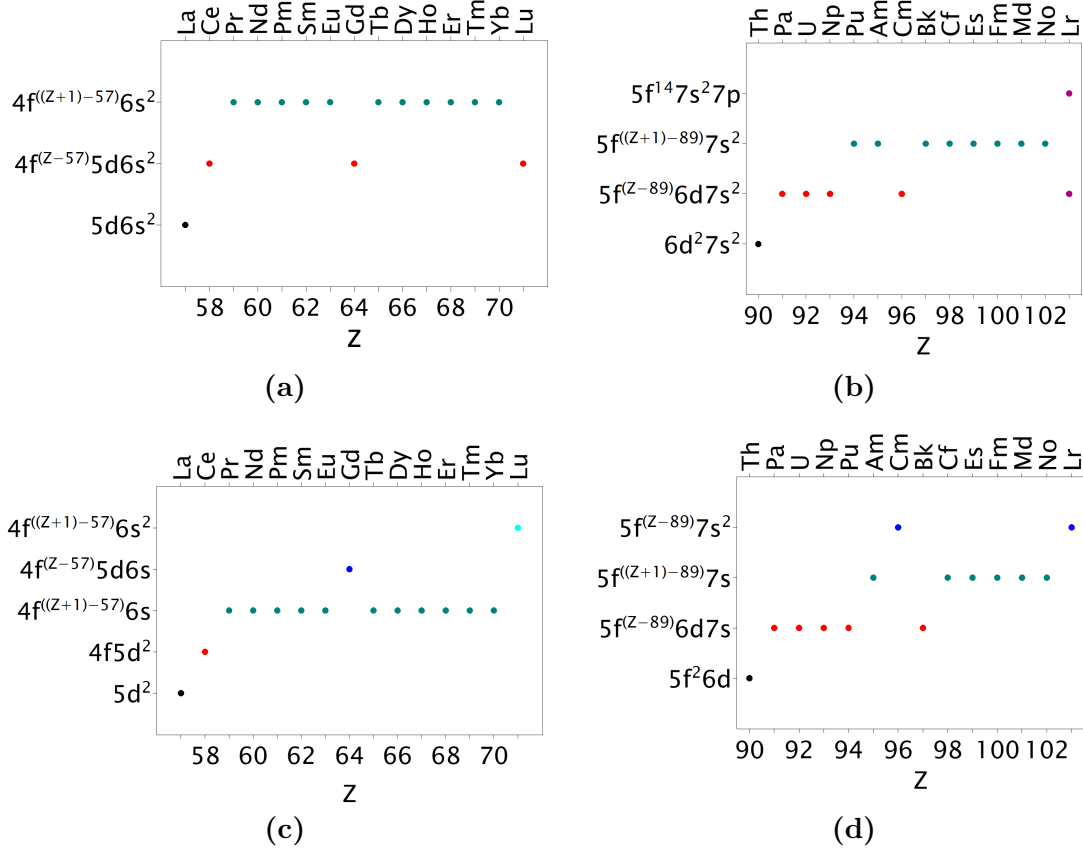


Figure 5.1: Electronic configuration of (a): lanthanide and (b): actinide ground states as well as (c): singly charged lanthanide and (d): actinide ions. The atomic number Z is denoted on the bottom, the element name at the top of each Figure.

since it provides more efficiency in stopping fusion products and minimizes the spacial distribution of the thermalized ions [150].

The reduced mobility K_0 (see Sec. 2.6.1) of the different lanthanides is tabulated in Tab. 5.1 together with the used laser excitation step. For all investigated lanthanides except $^{156}_{64}\text{Gd}$, the reduced mobility is found to be similar within the error bars, such that the mobility of different isotopes of the same element cannot be resolved with the IMS setup. In contrast to surrounding lanthanide cations, for which the $4f$ shell is gradually filled, Gd^+ exhibits in addition an occupied $5d$ shell. This has significant implications on the ion-atom interaction potential, because the Coulomb repulsion term and the attractive dispersion term of this potential depend on the electron shell occupation (see Sec. 2.6.3). The dispersion is caused mainly by the charge-induced dipole field of the argon atom on the ion itself [150]. Ionic species with different electron configurations and distinct polarizabilities are therefore expected to have different ion-atom interactions and consequently distinguishable ion mobilities. In the case of Gd^+ , the mobility is

5 The development of an Actinide Ion Mobility Spectrometer

reduced by 8% in comparison to the other lanthanides. In 2017, reduced mobilities of Eu^+ , Gd^+ , Yb^+ and Lu^+ were measured in helium, revealing a $\approx 7\%$ larger mobility for Gd^+ and a $\approx 14\%$ smaller mobility for Lu^+ in comparison to Yb^+ [216]. The larger mobility of Gd^+ in comparison to the other lanthanides is explained by a stronger spin-orbit coupling when the ions are drifting in helium, while the mobility of Gd^+ in heavier buffer gases is smaller than the other lanthanides [217].

Lanthanide	$\bar{\nu}$ [cm ⁻¹]	K_0 [cm ² /Vs]	$\Delta K_{0,\text{err, stat}}$ [cm ² /Vs]	$\Delta K_{0,\text{err, sys}}$ [cm ² /Vs]
$^{151}_{63}\text{Eu}$	21761.3	1.844	± 0.002	± 0.019
$^{156}_{64}\text{Gd}$	21857.5	1.692	± 0.001	± 0.018
$^{159}_{65}\text{Tb}$	23107.3	1.834	± 0.002	± 0.019
$^{165}_{65}\text{Ho}$	24660.8	1.839	± 0.001	± 0.019
$^{168}_{68}\text{Er}$	24943	1.839	± 0.004	± 0.019
$^{174}_{70}\text{Yb}$	25068.2	1.837	± 0.001	± 0.019

Table 5.1: Lanthanide mobility measurements with respective ionizing step. $\bar{\nu}$ is the first step for resonant ionization, the second step was provided by a Xe:F operated excimer laser at 351 and 353 nm. Data taken from Ref. [150]

In 2003, resonance ionization spectroscopy was performed on $^{255}_{100}\text{Fm}^+$ [136], [172], [134], $^{94}\text{Pu}^+$ and $^{95}\text{Am}^+$ [218], [219]. During the measurement campaign on $^{255}_{100}\text{Fm}$ reported in Ref. [136], two resonant ground-state transitions at energies of 25099.8(2) cm⁻¹ and 25111.8(2) cm⁻¹ were observed (see Sec. 3.1.1). During the extraction, the drift time from the filament position to the nozzle was extracted for the ionized $^{255}_{100}\text{Fm}$. Moreover, the drift time of the fermium α -decay daughter $^{251}_{98}\text{Cf}^+$ and the $^{238}\text{UO}^+$ dimer originating from the sample preparation were obtained. Since the drift path in these experiments was only 3.5 cm long, the drift time difference between $^{255}_{100}\text{Fm}^+$ and $^{251}_{98}\text{Cf}^+$ was only minor, leading to a large uncertainty in K [172].

The same challenges apply for the drift time measurements of $^{94}\text{Pu}^+$ and $^{95}\text{Am}^+$, revealing a slightly shorter drift time of $^{95}\text{Am}^+$ [218]. The drift time difference was used to estimate the relative change in charge radii, which is about $\Delta r^{\text{Fm}^+,\text{Cf}^+}/r^{\text{Cf}^+} \approx -2\%$ [136] and $\Delta r^{\text{Pu}^+,\text{Am}^+}/r^{\text{Pu}^+} = -(3.1 \pm 1.3)\%$ [219], respectively. However, due to large uncertainties, both previous actinide drift time measurements are not very reliable. To extract more precise mobility values for the actinides, completely new and accurate measurements are needed. In Fig. 5.2a and 5.2b, the drift time measurements from Ref. [136] and Ref. [218] are depicted.

For the systematic mobility measurement of lanthanides, an ion mobility spec-

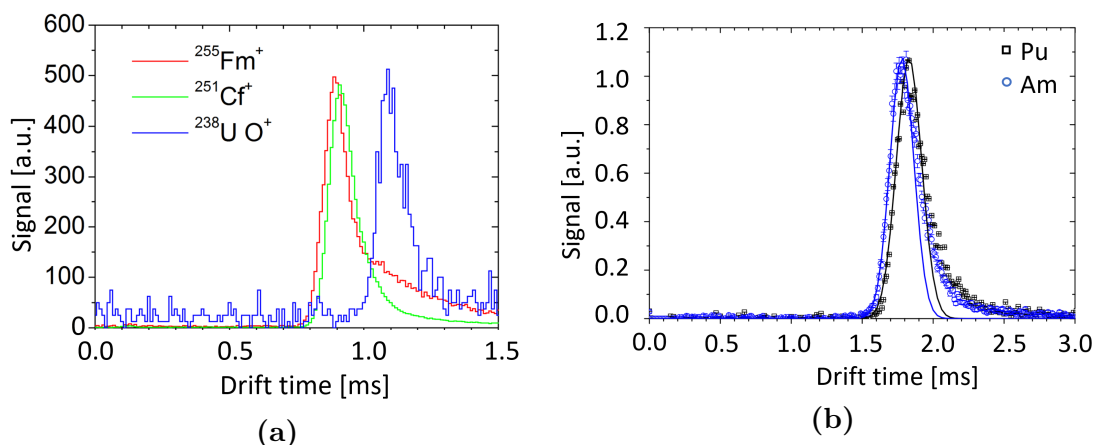


Figure 5.2: (a): Drift time measurement of $^{255}_{100}\text{Fm}$, $^{251}_{98}\text{Cf}$ and $^{238}\text{UO}^+$, taken from Ref. [136]. (b): Drift time measurement of ^{94}Pu and ^{95}Am , taken from Ref. [219].

trometer was used [150], which is described in the following section. Since systematic measurements at different temperatures cannot be achieved with this setup, a new cryogenic drift cell has been developed within the framework of this thesis, which is described in Sec. 5.5.2.2.

5.4 Mobility predictions for singly charged lanthanide and actinide ions

Ion-neutral interaction potentials can be obtained from theoretical *ab-initio* calculations with high accuracy, e.g., within 0.05% from Coupled Cluster calculations with Singles, Doubles and non-iterative Triples (CCSD(T)) [146].

In 2020, theoretical calculations of the ion interaction potentials and of the ion mobility over a wide range of temperatures were performed for several monoatomic lanthanide and actinide ions in helium and argon gas. To solve the Boltzmann equation for ions drifting in gas, the Gram-Charlier expansion of ion distribution was used and to obtain classical collision integral values $\Omega^{(1,1)}$ (see Sec. 2.6.2), a program from Viehland was applied [21]. The interaction potentials were calculated from the CCSD(T) method using small-core (28-electron) and large-core (60-electron) effective core potentials adjusted for an isotropic scalar relativistic approximation for lanthanides and actinides, respectively. The calculations are based on the assumption, that the properties of weakly bound dimers can be described by the properties of the individual monomers, such that ion-atom interaction potentials are sensitive to the electronic structure of the constituting ion [203]. The detailed theoretical models and the strategies for basis set development are given in Ref. [21]. The calculation method was tested on Eu^+ , Gd^+ , Yb^+ and Lu^+ and compared to experimental values obtained in mobility

studies in helium and argon gas from Ref. [216] and Ref. [22], respectively. From both experiment and theory one reports a general increase of the $4f^m6s$ ions in helium with increasing Z , while the mobility of these configurations in argon is almost constant [203]. Overall, a good agreement between experimental and theoretical ion mobilities of lanthanides is achieved. However, experimental data for a wider temperature range are needed to reveal further features of a particular ion-neutral interaction.

The extrapolation of the calculation towards actinide cations cannot guarantee the same accuracy as for lanthanides, since the ion-atom interaction potentials depend on the density of outer electrons such that relativistic effects and electron correlations may not be fully considered. Furthermore, an accurate treatment of the spin-orbit coupling, the development of appropriate basis sets and of the virtual space may complicate the theoretic treatment.

In Ref. [203] and [21], the mobilities for the following actinides cations were calculated: ${}_{89}^{227}\text{Ac}^+$ ($7s^2, {}^1S$), ${}_{95}^{241}\text{Am}^+$ ($5f^77s, {}^9S^\circ$), ${}_{96}^{247}\text{Cm}^+$ ($5f^77s^2, {}^8S^\circ$), ${}_{102}^{254}\text{No}^+$ ($5f^{14}7s, {}^2S$) and ${}_{103}^{255}\text{Lr}^+$ ($5f^{14}7s^2, {}^1S$). The interaction potentials of actinides with $7s$ and $7s^2$ outer shells differ significantly from each other, while the status of the inner f -shell occupation has a more pronounced effect than in case of lanthanides. In general, interactions of actinide ions with argon are stronger than interactions with helium. Stronger interactions result hereby in a smaller mobility. The derived ion mobilities show a similar trend to the homologue lanthanides with mobility in helium increasing with Z and decreasing with increasing Z in argon. The relative mobility differences for the pairs $\text{Cm}^+ - \text{Am}^+$ and $\text{Lr}^+ - \text{No}^+$ are predicted to about 10–15% at room temperature in helium, such that the $7s$ and $7s^2$ ions should be well separated in the time spectra. For both buffer gases, the occupation of the outer ns shell leads to a smaller variation of the mobility than the effect on the lanthanides for an occupied $5d$ shell. However, systematic measurements of ion mobilities for varying temperatures or E/N values are needed for monoatomic actinide ions to assess the quality of the used *ab-initio* models and to give a benchmark for further theory developments. Probing actinide ions by IMS may help to better model global potentials in the *ab-initio* framework [21].

5.5 Experimental setup of the ion mobility spectrometer

To study the ion-atom interaction potential of actinides, the ion mobility spectrometer developed in Ref. [150] will be used and is adapted for the new challenges. The spectrometer is redesigned to be an Actinide Ion Mobility Spectrometer (AIMS). AIMS investigations will enable the systematic mobility study of monoatomic actinide ions. Moreover, molecular actinide ions will be accessible, due to unavoidable chemical reactions with impurities of the gas. Hereby,

monoatomic ions can be easily separated by drift time from molecular ions. In Sec. 5.5.1, the maintained drift and detection chamber are shortly described. The new parts of AIMS are presented in Sec. 5.5.2, with a focus on the development of a cryogenic drift cell for systematic ion mobility measurements at varying temperatures and different E/N values in Sec. 5.5.2.2.

5.5.1 Maintained parts of the old IMS apparatus

For ion mobility investigations across the actinides, the spectrometer described in Ref. [150] was re-inaugurated within the framework of this thesis. In this section, the functionality and the major components of this IMS apparatus are briefly described. As described in Sec. 2.6.4, the IMS consists of a drift chamber, a quadrupole ion guide and a detection section. Further details can be found in Ref. [150]. The maintained parts of the mobility spectrometer consist of a drift chamber and a detection part.

5.5.1.1 Drift chamber

In Fig. 5.3, a cross section view of the drift cell is depicted. The electric field in the drift chamber is provided by 22 ring electrodes, which span a total length of 420 mm. The drift distance from the filament position to the nozzle is thereby about 320 mm. All ring electrodes are made of stainless steel, which are electropolished to reduce the risk of gas discharges. The last five electrodes are shaped like a funnel. The electrode radius decreases thereby from 90 mm inner diameter of the outer most electrode to the nozzle with a 0.5 mm throat diameter, which separates the drift section from the detection part. An entrance window provides the possibility to use the apparatus in on-line experiments.

For off-line experiments, strips of lanthanide metal foils are mounted on a filament holder. By resistive heating, a neutral atom cloud is created. This atom cloud is then ionized in a two-step photo ionization process by the combination of a pulsed Nd:YAG laser and an Optical Parametric Oscillator (OPO) (see Sec. 5.5.2.3), such that the ions are created in a well-defined volume at a fixed starting time. For the experiments in Ref. [150], the ions were produced from commercially available 25- μm -thin lanthanide foils of 99% isotopic purity, which were mounted in multi layers on the filaments holder. Holmium was hereby consistently included to the multi layer filaments and used as a reference element, since its stable isotope $^{165}_{67}\text{Ho}$ enables precise identification in the mass spectrum of the sample. Before the re-inauguration of the drift cell, the two-step ionization was obtained by the combination of a tunable dye laser (Lambda Physik, FL 2001) and an excimer laser (Lambda Physik, EMG MSC 103), both pulsed with 20 Hz, which were guided to the cell by one multi-mode silica glass fiber.

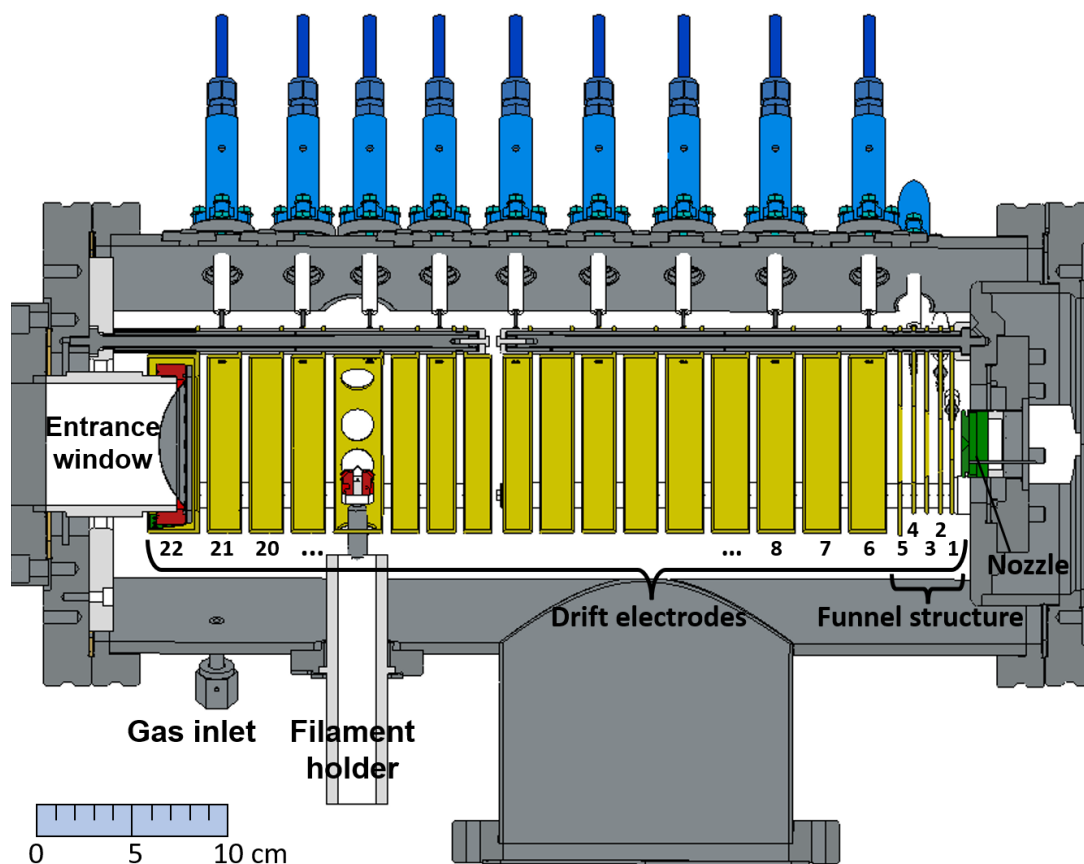


Figure 5.3: IMS Drift Cell. The entrance window is foreseen for on-line experiments. For an off-line operation of the setup the ions are produced from the filament by heating a metal sample and ionizing the atomic species in a two step photo ionization process. The electric field is created by the drift electrodes.

The chamber is filled with argon gas, and the pressure is regulated such that the gas number density E/N is below $2 \cdot 10^{-17} \text{ Vcm}^2 = 2 \text{ Townsend (Td)}$ to fulfill the low-field conditions. Only under these conditions, the diffusion can be assumed to be constant. This is the case for an argon pressure of 40 mbar, which is obtained for a 0.50-mm-diameter nozzle at a gas flow rate of 1.5 mbar l/s. To provide maximal gas purity, the argon gas (ideally Argon 6.0 with a purity of 99.9999%) is purified further by a gas-getter system (SAES, model PS4-MT3-R-2). Moreover, the drift cell can be heated by heating bands up to 250°C to evaporate water from the metal surfaces.

After the ions of choice are produced in the two-step ionization process, they drift along the electric field lines in the gaseous atmosphere. At the end of the drift path, the ions reach the nozzle, which separates the drift chamber from the detection part.

5.5.1.2 Detection section

To avoid background during ion detection, a mass separation is required prior to the detection. The mass separation is ensured by a quadrupole mass filter QMF (Balzers, QMG 311), where radio frequency and direct current voltages are applied to the four QMF rods. The ion motion in the dynamic electric field is dependent on the mass-to-charge ratio of the ions [220]. The equation of motion can be solved by a set of Mathieu parameters a and q , derived in, e.g., Ref. [221], which are related to the DC and RF voltages, respectively. According to the choice of Mathieu parameters and the a/q ratio, the ions either follow a stable trajectory and oscillate transversally with limited amplitudes or are lost, such that the mass resolution can be adjusted to down to 0.1 u. Through the QMF control unit, the RF potentials can be manipulated, to reach the desired a/q value. As a result, only the ions with the mass-to-charge-ratio of choice e/m are transmitted.

The used mass filter can select ion masses up to 300 atomic mass units (u) and can be controlled via an analog interface by the data acquisition and control system, which is further explained in Sec. 5.5.2.4 and [222]. Other possibilities for the mass analysis in mass spectrometry, apart from a quadrupole mass filter, are given by time-of-flight spectrometers [223], sector field spectrometers which act as Wien-Filters [224], and quadrupole ion traps as Penning traps [225].

After the QMF, a 90° electrostatic deflector deflects the filtered ions, which are then focused by electrostatic lenses before being detected by a channel electron multiplier detector or channeltron (Sjuts, CEM, KBL 15RS) [226].

In the previous setup for mobility measurements on lanthanides, a differential pumping section was placed between the drift chamber and the detection section, to ensure a pressure reduction to $< 10^{-5}$ mbar in the detection section. The low pressure is needed for a proper operation of the QMF and the channeltron [227]. The guiding of the ions through the differential pumping section was ensured by a miniature Radio Frequency Quadrupole ion guide (mini RFQ). A brief description of the old differential pumping sections and the detection sections is given in the appendix (see Sec. 7.3). For AIMS, the connection between the drift chamber and the detection section was completely revised, allowing the integration of a cryogenic drift cell in setup, which is described in Sec. 5.5.2.2 and 5.5.3. In Fig. 5.4, a technical drawing of the detection section is shown.

5.5.2 New parts for the AIMS apparatus

5.5.2.1 Preliminary considerations

As motivated in the previous sections, measurements at different E/N -parameters can give valuable information about interatomic interaction potentials. The larger E/N , the narrower is the arrival time distribution. As a consequence, the uncertainty in the determination of the mobility parameter decreases. In contrast,

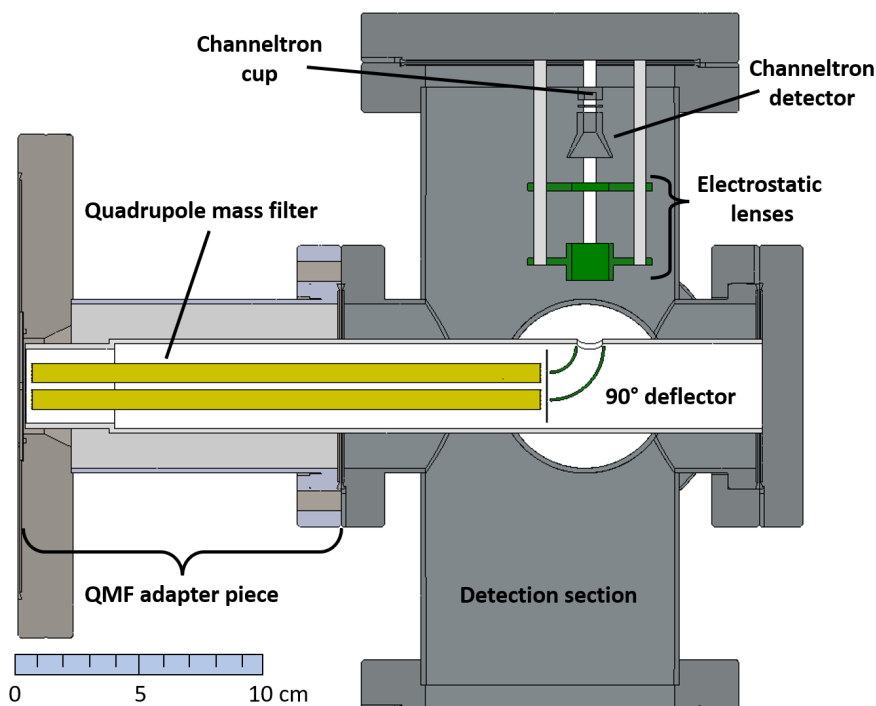


Figure 5.4: IMS detection section accommodating the quadrupole mass filter. The surviving ions with the proper mass to charge ratio are deflected towards a channeltron detector, where they are registered.

the longitudinal and transversal diffusion coefficients D_L and D_T are the same at small E/N values. For singly charged ions, $D_L = D_T = D$ is directly linked to the mobility K by the Einstein equation 2.33 (see Sec. 2.6.1). Varying E/N can be achieved by regulating the gas pressure or the electric field, whereby the limitations are given by the geometry of the drift cell, which together with the pressure determines the critical voltage for gas discharges. The influence of decreasing E/N for the drift cell geometry shown in Fig. 5.3, has been studied in Ref. [150], revealing ion diffusion losses for very low E/N values. Extraction efficiencies depend thereby on the friction forces in the transition zone between nozzle and subsequent ion guide electrodes. Moreover, small electric fields result in broad arrival time distributions due to diffusion. It is therefore more appropriate to choose a moderate electric field and vary the gas pressure. This possibility is to be implemented in the new setup.

At constant E/N values, the arrival time distribution can be influenced by the gas temperature T according to Eq. 2.33. For the previous measurements, the gas temperature was room temperature (≈ 300 K), which results in a relatively broad Arrival Time Distribution (ATD). To improve the width of the ATD, which roughly scales with $\frac{1}{\sqrt{T}}$, the gas temperature should be decreased. Furthermore, through systematic measurements at different gas temperatures and various buffer gases, “standard” *ab-initio* calculations describing the interaction of heavy ions

with noble gases can be assessed. In addition, by choosing the appropriate temperature, meta-stable ionic states, once created, can be resolved from the ground states [23].

5.5.2.2 Developments towards actinide ion mobility spectrometry

For systematic ion mobility studies of different actinide ions, a redesign of the differential pumping section of the spectrometer used in Ref. [150] will be implemented. This new vacuum section will allow better evacuation of the gas emerging from the nozzle in the transition zone. To provide the possibility of varying the drift temperature between 300 K and 100 K, a cryogenic drift tube is placed in the vacuum section. The cryogenic drift cell follows the concept used for ion mobility measurements on lighter transition metals [228], [229]. The distance from the nozzle exit to the QMF will only slightly change from originally 388 mm to 407 mm. The first conceptual design of the new vacuum section and the cryogenic drift cell for the AIMS setup is described in Ref. [45]. The originally used miniature ion guide in the differential pumping section (see Sec. 7.3) is replaced by a buncher, a cryogenic drift cell, and a short QuadruPole Ion Guide (QPIG). Instead of a differential pumping section with different turbomolecular pumps, only one section evacuated by one Edwards turbomolecular pump (STPA1603C) is inserted between the drift cell and the QMF. The first draft was revised, the new AIMS setup is schematically shown in Fig. 5.5.

In the new setup, the ions are guided from the nozzle exit to the cryogenic drift cell by a buncher. This radiofrequency quadrupole ion guide is 16.38 cm long. An axial trapping for bunching is enabled by individual control of the segments' DC voltage. The cryogenic drift cell consists of 24 drift electrodes enclosed by two electrically isolated endcaps. The drift cell to be implemented has 14.25 cm inner drift length. The ring electrodes have an inner diameter of 20 mm and a width of 5 mm. The distance between the electrodes is set by ceramic spacers to 0.5 mm. The endcaps are designed as ring electrodes but are closed from one side by a 1 mm thick plate perforated in the center by a 1 mm diameter pinhole. The ring electrodes are fixed on four ceramic holder rods, which on turn are fixed at the endcaps. This holding principle ensures an efficient evacuation of the drift volume and a homogeneous distribution of the cooled buffer gas. The voltage applied on the electrodes is successively scaled down by a resistor chain to enable a homogeneous electric drift field. A picture of the drift cell is shown in Fig. 5.6a.

The cooling of the drift cell down to 100 K is achieved by a cryocooler (CryoTel-CT), which is connected to the drift cell via copper connections. The cooling capacity at 60 K is specified as 30 W at 50 Hz. A 50–100 μm copper coating on the hexagonal cryocell housing, as visible in Fig. 5.6b, enables a uniform cooling of the cell, whereby the gas temperature can be controlled with ± 0.1 K through

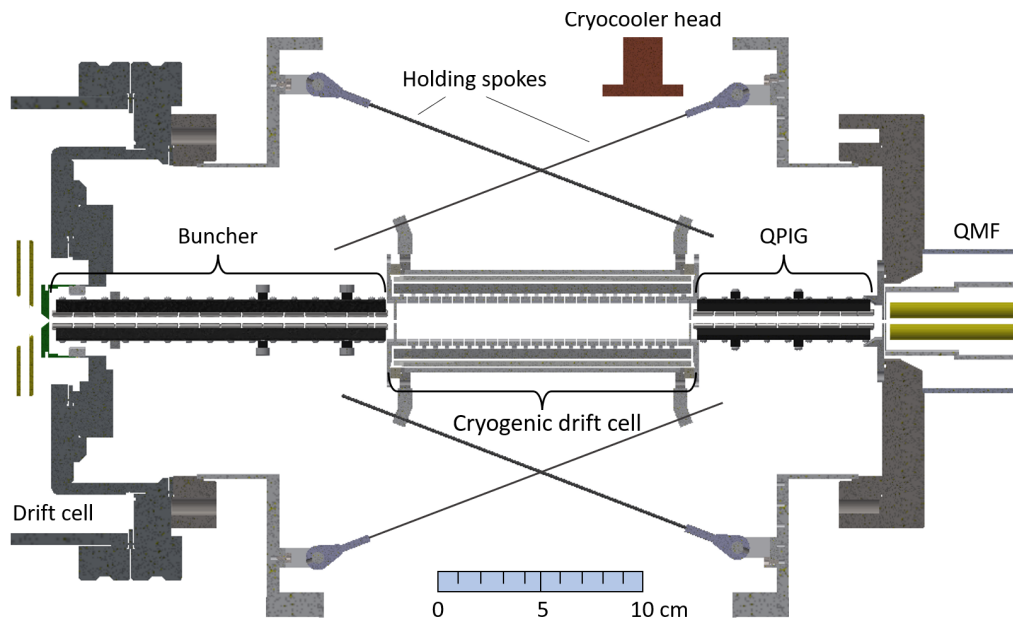


Figure 5.5: Cryogenic drift cell design. The new vacuum section is placed between the drift cell and the QMF. It consists of a buncher, a cryogenic drift cell, and an ion guide. A QMF adapter piece is placed between the cryocell housing and the detector chamber (see Fig. 5.4).

the Proportional-Integral-Derivative controller PID-regulated cryocooler. The gas is injected to the cryogenic drift cell by a Vacuum Coupling Radiation (VCR) gas inlet. The pressure control is obtained by using a needle valve. Finally, a second, 8.84 cm long RF structure guides the ions to the QMF. The electrode segments of buncher and the final QPIG are all fabricated from stainless steel. The electrodes are embedded in peek segment holders, which are mounted on aluminum bars. The opposite segments are connected by Kapton isolated wires, as visible in Fig. 5.6c. Both QPIG and buncher are held by supporting structures fixed at the endcaps of the cryogenic drift cell, see Fig. 5.6b. The cryogenic drift cell is fixed in the outer vacuum chamber, the cryocell housing, by 12 titanium holding spokes (M2, DIN 975 / DIN 976 Titanium Grade 2) [204]. The cryogenic drift cell for the AIMS setup is fabricated by the mechanical workshop and is completely assembled. In summer 2022, it has been already tested for leaks. Buncher and miniature QPIG are assembled and under commissioning. The replacement of the old extraction section is to be implemented soon.

In the current setup, the cryocell housing is already in place between the drift cell and the QMF, as visible in Fig. 5.7. For further details on the current setup, see Sec. 5.5.3.

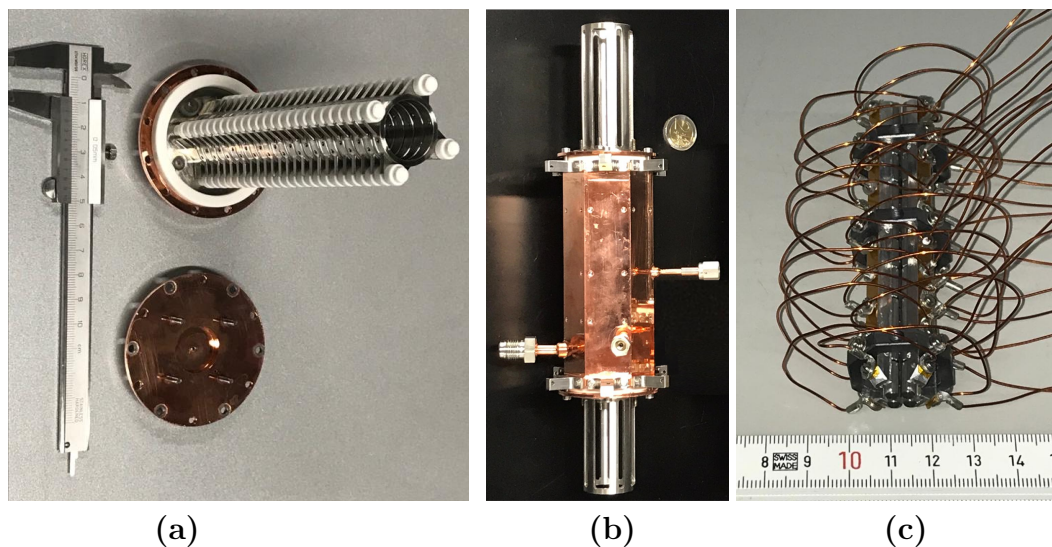


Figure 5.6: Panel (a): Inner structure of the cryogenic drift cell with ring electrodes. Panel (b): Housing of the AIMS cryocell electrodes with VCR inlet for gas supply and copper coating for uniform cooling. Panel (c): New mini QPIG. The opposite segments are connected with Kapton wires.

5.5.2.3 The laser system

The laser system for ionization of the actinides for ion mobility investigations is a combination of a tunable Optical Paramagnetic Oscillator (OPO) pumped by a Nd:YAG laser. The Nd:YAG (Continuum Powerlite Precision II, [230]) provides a fundamental wavelength of 1064 nm. By frequency doubling and tripling 532 nm and 355 nm can be obtained through the use of Second Harmonic Generation (SHG) and Third Harmonic Generation (THG) crystals. SHG and THG crystals enable the self-mixing of the fundamental wave to double or tripple the incoming frequency, respectively. The repetition rate of the Nd:YAG laser is 50 Hz. A maximum pulse energy of 500 mJ and a maximum power of 25 W can be achieved in the infrared, where the pulse length is about 9 ns. As shown in Fig. 5.8, the fundamental 1064 nm and the 355 nm laser beams are coupled in the OPO laser (GWU VisIR2, [231]). The 532 nm laser beam is not used and therefore blocked inside of the Nd:YAG. Inside the OPO laser, a nonlinear OPO crystal is placed in an optical resonator, where the 355 nm pump wave generates a signal and an idler wave and all three waves overlap under phase matching condition [232]. Two different OPO crystals are available for selection to cover a wavelength range between 410–710 nm in total. The range is even expendable by the use of Second Harmonic Generation (SHG) and Sum Frequency Mixing (SFM) crystals. As mentioned above, the SHG crystal allows a frequency doubling by self-mixing of the incoming wave. The SFM crystal enables a mixing of the signal wave from the OPO crystal and the 1064 nm beam from the Nd:YAG.

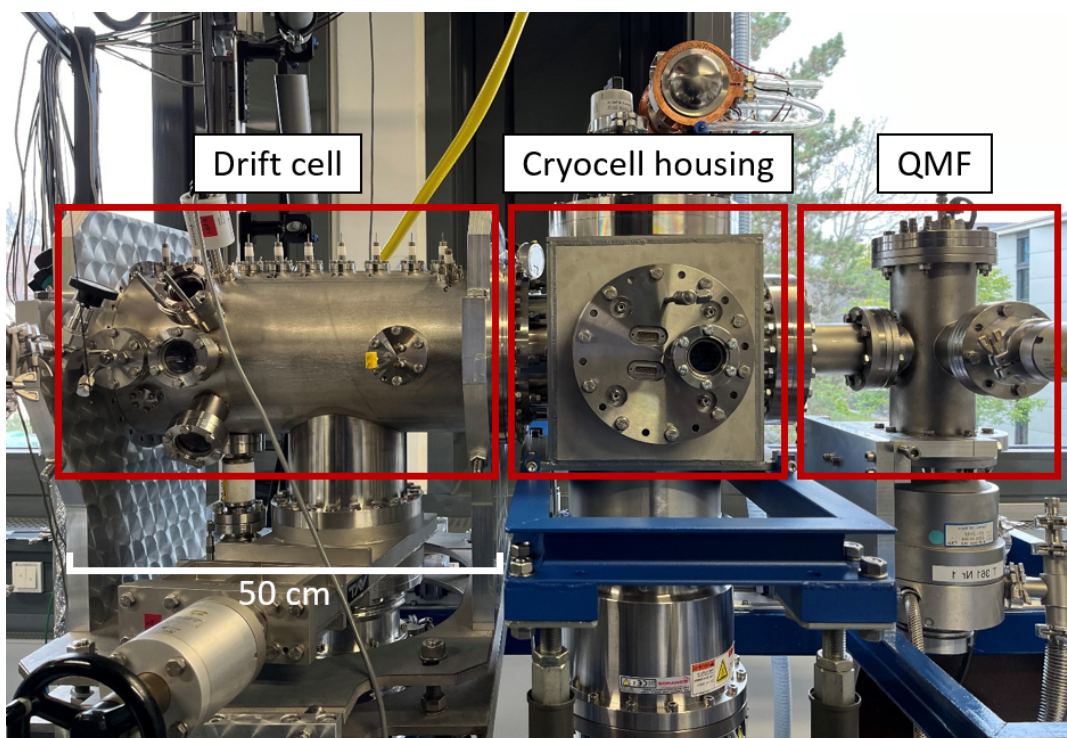


Figure 5.7: Photograph of the AIMS setup. The new vacuum section (cryocell housing) is placed between the drift cell and the QMF. So far, the buncher, the cryogenic drift cell and the QPIG are not yet mounted, but a RFQ ion guide is inserted for first efficiency tests (see Sec. 5.5.3).

A Pellin-Broca-Prism enables the decoupling of the OPO laser beam at wavelengths in the range between 250–710 nm from the other two laser wavelengths. The respective pulse length is 8–10 ns and the maximal power equals to 4 mJ/pulse at the output of the OPO laser. Overall, the bandwidth of OPO laser is about 90 GHz. The tunable laser beam is guided to the cell by an optical multi-mode silica glass fiber of 500 μm core diameter. The 355 nm back reflection from the OPO crystal is coupled back to the Nd:YAG, before being guided to an additional output, from where it can be guided to the drift cell either by a fiber or a set of mirrors. This back reflection is used to provide the non resonant second step for resonant laser ionization. View port windows on the drift cell enable both laser beam coupling and temperature control of the filament utilizing a pyrometer (Lumasense IMPAC IS 6 Advanced Pyrometer). More details on the Nd:YAG-pumped OPO laser system can be found in Ref. [233] and [222].

First tests of the laser system hint towards possible efficiency losses due the bandwidth of the OPO, which may be the limiting factor for ionization of actinides. Due to the broad bandwidth, the excitation to the resonant step might not be efficient enough. Further tests on lanthanide isotopes are planned within the framework of the inauguration of the AIMS apparatus.

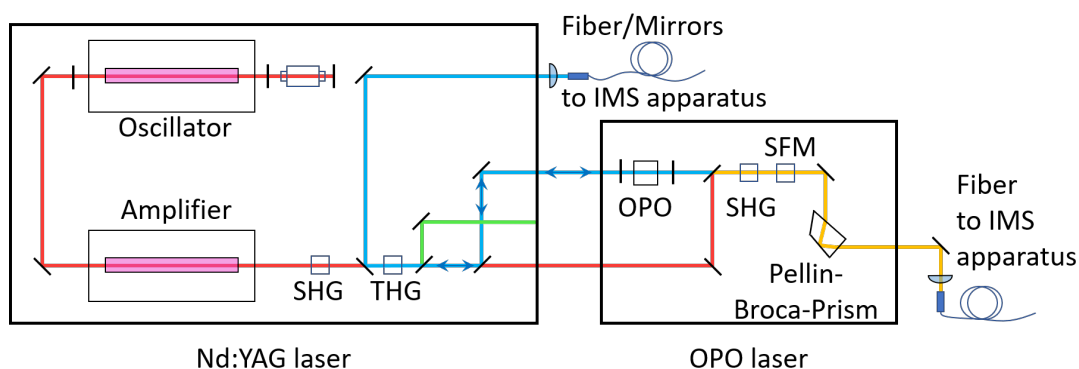


Figure 5.8: Laser setup for IMS measurement, Nd:YAG on the right hand side, OPO fed by Nd:YAG on the left hand side.

5.5.2.4 Data acquisition system

The Data AcQuisition system (DAQ) was developed in Ref. [150] and updated within the M.Sc Thesis of J. Schneider [222] to be compatible with the Windows10 operating system. Within the framework of the LRC project [26], the DAQ is still under development. The main features of the different DAQ system are listed in Tab. 5.2. The control of the DAQ system is obtained by a field-programmable gate array (FPGA based National Instruments, NI PXI 7842R / NI PCIe 7857). The FPGA module enables for reconfigurability of the analog and digital I/O channels.

Feature	Version 2019 [222]	Future Version
Bus type	PXI 7842 R	PCIe 7857
Clock frequency	40 MHz	80 MHz
Digital I/O	96	48
Analog inputs	8 (± 10 V)	8 (± 10 V)
Analog outputs	8 (± 10 V)	8 (± 10 V)
I/O resolution	16 bits	16 bits
Sampling rate	200 kS/s/channel	1 MS/s/channel
Operating system	Windows 10 (64 bit)	Windows 10
DAQ software	LabVIEW 2019	LabVIEW 2019

Table 5.2: DAQ key features

In the current version, the DAQ system provides both experiment control and data recording. Start and stop of the mass and laser scans are implemented in a dedicated LabVIEW program. Moreover, spectra plotting, data saving and control of the Nd:YAG as well as the OPO lasers are achieved by the DAQ [222]. The current software enables an individual control of the voltage settings for

the drift cage, the filament, the new QPIG and the QMF all together (see Sec. 5.5.2.5).

The measurement start time is defined by the laser pulse, which is triggered by a TLL pulse from the DAQ system. When an ion hits the channeltron multiplier surface, it produces a negative detector signal. The signal is amplified and shaped using a spectroscopy amplifier (Ortec 451), then converted by a constant fraction discriminator (Ortec 584) to a digital signal, which determines the time stamp of the recorded event. As a future development, the buffer gas pressure inside the drift cell during mobility measurements will be monitored, too. Further details on the signal processing are explained in Ref. [150] and [222].

5.5.2.5 Voltage settings

The voltage settings for the drift cage, the filament and the QPIG are set by a CAEN SY5527 module, which enables the control of 4x12 positive and 1x12 negative channels (positive: +S/N 0501, 0468, 0471, 0523, negative: -PID 15742). For the systematic measurements on lanthanides and the recommissioning of the ion mobility spectrometer, the voltage settings of [150] were applied.

The voltage settings for the drift cage were firstly obtained by electric field calculations [150] and used for recommissioning measurements in Ref. [222]. Now, a LabVIEW program enables for direct control and surveillance of the voltage and current settings, such that the potential settings can be varied quickly upon request. For the current inauguration experiments, a voltage setting has been chosen to give a mean drift field of ~ 18 V/cm.

The voltage control of the segments of the new QPIG, as described in Sec. 5.5.2.2, is achieved by in the positive modules +S/N 0501, +S/N 0468, +S/N 0471 and +S/N 0523 in the CAEN SY5527, such that each of the segments of the new QPIG can be addressed separately in the developed LabVIEW program. This enabled to substitute a resistor chain used in Ref. [150] to set homogenous electric fields of the QPIG.

The negative voltages of the QMF, the 90° deflector parts and the focusing electrodes Dia₁ and Dia₂ are provided by the negative module -PID 15742 in the CAEN SY5527. In Tab. 5.3, the used voltages are listed.

A CAEN HV Power Supply (Model N1470) provides a bias voltage of -2 kV for the channeltron and +180 V for the detector plate.

5.5.3 Interim status of AIMS

First test experiments were carried out to test differential pumping performances in the different sections of the apparatus. Instead of the cryocell setup with miniature buncher, the cryogenic drift cell and the mini QPIG, a 37.8 cm long RF quadrupole with 24 segments is inserted in the cryocell housing to bridge the distance between the nozzle exit and the QMF start. The segment diameter of

5 *The development of an Actinide Ion Mobility Spectrometer*

Electrode	22	21	20	19	18	Filament	17	16	15	14
Voltage [V]	1026	1026	1026	1026	942	954	918	888	858	828
Electrode	13	12	11	10	9	8	7	6	5	4
Voltage [V]	798	768	732	696	660	618	576	528	468	408
Electrode	3	2	1	Nozzle		QMF	90° _{out}	Dia ₁	90° _{in}	Dia ₂
Voltage [V]	342	264	180	126		-26.2	-30.8	-70.5	-116.2	-204.5

Table 5.3: Caen SY5527 Voltage Settings.

this RFQ ion guide is 11 mm. A picture of the buncher is given in Fig. 5.9. The RFQ is placed in the cryocell housing, as depicted in Fig. 5.10.

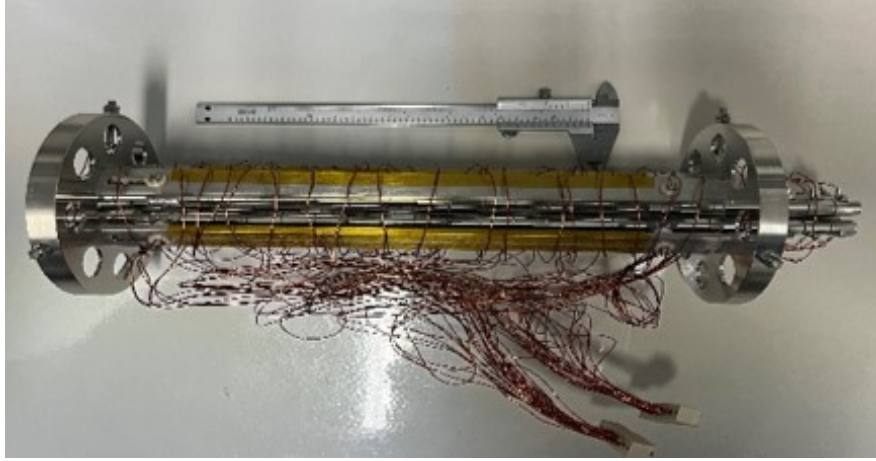


Figure 5.9: Photo of the RFQ buncher inserted in the cryocell housing for the interim status of AIMS. A schematic drawing with inserted RFQ is given in Fig. 5.10.

To allow for an efficient pressure reduction from the drift cell towards the detection section, the vacuum system of the ion mobility spectrometer was revised. The drift chamber and the detection section are evacuated by TurboMolecular Pumps (TMPs) of the same model (Edwards, EXT225H), which can reach a pumping speed of up to 400 l/s for nitrogen. The cryocell housing is connected to the TMP Edwards STPA1603C, which reaches pumping speeds of up to 1200 l/s for helium. The TMPs are connected to dry pumps, whereby the TMPs of drift chamber and the detection section are coupled to Edwards iXL600 with an average speed of 600 m³/h. The TMP below the cryocell housing is connected to the Edwards XDS35i scroll pump.

A schematic picture of the new vacuum pumping system is given in Fig. 5.11. With the new vacuum system, a leak test attested ultimate pressures of $1.4 \cdot 10^{-7}$ mbar for the drift cell, $3.2 \cdot 10^{-8}$ mbar for the cryocell housing and $3.9 \cdot 10^{-7}$

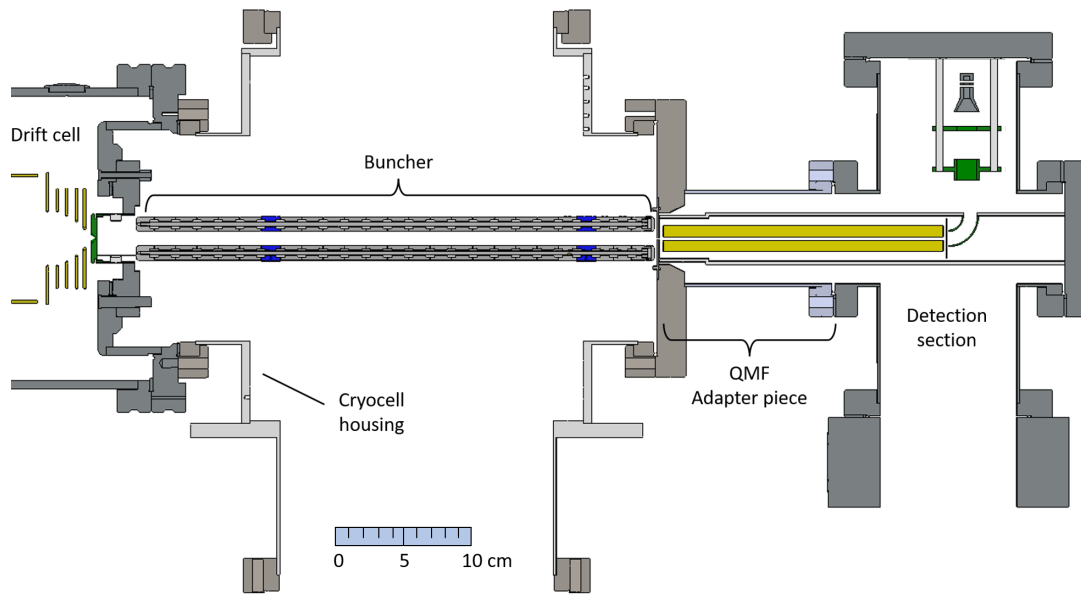


Figure 5.10: Interim status of AIMS before the implementation of the cryogenic drift cell design. The detection section is described in more detail in Fig. 5.4.

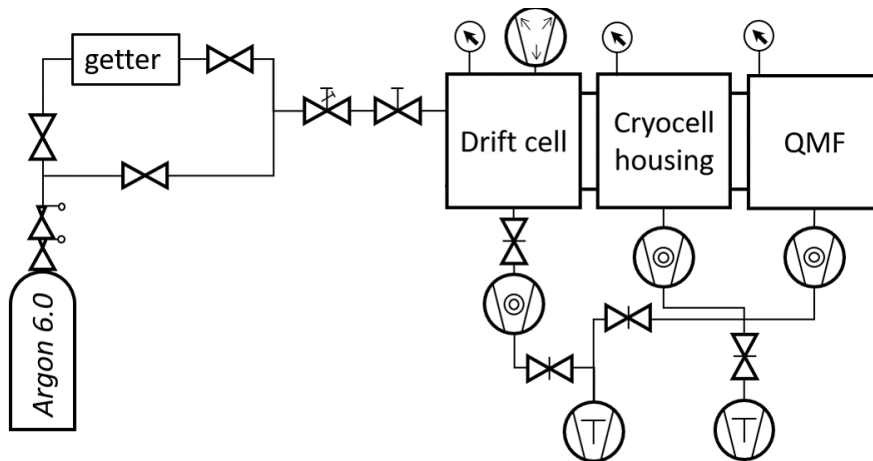


Figure 5.11: Vacuum system of the AIMS apparatus, adapted from Ref. [150]. The final vacuum system may vary slightly from the interim status depicted here. The characteristics of the TMPs and dry pumps are specified in the text above.

mbar for the detection section. The leakage rate was better than $7 \cdot 10^{-8}$ mbar·l/s. A test of the gas control system when utilizing a 1 mm diameter nozzle showed that an argon flow rate of 5.0 mbar·l/s is appropriate to reach a pressure of 40 mbar in the drift cell. The new vacuum system leads to a final pressure of $5.5 \cdot 10^{-3}$ mbar in the cryocell housing and $2.4 \cdot 10^{-5}$ mbar in the detection section, respectively. This allows both for a required cooling of the extracted ions in the RFQ and for the proper operation of the QMF.

The next steps towards an operation in the interim status are efficiency measure-

ments of both the drift cell and the RFQ in the cryocell housing. Hereby, the extraction efficiency of the drift cell should amount to at least 35% with the 1 mm diameter nozzle to ensure similar performance as before [150].

5.6 Possible isotopes for drift measurements

For ion mobility studies in the actinides, trace amounts of long lived radioisotopes will be used. Particularly the region between $Z = 94$ and $Z = 98$ is interesting due to expected distinct electronic configurations of the ionic species (see Sec. 5.2). For off-line experiments, $^{242}_{94}\text{Pu}$, $^{243}_{95}\text{Am}$, $^{245}_{96}\text{Cm}$, $^{248}_{96}\text{Cm}$, $^{249}_{97}\text{Bk}$ and $^{249}_{98}\text{Cf}$ are produced in a macroscopic scale of several picograms through long-term breeding in nuclear reactors such as the research reactor High Flux Isotope Reactor HFIR at Oak Ridge, TN, USA. The samples are put on filaments through electrochemical deposition [234]. For this procedure, the actinides are deposited as 25–50 μm layers of element hydroxides on carrier foils, usually tantalum, and finally covered by a 1–2 μm thin passivating layer of titanium. The production of off-line actinide samples has been successively established [235]. A new approach for sample production is given by the drop-on-demand technique. Here, the sample in solution is dispensed in drops with volumes down to 5 nL to a substrate of choice. This enables variable sample geometry, the usage of non-metal backing foils and chemically pure preparation [236]. An overview on possible isotopes that can be taken for future IMS measurements is given in Tab. 5.4.

Isotope	$t_{1/2}$	Main decay	Max. activity	Max. amount	Order
$^{242}_{94}\text{Pu}$	$3.75 \cdot 10^5 \text{ y}$	$\alpha \xrightarrow{100\%} ^{238}_{92}\text{U}$	10^6 Bq	$1.7 \cdot 10^{19} \text{ atoms}$	1
$^{241}_{95}\text{Am}$	432.6 y	$\alpha \xrightarrow{100\%} ^{237}_{93}\text{Np}$	10^5 Bq	$1.9 \cdot 10^{16} \text{ atoms}$	3b
$^{243}_{95}\text{Am}$	7364 y	$\alpha \xrightarrow{100\%} ^{239}_{93}\text{Np}$	10^5 Bq	$3.3 \cdot 10^{16} \text{ atoms}$	3a
$^{245}_{96}\text{Cm}$	8423 y	$\alpha \xrightarrow{100\%} ^{241}_{94}\text{Pu}$	10^5 Bq	$3.8 \cdot 10^{16} \text{ atoms}$	2b
$^{248}_{96}\text{Cm}$	$3.48 \cdot 10^5 \text{ y}$	$\alpha \xrightarrow{91.61\%} ^{244}_{94}\text{Pu}$	10^5 Bq	$1.6 \cdot 10^{18} \text{ atoms}$	2a
$^{249}_{97}\text{Bk}$	330 d	$\beta^- \xrightarrow{99.998\%} ^{249}_{98}\text{Cf}$	10^8 Bq	$4.1 \cdot 10^{15} \text{ atoms}$	5
$^{249}_{98}\text{Cf}$	351 y	$\alpha \xrightarrow{100\%} ^{245}_{96}\text{Cm}$	10^8 Bq	$1.6 \cdot 10^{18} \text{ atoms}$	4b
$^{251}_{98}\text{Cf}$	898 y	$\alpha \xrightarrow{100\%} ^{247}_{96}\text{Cm}$	10^5 Bq	$4.1 \cdot 10^{15} \text{ atoms}$	4a

Table 5.4: Possible isotopes for AIMS. The suggested order for AIMS studies is given by the decay path of the studied actinides and the allowed sample amount.

The suggested order of ions for mobility studies is based on the half-life of the selected isotopes to avoid contamination as far as possible. The first actinide for AIMS investigations should therefore be $^{242}_{94}\text{Pu}$, which is the most long-lived isotope of the suggested candidates and decays by α -decay to $^{238}_{92}\text{U}$. Moreover,

5 The development of an Actinide Ion Mobility Spectrometer

the allowed sample size should be more than sufficient to perform mobility measurements even with limited efficiency. However, the sample size should be as low as possible to reduce the handled activity. In preparation for the reduction of the sample size, systematic efficiency tests are foreseen with limited sample amounts of stable lanthanide isotopes after the assembly of the AIMS setup. As second actinide species, curium can be studied. Typically, nowadays HFIR uses curium targets as a start for the production of heavier nuclides, mainly $^{248}_{96}\text{Cm}$, from which gram quantities are available. Alternatively, the more short lived $^{245}_{96}\text{Cm}$ might be used. After curium, the longest lived americium isotope $^{243}_{95}\text{Am}$ is foreseen for mobility studies with AIMS, whereby the isotope $^{241}_{95}\text{Am}$ could be used alternatively. For the choice of californium isotope between $^{249}_{98}\text{Cf}$ and $^{251}_{98}\text{Cf}$, the breeding path might prefer $^{249}_{98}\text{Cf}$, which allows moreover a larger manageable activity. $^{251}_{98}\text{Cf}$ is hereby usually obtained from old californium sources and therefore rather rare. Finally, $^{249}_{97}\text{Bk}$ can be used, which is the only berkelium isotope that can be provided in amounts of $\geq 10^{14}$ atoms. This isotope is regularly produced by β^- decay of $^{249}_{97}\text{Cm}$ in the breeding path. Due to the short half-life of $^{249}_{97}\text{Bk}$ ($t_{1/2} = 330$ d), the contamination of the spectrometer will not be negligible after this series of mobility studies anymore.

In the off-line application, the atoms have to be ionized by suitable excitation schemes. Possible first steps for the excitation schemes of these elements have been tabulated in Ref. [150], and are summarized here in the appendix 7.4 in Tab. 7.3 and 7.4 in the OPO range between 250–710 nm.

In the on-line application of AIMS, even heavier actinides and even transactinides can be examined after being produced by an on-line facility like SHIP at GSI (see Sec. 2.4.3). Hereby, the actinides produced from fusion reactions are initially multiply charged. During thermalization in the argon buffer gas cell, mostly singly charged ions remain, which drift through the drift cell enabling a measurement of the ion mobility. However, the efficiency of extracting and guiding of the ions towards the detector becomes crucial, such that the efficiency determination for the new AIMS setup will be the first task to be tackled after the assembly.

6 Summary and outlook

Both resonance ionization spectroscopy and ion mobility spectrometry are powerful methods to investigate the atomic structure of heavy and potentially superheavy elements. In this thesis, the main focus was on the spectroscopic investigation of $^{248,249,250}\text{Fm}$. In combination with data from $^{255,257}\text{Fm}$, the change in mean-squared charge radii around the deformed shell gap at $N=152$ was extracted, which is in good agreement with all considered theoretical models. To gain more knowledge on the change in mean-squared charge radii around the deformed shell gap at $N=152$, the investigation of further isotopes is essential. The study of additional fermium isotopes, as described in Sec. 3.4, is hereby the next step. An extension of fermium isotope shift studies to combine the results of ^{245}Fm , ^{246}Fm , ^{248}Fm , ^{249}Fm , ^{250}Fm , ^{254}Fm , ^{255}Fm and ^{257}Fm is in preparation [187]. The study of ^{252}Fm would be very clarifying to assess the influence of the $N=152$ shell gap on the mean-square charge radii, but requires further advancing of detection methods. For even further investigation on especially odd- A fermium isotopes, the spectroscopic resolution should be sufficient to resolve the hyperfine structure. The study of other transitions with a larger splitting could help to extract the hyperfine structure. So far, seven transitions are reported, which can be used for isotope shift studies [166].

For high-resolution spectroscopy, one possibility is the use of the JetRIS setup, which combines the RADRIS technique with laser spectroscopy in a gas-jet [160]. Hereby, heavy ions are thermalized in a buffer gas cell and guided by a DC gradient to a filament. After neutralization and subsequent desorption from the filament, the sample atoms follow the gas flow to an extraction nozzle. This de Laval nozzle creates a hypersonic gas-jet, which provides a low temperature (<50 K) and low pressure ($\approx 10^{-1} - 10^{-2}$ mbar) conditions for high-resolution laser spectroscopy. The collisional broadening and the Doppler broadening are significantly reduced, such that a spectral resolution of a few hundred MHz is in reach [160]. With the JetRIS technique, high-resolution spectroscopy studies on ^{253}No are planned at the GSI in Darmstadt. For spectroscopy on ^{254}No , a spectral resolution of 800 MHz have been achieved [237]. Further spectroscopy on odd- A fermium isotopes is therefore possible with JetRIS and may improve the accuracy of the extracted hyperfine parameters.

Other future avenues would be spectroscopy studies on the nobelium isotope ^{255}No to extend laser spectroscopy on the nobelium isotopic chain across the $N=152$ shell gap, which has already been performed in broadband mode with the RADRIS technique [187]. ^{255}No ($t_{1/2} = 3.1$ min) was produced by exploiting the 0.3% electron-capture branch of ^{255}Lr ($t_{1/2} = 31.1$ s) instead of using the

6 Summary and outlook

direct fusion-evaporation reaction $^{208}\text{Pb}(^{48}\text{Ca},n)^{255}\text{No}$. Moreover, the isotope ^{251}No ($t_{1/2} = 0.8$ s) is accessible for laser spectroscopy, which was proven for the first time during a RADRIS beamtime in 2022. The reaction cross section is about 30 nb for the reaction $^{206}\text{Pb}(^{48}\text{Ca},3n)^{251}\text{No}$ [191]. Further neutron rich nobelium isotopes, such as ^{256}No , can be produced by nucleon transfer reactions. High resolution spectroscopy on the californium isotopes $^{249-252}\text{Cf}$ has been performed in a hot cavity at the RISIKO separator of the Johannes Gutenberg-University (see Sec. 3.0.1, [163]). However, input from atomic calculations is still needed to extract the field shift constant F and subsequently the change in the mean-squared charge radii.

For lawrencium ($Z=103$), the search for atomic transitions is still ongoing. Since the isotope ^{255}Lr ($t_{1/2} = 31.1$ s) features the highest production cross section (≈ 400 nb for the reaction $^{209}\text{Bi}(^{48}\text{Ca},2n)^{255}\text{Lr}$ [238]), it is used for the atomic level search. Two atomic ground-state transitions predicted by theory calculations are hereby especially promising, the one leading to the $^2S_{1/2}$ state and the other one leading to the $^2D_{3/2}$ state, which feature a transition amplitude of a few 10^7 s $^{-1}$. Originally, Fock Space Coupled Cluster (FSCC) calculations predicted the states at 20.118 cm $^{-1}$ or 20.131 cm $^{-1}$ and 28.118 cm $^{-1}$ or 28.096 cm $^{-1}$, respectively [239]. More recent coupled cluster calculations locate the transitions at 20.485 cm $^{-1}$ and respectively at 28.580 cm $^{-1}$ [240]. Configuration Interaction (CI) coupled cluster calculations predict transitions at 20.253 cm $^{-1}$ and 28.320 cm $^{-1}$ [241]. Multi-Configuration Dirac-Fock (MCDF) calculations result in the positions 20.053 cm $^{-1}$ and 20.405 cm $^{-1}$ for the $^2S_{1/2}$ state and 28.312 cm $^{-1}$ for the $^2D_{3/2}$ state [242]. To enable an efficient collection and subsequent desorption, which is crucial for a level search at an expected low ion production rate of about 1 ion/s, filament studies have been performed indicating the suitability of pure hafnium filaments [143]. During the RADRIS beamtimes in 2020 and 2022, a wavenumber range of ≈ 1500 cm $^{-1}$ has been scanned for the level search by a two-step excitation scheme. Two dye lasers are simultaneously scanned to provide the first step. One laser covered hereby the wavelength range of 19.700 cm $^{-1} \leq \bar{\nu}_1 \leq 21.000$ cm $^{-1}$, aiming for the transition to the $^2S_{1/2}$ state, the other between 27.500 cm $^{-1} \leq \bar{\nu}_1 \leq 28.750$ cm $^{-1}$ for the $^2D_{3/2}$ state [127]. The non-resonant second step is provided by an excimer laser at 490 nm. Due to an increased detector sensitivity by increasing the solid angle coverage for α -decay detection [168], level search during the RADRIS beamtime in 2022 could scan a wavelength range of > 600 cm $^{-1}$ with a high confidence. The uncertainty of atomic theory predictions is hereby assumed to be about 300 cm $^{-1}$. The search for atomic transitions in lawrencium will therefore continue in the next RADRIS beamtimes.

The second focus of this thesis was on the development of an actinide ion mobility spectrometer, that should enable systematic studies of interaction potentials of actinide ions drifting in neutral gases. IMS studies can provide benchmark data for *ab-initio* calculations and may enable the assignment of ion mobilities to

6 Summary and outlook

certain electronic configurations, which in turn can be exploited for distinguishing between different ion species and different states of the same species. The spectrometer described in Ref. [150] was adapted for mobility measurements on actinide ions. Therefore, a cryogenic drift cell was developed to enable systematic mobility studies of different actinide ions at various gas pressures and temperatures.

Since the resonance ionization spectroscopy is only applicable to neutral atoms, the RIS method may not be suitable for superheavy elements, which belong to the refractory transition metals [26]. A novel way of laser spectroscopy, which is in preparation to be applied to Lr^+ , may be the Laser Resonance Chromatography technique (LRC) [26]. LRC enables probing the ion state by detecting the difference in mobility between products extracted from gas catchers and their resonantly pumped meta-stable states [204]. Neutralization of thermalized ions as needed for resonance ionization spectroscopy can be obviated by this implementation of optical spectroscopy, such that more short-lived isotopes are accessible. To avoid quenching, only short drift tubes filled with <10 mbar helium gas are foreseen. By coupling laser spectroscopy with ion mobility spectrometry, LRC enables an alternative approach for atomic level search and subsequent high-resolution spectroscopy studies. The LRC setup is currently nearly complete [204] and commissioning experiments are ongoing. To investigate superheavy elements with the LRC technique, *ab-initio* calculations are necessary to predict excited states to be searched for and the low-lying metastable states, which are suitable for optical pumping. For singly charged rutherfordium ($Z=104$), results from MRCI calculations were recently reported, suggesting two possible pumping schemes for this superheavy element cation [243]. For LRC investigation of even heavier elements, further calculations are needed. Mobility studies can thus provide an alternative access for element identification and characterization of heavy and superheavy elements.

7 Appendix

7.1 Gate setting for Fm spectroscopy

The α spectra of the events registered by the PIPS detector can be modeled with a convolution of a Gaussian and a weighted sum of two left-sided exponentials, such that the fit function for the spectrum is given by $f(x) = \frac{1}{2\tau} \exp\left(\frac{x-x_c}{\tau} + \frac{\sigma^2}{2\tau^2}\right) \operatorname{erfc}\left[\frac{1}{\sqrt{2}}\left(\frac{x-x_c}{\sigma} + \frac{\sigma}{\tau}\right)\right]$ [244]. τ is a parameter to describe the left sided exponential, x_c is the center of the Gaussian, σ is the standard variation of the normalized Gaussian and erfc is a complementary error function. A picture of the fitted spectra and the respective gates for ^{250}Fm resonance ionization spectroscopy is given in Fig. 7.1. The upper gate is given by the 3σ interval of the Gaussian. The lower gate is set at $1/12$ of the maximal height of the fitted α spectrum. A table of the chosen gates is given in Tab. 7.1.

Reaction	$E_{\alpha, No}$	$E_{\alpha, Fm}$	Lower gate	Upper gate
$^{254}_{102}\text{No} \xrightarrow{\alpha} ^{250}_{100}\text{Fm}$	8.093 MeV	7.43 MeV	7.135 MeV	7.535 MeV
$^{253}_{102}\text{No} \xrightarrow{\alpha} ^{249}_{100}\text{Fm}$	8.01 MeV	7.527 MeV	7.23 MeV	7.60 MeV
$^{252}_{102}\text{No} \xrightarrow{\alpha} ^{248}_{100}\text{Fm}$	8.415 MeV	7.87 MeV	7.47 MeV	7.93 MeV

Table 7.1: Gates for Fm isotopes

The influence of a change of the gates to, e.g., 4σ and $1/10$ of the height amount to less than 10% of the stated uncertainty (see Sec. 3.2.1). In Fig. 7.1, the respective gates for ^{250}Fm are shown. When α events are registered in these gates, they are taken into account for the RIS scan.

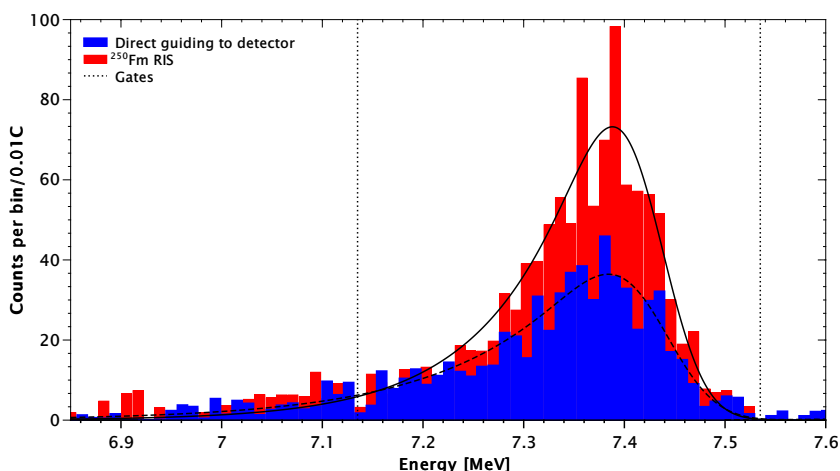


Figure 7.1: α spectra of ^{250}Fm with set gates

7.2 Spherical FRDM parametrization for modeling $\delta\langle r^2 \rangle$

The spherical Finite Range Droplet Model differs from the Liquid Drop Model due to the definition and use of equivalent radii of proton and neutron distribution and due to the consideration of mass redistribution due to the Coulomb force [179]. The parametrization from [179] is used. To construct the equivalent radii R_N and R_Z , the radius definition from the Liquid Drop Model is extended by the parameter ε :

$$R = r_0 A^{1/3} (1 + \varepsilon) . \quad (7.1)$$

The parameter ε is defined by

$$\varepsilon = (-2a_2 A^{-1/3} B_S + L\delta^2 + c_1 Z^2 A^{-4/3} B_C) / K \quad (7.2)$$

with

$$\delta = \frac{I + \frac{3}{16}(c_1/Q)ZA^{-2/3}B_V}{1 + \frac{9}{4}(J/Q)A^{-1/3}B_S} \quad \text{and} \quad I = (N - Z)/A . \quad (7.3)$$

ε consists of several terms, which take the surface energy a_2 , the density symmetry L and the Coulomb energy c_1 into account. K is the compressibility coefficient, J is the asymmetry coefficient and Q is the surface stiffness, which governs the neutron skin thickness of the nucleus [178]. The parameters B_S , B_C and B_V , which consider the deformation on the surface, variations of the Coulomb potential and the volume change due to the Coulomb potential variation, respectively, can be set to zero for a spherical nucleus. The equivalent radii R_N and R_Z are given by

$$R_N = R + \frac{Z}{A}t \quad \text{and} \quad R_Z = R - \frac{N}{A}t \quad (7.4)$$

7 Appendix

with $t = \frac{2}{3}R(I - \delta)$ for spherical nuclei. The change in the proton distribution, which is given by

$$C' = \frac{1}{2} \left(\frac{9}{2K} + \frac{1}{4J} \right) \frac{Ze^2}{R_Z}, \quad (7.5)$$

is also needed for the computation of the mean square charge radius $\langle r^2 \rangle$. It is calculated by

$$\langle r^2 \rangle = \langle r^2 \rangle_u + \langle r^2 \rangle_r + \langle r^2 \rangle_d \quad (7.6)$$

with $\langle r^2 \rangle_u = \frac{3}{5}R^2$, $\langle r^2 \rangle_r = \frac{12}{175}C'R^2$ and $\langle r^2 \rangle_d = 3b^2$ to account for the contribution from the size of the uniform distribution, the redistribution and the diffuseness. The change in mscr $\delta\langle r^2 \rangle_{\text{sph}}$ is calculated in relation to the reference isotope. The used parameters are mainly extracted from a parametrization in Ref. [178] and listed in Tab. 7.2.

r_0 [fm]	b [fm]	a_2 [MeV]	J [MeV]	Q [MeV]	K [MeV]	L [MeV]
1.18	1.02	23	29.5	45	240	-35

Table 7.2: FRDM parametrization for computation of $\delta\langle r^2 \rangle_{\text{sph}}$ from [178]

The Coulomb parameter $c_1 = \frac{3e^2}{5r_0}$ amounts with $r_0 = 1.18$ fm to $c_1 \approx 0.7465$ MeV. r_0 is hereby the only value taken from the parametrization used in Ref. [179], instead of calculating it back from the definition given in Ref. [178] $\rho_\infty = 3/(4\pi r_0^3) = 0.154$ fm⁻³. The diffuseness is chosen to $b = 1.02$ fm, which fits better for heavier nuclei [178].

7.3 Old IMS detection section

After the extraction through the nozzle, the ions have to be guided to the detector. This was in the old setup [150] done in a differential pumping section by using a miniature radio frequency quadrupole ion guide (QPIG), a Quadrupole Mass Filter (QMF) and a 90° deflector, which are briefly described here. A schematic overview of the setup is given in Fig. 7.2.

Since the QPIG was placed about 1 mm behind the nozzle, the thermal energy of the extracted ions is efficiently reduced by gas cooling. The pressure in the first segment of the differential pumping section was $< 5 \cdot 10^{-2}$ mbar. The ions are consequently centered in the QPIG, such that the emittance was quite small [245]. The ion guide follows the design of a Paul trap. Its working principle is described in detail in Ref. [246], [247] and [248]. The necessary preliminary considerations are given in Ref. [150]. In a segmented quadrupole geometry, a radio frequency (RF) voltage is applied to the opposite rod pairs, whereby the neighboring electrodes are 180° out of phase. A DC gradient is applied to the

28 segments, such that overall, a centering and guiding of the sample ions is achieved. With the QPIG, a distance of 38 cm is bridged between the nozzle and the QMF, such that the ions are guided through four differential pumping sections. The segment length hereby decreases from 15, to 12.5 to 10 mm, while the last segment is 50 mm long. The RF frequency is set to 1.95 MHz to be in consistence with the RF frequency of the QMF. The differential pumping section and the used turbomolecular pumps are described in Ref. [150], details on the mass filter and the channeltron can be found in Ref. [249], [250] and [136].

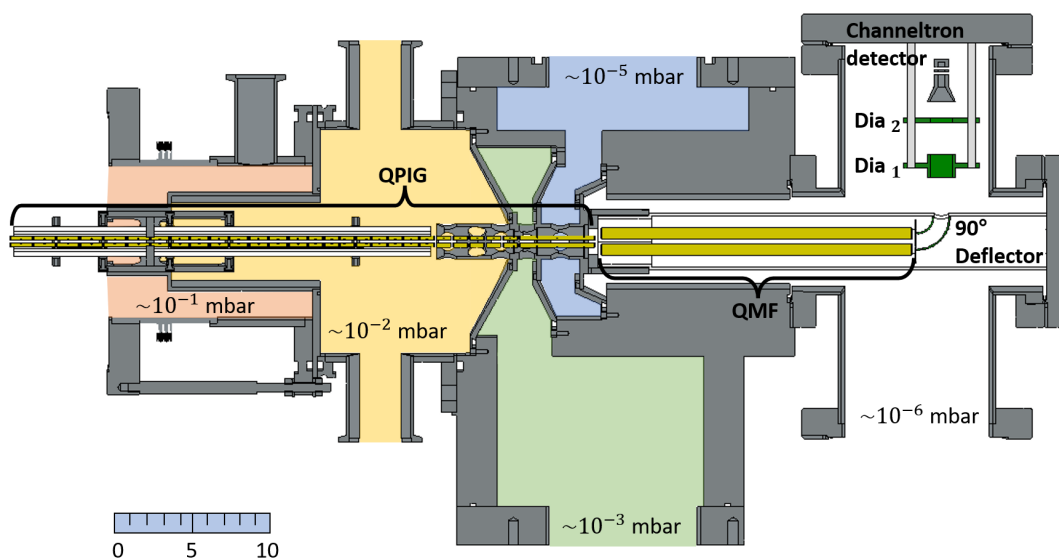


Figure 7.2: IMS Detection part. The QPIG is placed 1 mm behind the nozzle. It bridges 4 differential pumping sections till arriving to the detection section. The ions are selected by the mass filter, which is operated in the last section at $< 10^{-5}$ mbar. The detection is archived with a channel electron detector.

7.4 Excitation states for selected actinides ($Z=92-100$)

In the AIMS setup, the ionization of the actinide of choice is obtained by an excitation of the sample atoms by the OPO laser in a first resonant excitation step followed by a subsequent non-resonant excitation to continuum by the 355 nm laser beam of the Nd:YAG (see Sec.5.5.2.3). Since the OPO can cover a wavelength range between 250–710 nm, possible excitation steps are noted down in Tab. 7.3 and 7.4 for $Z = 92 - 95$ and $Z = 96 - 100$, respectively.

7 Appendix

Element	Configuration	Term	J	λ_{12} [Å]	$\bar{\nu}_{12}$ [cm ⁻¹]	
⁹² U I	$5f^36d7s^2$	$^5L^\circ$	6		0	
	$5f^36d7s7p$	7L	7	4362.051	22918.553	
			7	4153.971	24066.566	
			6	3943.8161	25348.977	
			6	3871.0353	25825.565	
			6	3811.9911	26225.569	
	$5f^36d^27p$	7N	7	3584.8774	27886.995	
			5	3561.8038	28067.646	
			5	3561.8038	2844.517	
5			3489.3672	28650.294		
⁹² U II	$5f^36d7s$	$^4I_{9/2}^\circ$			49958.4	
⁹³ Np I	$5f^46d7s^2$	6L	11/2		0	
	$5f^46d7s7p$	$^8M^\circ$	11/2	6972.09	14338.88	
	$5f^46d7s7p$	$^6M^\circ$	13/2	5878.04	17007.70	
			◦	13/2	3986.89	25075.145
			◦	13/2	3501.50	28551.035
			◦	13/2	3481.93	28711.465
⁹³ Np II	$5f^46d7s$	7L_5			50536	
⁹⁴ Pu I	$5f^67s^2$	7F	0		0	
	$5f^5(^6H^\circ)6d7s^2$	$^7G^\circ$		6488.853	15406.76	
	$5f^5(^6F^\circ)6d7s^2$	$^7G^\circ$		6304.661	15856.888	
			1	4896	20426	
	$5f^57s7p$	$^7D^\circ$	1	4206.481	23766.139	
	$5f^56d^27s$		1	3851.007	25959.849	
	$5f^67s7p$		1	3753.628	26633.288	
⁹⁴ Pu II	$5f^56d7s$	$^8F_{1/2}$			48603	
⁹⁵ Am I	$5f^77s^2$	$^8S^\circ$	7/2		0	
	$5f^77s7p$	$(7/2, 1)$	9/2	6054.64	16511.82	
			7/2	5000.21	19992.16	
				4681.65	21352.99	
	$5f^77s7p$	$(7/2, 2)$	7/2	4662.79	21440.37	
			9/2	4289.258	23307.41	
	$5f^77s7p$	$(7/2, 1)$	5/2	3673.121	27217.14	
	$5f^77s7p$	$(7/2, 1)$	7/2	3569.163	28009.81	
	$5f^77s7p$	$(7/2, 1)$	9/2	3510.127	28480.87	
	⁹⁵ Am II	$5f^77s$	$^9S_{1/2}^\circ$			48182

Table 7.3: Actinide atomic levels $Z=92 - 95$, that radiatively couple to the ground state (first row of each element). Data taken from [251], [150].

7 Appendix

Element	Configuration	Term	J	λ_{12} [Å]	$\bar{\nu}_{12}$ [cm ⁻¹]
⁹⁶ Cm I	$5f^7 6d 7s^2$	$^9D^\circ$	2		0
	$5f^7 6d 7s 7p$	^{11}F	3	6376.71	15677.75
	$5f^7 6d 7s 7p$	9D	2	4330.82	23083.822
	$5f^7 6d 7s 7p$	7D	3	3995.10	25023.578
	$5f^7 6d 7s 7p$	5D	2	3116.411	32078.886
⁹⁶ Cm II	$5f^7 7s^2$	$^8S_{7/2}^\circ$			48324
⁹⁷ Bk I	$5f^9 7s^2$	$^6H^\circ$	15/2		0
	$5f^9 6d 7s 7p$	(15/2, 0)	15/2	5910.71	16913.77
	$5f^9 6d 7s 7p$	(15/2, 1)	17/2	5659.03	17665.98
	$5f^9 6d 7s 7p$	(15/2, 1)	15/2	5212.53	19179.21
	$5f^9 6d 7s 7p$	(15/2, 2)	17/2	4466.457	22382.83
	$5f^9 6d 7s 7p$	(15/2, 2)	15/2	4363.636	22910.225
			15/2	3609.614	27695.87
	$5f^9 6d 7s 7p$	(13/2, 2)	15/2	3442.664	29038.93
	$5f^9 6d 7s 7p$	(13/2, 2)	17/2	3426.951	29172.103
⁹⁷ Bk II	$5f^8 6d 7s$				49989
⁹⁸ Cf I	$5f^{10} 7s^2$	5I	8		0
	$5f^7 6d 7s 7p$	(8, 1) [°]	9	5408.88	18483.06
	$5f^7 6d 7s 7p$	(8, 2) [°]	9	4329.03	23093.355
				3785.61	26408.305
	$5f^{10} 7s 7p$	(8, 1) [°]	9	3598.77	27779.345
	$5f^9 6d 7s^2$	°	8	3352.71	29818.055
		°	3298.14	30311.4	
⁹⁸ Cf II	$5f^{10} 7s$				50665
⁹⁹ Es I	$5f^{11} 7s^2$	$^4I^\circ$	15/2		0
	$5f^{11} 7s 7p$	6I	15/2	5615.51	17803.09
	$5f^{11} 7s 7p$	6I	17/2	5204.40	19209.15
	$5f^{10} 6d 7s^2$	6I	17/2	5161.74	19367.85
	$5f^{10} 6d 7s^2$		13/2	3555.34	28118.65
	$5f^{10} 6d 7s^2$		13/2, 15/2, 17/2	3523.49	28372.78
	$5f^{11} 7s 7p$		13/2	3514.33	28447.02
	$5f^{10} 6d 7s^2$		15/2, 17/2	3498.11	28578.60
	$5f^{11} 7s^2$		15/2, 17/2	3428.48	29159.28
⁹⁹ Es II	$5f^{11} 7s$	$((15/2, 1/2)_8^\circ)$			51800
¹⁰⁰ Fm I	$5f^{12} 7s^2$	$^3H_6^e$			0
	$5f^{12} 7s 7p$	$^5I_6^\circ$		3982.98	25099.80
	$5f^{12} 7s 7p$	$^5G_5^\circ$		3981.08	25111.80
¹⁰⁰ Fm II	$5f^{12} 7s$				52587

Table 7.4: Actinide atomic levels Z=96 – 100, that radiatively couple to the ground state (first row of each element). Data taken from [251], [150].

List of Figures

2.1	Orbital binding energy in non-relativistic calculation and relativistic calculation for ${}_{64}\text{Gd}$ and it's actinide homologue ${}_{96}\text{Cm}$	11
2.2	Nilsson quantum numbers	13
2.3	Nilsson diagram for $N \geq 126$	15
2.4	δ_{2n} values around $N=152$	22
2.5	Predicted ground-state quadrupole deformation	23
2.6	Excitation functions ${}^{208}\text{Pb}({}^{48}\text{Ca}, xn)$	25
2.7	Schematic setup of SHIP	27
2.8	Resonance Ionization Spectroscopy principle	31
2.9	Schematic picture of RADRIS method	33
2.10	Schematic overview of AIMS method	37
3.1	RIS studies in actinides	41
3.2	${}^{255}\text{Fm}$ scan	43
3.3	Technical drawing of the RADRIS cell	45
3.4	α spectra on the PIPS detector for ${}^{250}\text{Fm}$ production	46
3.5	RADRIS cycle	47
3.6	RADRIS laser system	48
3.7	${}^{249}\text{Fm}$ narrowband scan	51
3.8	${}^{248,249,250}\text{Fm}$ scan	52
3.9	${}^{257}\text{Fm}$ scan	53
3.10	$\delta\langle r^2 \rangle$ of ${}^{248,249,250}\text{Fm}$ and ${}^{255,257}\text{Fm}$	58
3.11	Different theoretic models to model the change of mscr $\delta\langle r^2 \rangle$ of ${}^{248,249,250}\text{Fm}$ and ${}^{255,257}\text{Fm}$	60
3.12	$\delta\langle r^2 \rangle$ of ${}^{248,249,250,255,257}\text{Fm}$ and further actinide isotopes	62
3.13	Detector improvement: Rotatable multi-detector setup	63
3.14	Fm isotope production	65
4.1	Mobility limitation of the RADRIS technique	68
5.1	Electronic configuration of lanthanide and actinide ground state and singly charged lanthanide and actinide ions	73
5.2	Drift time measurement of ${}^{255}_{100}\text{Fm}$, ${}^{251}_{98}\text{Cf}$ and ${}^{238}\text{UO}^+$	75
5.3	IMS Drift cell	78
5.4	IMS detection section	80
5.5	Cryogenic drift cell design	82
5.6	Cryogenic drift cell	83

LIST OF FIGURES

5.7	Photograph of the AIMS setup	84
5.8	Laser setup for IMS	85
5.9	Photo of RFQ buncher for interim status	87
5.10	Interim status of AIMS	88
5.11	Vacuum system of the AIMS apparatus	88
7.1	^{250}Fm gate setting	95
7.2	IMS Detection part	97

List of Tables

3.1	No RIS results	40
3.2	Hyperfine parameters for ^{255}Fm , taken from Ref. [44]	44
3.3	RADRIS electrode settings	45
3.4	Isotope shift of $^{248,249,250}\text{Fm}$	51
3.5	Isotope shift of $^{255,257}\text{Fm}$	53
3.6	Uncertainties of the $5f^{12}7s7p$ state resonance for $^{248-250}\text{Fm}$	55
3.7	Isotope shift parameters, taken from Ref. [44]	57
3.8	Isotope shift $^{248,249,250}\text{Fm}$ and $^{255,257}\text{Fm}$	57
5.1	Lanthanide mobility measurements	74
5.2	DAQ key features	85
5.3	Caen SY5527 Voltage Settings	87
5.4	Possible isotopes for AIMS	89
7.1	Gating for Fm spectroscopy	94
7.2	FRDM parametrization for computation of $\delta\langle r^2 \rangle_{\text{sph}}$	96
7.3	Actinide atomic levels $Z=92 - 95$	98
7.4	Actinide atomic levels $Z=96 - 100$	99

Bibliography

- [1] William D. Myers and Wladyslaw J. Swiatecki.
Nuclear masses and deformations.
Nuclear Physics, 81(2):1–60, 1966.
- [2] M. Göppert Mayer.
The shell model.
Science, 3636:999–1006, 1964.
- [3] S Ówiok, P-H Heenen, and Witold Nazarewicz.
Shape coexistence and triaxiality in the superheavy nuclei.
Nature, 433(7027):705–709, 2005.
- [4] S Ówiok, S Hofmann, and W Nazarewicz.
Shell structure of the heaviest elements.
Nuclear Physics A, 573(3):356–394, 1994.
- [5] Meng Wang, WJ Huang, Filip G Kondev, Georges Audi, and Sarah Naimi.
The AME 2020 atomic mass evaluation (II). Tables, graphs and references.
Chinese Physics C, 45(3):030003, 2021.
- [6] Y Nagame and M Hirata.
Production and properties of transuranium elements.
Radiochimica Acta, 99(7-8):377–393, 2011.
- [7] K.P. Santhosh and C. Nithya.
Predictions on the modes of decay of even Z superheavy isotopes within the range $104 \leq Z \leq 136$.
Atomic Data and Nuclear Data Tables, 119:33–98, 2018.
- [8] P Campbell, ID Moore, and MR Pearson.
Laser spectroscopy for nuclear structure physics.
Progress in Particle and Nuclear Physics, 86:127–180, 2016.
- [9] Randolph Pohl, Ronald Gilman, Gerald A Miller, and Krzysztof Pachucki.
Muonic hydrogen and the proton radius puzzle.
arXiv preprint arXiv:1301.0905, 2013.
- [10] Jan C Bernauer and A1 Collaboration.
High-precision determination of the electric and magnetic form factors of the proton.
In *AIP Conference Proceedings*, volume 1388, pages 128–134. American Institute of Physics, 2011.

BIBLIOGRAPHY

- [11] Isao Tanihata, Herve Savajols, and Rituparna Kanungo.
Recent experimental progress in nuclear halo structure studies.
Progress in Particle and Nuclear Physics, 68:215–313, 2013.
- [12] J. M. G. Levins, D. M. Benton, J. Billowes, P. Campbell, T. G. Cooper, P. Dendooven, D. E. Evans, D. H. Forest, I. S. Grant, J. A. R. Griffith, J. Huikari, A. Jokinen, K. Peräjärvi, G. Tungate, G. Yeandle, and J. Äystö.
First on-line laser spectroscopy of radioisotopes of a refractory element.
Phys. Rev. Lett., 82:2476–2479, Mar 1999.
- [13] B. A. Marsh, T. Day Goodacre, S. Sels, Y. Tsunoda, B. Andel, A. N. Andreyev, N. A. Althubiti, D. Atanasov, A. E. Barzakh, J. Billowes, K. Blaum, T. E. Cocolios, J. G. Cubiss, J. Dobaczewski, G. J. Farooq-Smith, D. V. Fedorov, V. N. Fedosseev, K. T. Flanagan, L. P. Gaffney, L. Ghys, M. Huyse, S. Kreim, D. Lunney, K. M. Lynch, V. Manea, Y. Martinez Palenzuela, P. L. Molkanov, T. Otsuka, A. Pastore, M. Rosenbusch, R. E. Rossel, S. Rothe, L. Schweikhard, M. D. Seliverstov, P. Spagnoletti, C. Van Beveren, P. Van Duppen, M. Veinhard, E. Verstraelen, A. Welker, K. Wendt, F. Wienholtz, R. N. Wolf, A. Zadvornaya, and K. Zuber.
Characterization of the shape-staggering effect in mercury nuclei.
Nature Physics, 14(12):1163–1167, 2018.
- [14] John L. Wood and Kristiaan Heyde.
A focus on shape coexistence in nuclei.
Journal of Physics G, 43:020402, 2016.
- [15] Mustapha Laatiaoui, Werner Lauth, Hartmut Backe, Michael Block, Dieter Ackermann, Bradley Cheal, Premaditya Chhetri, Christoph Emanuel Düllmann, Piet van Duppen, Julia Even, Rafael Ferrer, Francesca Giacoppo, Stefan Götz, Fritz Peter Heßberger, Mark Huyse, Oliver Kaleja, Jadambaa Khuyagbaatar, Peter Kunz, Felix Lautenschläger, Andrew Kishor Mistry, Sebastian Raeder, Enrique Minaya Ramirez, Thomas Walther, Calvin Wraith, and Alexander Yakushev.
Atom-at-a-time laser resonance ionization spectroscopy of nobelium.
Nature, 538:495–498, 2016.
- [16] S. Raeder, D. Ackermann, H. Backe, R. Beerwerth, J. C. Berengut, M. Block, A. Borschevsky, B. Cheal, P. Chhetri, Ch. E. Düllmann, V. A. Dzuba, E. Eliav, J. Even, R. Ferrer, V. V. Flambaum, S. Fritzsche, F. Giacoppo, S. Götz, F. P. Heßberger, M. Huyse, U. Kaldor, O. Kaleja, J. Khuyagbaatar, P. Kunz, M. Laatiaoui, F. Lautenschläger, W. Lauth, A. K. Mistry, E. Minaya Ramirez, W. Nazarewicz, S. G. Porsev, M. S. Safronova, U. I. Safronova, B. Schuetrumpf, P. Van Duppen, T. Walther, C. Wraith, and A. Yakushev.
Probing sizes and shapes of nobelium isotopes by laser spectroscopy.

BIBLIOGRAPHY

- Phys. Rev. Lett.*, 120:232503, Jun 2018.
- [17] I. Angeli and K.P. Marinova.
Table of experimental nuclear ground state charge radii: An update.
Atomic Data and Nuclear Data Tables, 99(1):69–95, 2013.
- [18] S. Raeder M. Block, M. Laatiaoui.
Recent progress in laser spectroscopy of the actinides.
Progress in Particle and Nuclear Physics, 116(103834), 2021.
- [19] Sebastian Raeder, Brankica Anelić, Julian Auler, Michael Block, Pierre Chauveau, Premaditya Chhetri, Arno Claessens, Antoine de Roubin, Christoph E. Düllmann, Rafael Ferrer, Francesca Giacoppo, Manuel Guitierrez Torres, Fritz-Peter Heßberger, Fedor Ivandikov, Magdalena Kaja, Oliver Kaleja, Tom Kieck, EunKang Kim, Sandro Kraemer, Mustapha Laatiaoui, Jeremy Lantis, Andrew Mistry, Danny Münzberg, Steven Nothhelfer, Emmanuel Rey-Herme, Elisabeth Rickert, Jekabs Romans, Elisa Romero-Romero, Marine Vandebrouck, Piet Van Duppen, Thomas Walther, and Jessica Warbinek.
Opportunities and limitations of in-gas-cell spectroscopy of the heaviest elements with RADRIS.
Nuclear Inst. and Methods in Physics Research, B, 2023.
Proceedings of the XIXth International Conference on Electromagnetic Isotope Separators and Related Topics (EMIS2022), Daejeon, South Korea, 3-7 October 2022.
- [20] G. Eiceman and Z. Karpas.
Ion Mobility Spectrometry.
CRC Press, Inc., Boca Raton, Ann Arbor, London, Tokyo, 1994.
- [21] Giorgio Visentin.
Accurate ab initio evaluation of the interatomic potentials and long-range coefficients.
PhD thesis, Skolkovo Institute of Science and Technology, Moscow, 2021.
- [22] Mustapha Laatiaoui, H Backe, D Habs, P Kunz, W Lauth, and M Sewtz.
Low-field mobilities of rare-earth metals.
The European Physical Journal D, 232(66), 2012.
- [23] P.R.Kemper and M.T.Bowers.
Electronic-state chromatography: application to first-row transition-metal ions.
J. Phys. Chem., 95:5134–5146, 1991.
- [24] J. Blaise and J.F. Wyart.
Selected constants energy levels and atomic spectra of actinides.
International Tables of selected constants, Paris, 1992.
- [25] J.P. Desclaux.

BIBLIOGRAPHY

- Relativistic Dirac-Fock Expectation Values for Atoms with $Z = 1$ to $Z = 120$.
Atomic Data and Nuc. Data Tables, 12, 1973.
- [26] Mustapha Laatiaoui, Alexei A. Buchachenko, and Larry A. Viehland.
Laser resonance chromatography of superheavy elements.
Phys. Rev. Lett., 125:023002, Jul 2020.
- [27] Wolfgang Demtröder.
Experimentalphysik 3 : Atome, Moleküle und Festkörper. , überarb. und erw. Aufl.
Springer-Verlag, 2016.
- [28] Peter van der Straten and Harold Metcalf.
Atoms and molecules interacting with light.
Cambridge University Press, 2016.
- [29] Ingolf V. Hertel and Claus-Peter Schulz.
Atome, Moleküle und optische Physik 1, Atomphysik und Grundlagen der Spektroskopie.
Springer-Verlag, 2008.
- [30] Willis E. Lamb and Robert C. Retherford.
Fine structure of the hydrogen atom by a microwave method.
Phys. Rev., 72:241–243, Aug 1947.
- [31] E. Borie.
Lamb shift of muonic deuterium.
Phys. Rev. A, 72:052511, Nov 2005.
- [32] Tobias Nebel.
The Lamb shift in muonic hydrogen : Die Lamb-Verschiebung in myonischem Wasserstoff.
PhD thesis, 2010.
Munich, Univ., Diss., 2010.
- [33] E W Otten.
Nuclear radii and moments of unstable isotopes.
1987.
- [34] K. Heilig and A. Steudel.
Changes in mean-square nuclear charge radii from optical isotope shifts.
Atomic Data and Nuclear Data Tables, 14(5):613–638, 1974.
Nuclear Charge and Moment Distributions.
- [35] B. Cheal and K.T. Flanagan.
Progress in laser spectroscopy at radioactive ion beam facilities.
Journal of Physics G: Nuclear and Particle Physics, 37(113101), 2010.
- [36] S. Raeder.

BIBLIOGRAPHY

- Spurenanalyse von Aktiniden in der Umwelt mittels Resonanzionisations-Massenspektrometrie.*
PhD thesis, Johannes Gutenberg-Universität Mainz, 2011.
- [37] Ann-Marie Mårtensson-Pendrill, Anders Ynnerman, Håkan Warston, Ludo Vermeeren, Roger E. Silverans, Alexander Klein, Rainer Neugart, Christoph Schulz, Peter Lievens, and The ISOLDE Collaboration.
Isotope shifts and nuclear-charge radii in singly ionized $^{40-48}\text{Ca}$.
Phys. Rev. A, 45:4675–4681, Apr 1992.
- [38] V. V. Flambaum, A. J. Geddes, and A. V. Viatkina.
Isotope shift, nonlinearity of King plots, and the search for new particles.
Phys. Rev. A, 97:032510, Mar 2018.
- [39] Gerda Neyens.
Nuclear magnetic and quadrupole moments for nuclear structure research on exotic nuclei.
Reports on Progress in Physics, 66(4):633, mar 2003.
- [40] K.E.G. Löbner, M. Vetter, and V. Höning.
Nuclear intrinsic quadrupole moments and deformation parameters.
Atomic Data and Nuclear Data Tables, 7(5):495–564, 1970.
- [41] P. Stránský, A. Frank, and R. Bijker.
On prolate shape predominance in nuclear deformation.
Journal of Physics: Conference Series, 322(1):012018, 2011.
- [42] P. Möller, A.J. Sierk, T. Ichikawa, and H. Sagawa.
Nuclear ground-state masses and deformations: FRDM(2012).
Atomic Data and Nuclear Data Tables, 109-110:1–204, 2016.
- [43] Peter Schwerdtfeger, Luká F. Pateka, Andrew Punnett, and Patrick Oswald Bowman.
Relativistic and quantum electrodynamic effects in superheavy elements.
Nuclear Physics, 944:551–577, 2015.
- [44] Saleh O. Allehabi, Jiguang Li, V.A. Dzuba, and V.V. Flambaum.
Theoretical study of electronic structure of erbium and fermium.
Journal of Quantitative Spectroscopy and Radiative Transfer, 253:107137, 2020.
- [45] Elisabeth Rickert, Hartmut Backe, Michael Block, Mustapha Laatiaoui, Werner Lauth, Jonas Schneider, and Fabian Schneider.
Ion mobilities for heaviest element identification.
Hyperfine Interactions, 241, 2020.
- [46] P. Indelicato, J. P. Santos, S. Boucard, and J.-P. Desclaux.
QED and relativistic corrections in superheavy elements.
The European Physical Journal D, 45(1):155–170, 2007.
- [47] Desclaux, J.-P. and Fricke, B.

BIBLIOGRAPHY

- Relativistic prediction of the ground state of atomic lawrencium.
J. Phys. France, 41(9):943–946, 1980.
- [48] M. Göppert Mayer.
On Closed Shells in Nuclei. II.
Phys. Rev., 75:1969, 1949.
- [49] O. Haxel, J. H. D. Jensen, and H. E. Suess.
On the ‘magic numbers‘ in nuclear structure.
Phys. Rev., 75:1766, 1949.
- [50] William D Myers and W.J Swiatecki.
Average nuclear properties.
Annals of Physics, 55(3):395–505, 1969.
- [51] V W Strutinsky.
Nuclear radii and moments of unstable isotopes.
page 205 p, 1987.
- [52] P. Moller, J.R. Nix, W.D. Myers, and W.J. Swiatecki.
Nuclear ground-state masses and deformations.
Atomic Data and Nuclear Data Tables, 59(2):185–381, 1995.
- [53] H. Olofsson, R. Bengtsson, and P. Möller.
Particle number projection in the macroscopic–microscopic approach.
Nuclear Physics A, 784(1):104–146, 2007.
- [54] Jens-Volker Kratz and Karl Heinrich Lieser.
Nuclear and Radiochemistry - Fundamentals and Applications.
Wiley-VCH Verlag GmbH Co. KGaA, Boschstr. 12, 69469 Weinheim, Germany, 2013.
- [55] C. F. v. Weizsäcker.
Zur Theorie der Kernmassen.
Zeitschrift für Physik, 96(7):431–458, 1935.
- [56] Vladimir Zelevinsky and Alexander Volya.
Physics of Atomic Nuclei, First Edition.
Wiley-VCH Verlag GmbH Co. KGaA, Boschstr. 12, 69469 Weinheim, Germany, 2017.
- [57] M. Göppert Mayer.
Nuclear Configurations in the Spin-Orbit Coupling Model. I. Empirical Evidence.
Phys. Rev., 78(1):16–21, 1950.
- [58] Wolfgang Demtröder.
Experimentalphysik 4 : Kern-, Teilchen- und Astrophysik , überarb. und erw. Aufl.
Springer-Verlag, 2017.

BIBLIOGRAPHY

- [59] S. G. Nilsson.
Binding states of individual nucleons in strongly deformed nuclei.
Dan. Mat. Fys. Medd. 29, 16:1–69, 1955.
- [60] R. B. Firestone.
Table of isotopes, 8 ed.
John Wiley Sons, New York, 1999.
- [61] S.G. Nilsson, S.G. Thompson, and C.F. Tsang.
Stability of superheavy nuclei and their possible occurrence in nature.
Physics Letters B, 28(7):458–461, 1969.
- [62] S. E. Agbemava, A. V. Afanasjev, D. Ray, and P. Ring.
Global performance of covariant energy density functionals: Ground state observables of even-even nuclei and the estimate of theoretical uncertainties.
Phys. Rev. C, 89:054320, 2014.
- [63] P. T. Greenlees, R.-D. Herzberg, S. Ketelhut, P. A. Butler, P. Chowdhury, T. Grahn, C. Gray-Jones, G. D. Jones, P. Jones, R. Julin, S. Juutinen, T.-L. Khoo, M. Leino, S. Moon, M. Nyman, J. Pakarinen, P. Rahkila, D. Rostron, J. Sarén, C. Scholey, J. Sorri, S. K. Tandel, J. Uusitalo, and M. Venhart.
High- K structure in ^{250}Fm and the deformed shell gaps at $N = 152$ and $Z = 100$.
Phys. Rev. C, 78:021303, Aug 2008.
- [64] B. R. Mottelson and S. G. Nilsson.
Classification of the nucleonic states in deformed nuclei.
Phys. Rev., 99(5):1615–1617, 1955.
- [65] Sven Gösta Nilsson, Chin Fu Tsang, Adam Sobiczewski, Zdzislaw Szymański, Slawomir Wycech, Christer Gustafson, Inger-Lena Lamm, Peter Möller, and Björn Nilsson.
On the nuclear structure and stability of heavy and superheavy elements.
Nuclear Physics A, 131(1):1–66, 1969.
- [66] Michael Block, Francesca Giacoppo, Fritz-Peter Heßberger, and Sebastian Raeder.
Recent progress in experiments on the heaviest nuclides at SHIP.
La Rivista del Nuovo Cimento, 45:279–323, 2022.
- [67] T Kühl, Ph Dabkiewicz, C Duke, H Fischer, H-J Kluge, H Kremmling, and E-W Otten.
Nuclear shape staggering in very neutron-deficient hg isotopes detected by laser spectroscopy.
Physical Review Letters, 39(4):180, 1977.
- [68] AN Andreyev, M Huyse, Piet Van Duppen, L. Weissman, D. Ackermann, J Gerl, FP Hessberger, S. Hofmann, A Kleinbohl, G. Münzenberg,

BIBLIOGRAPHY

- S Reshitko, C Schlegel, H Schaffner, Peter Cagarda, Melquior Matos, Sofia Saro, Alex Keenan, C Moore, CD O’Leary, and Kris Heyde.
A triplet of differently shaped spin-zero states in the atomic nucleus ^{186}Pb .
Nature, 405:430–3, 06 2000.
- [69] K. Heyde, P. Van Isacker, M. Waroquier, J.L. Wood, and R.A. Meyer.
Coexistence in odd-mass nuclei.
Physics Reports, 102(5):291–393, 1983.
- [70] J.L Wood, K Heyde, W Nazarewicz, M Huyse, and P van Duppen.
Coexistence in even-mass nuclei.
Physics Reports, 215(3):101–201, 1992.
- [71] M. Bender, W. Nazarewicz, and P.-G. Reinhard.
Shell stabilization of super- and hyperheavy nuclei without magic gaps.
Physics Letters B, 515(1):42–48, 2001.
- [72] Peter Ring and Peter Schuck.
The nuclear many-body problem.
Springer Science & Business Media, 2004.
- [73] A. E. Barzakh, J. G. Cubiss, A. N. Andreyev, M. D. Seliverstov, B. Andel, S. Antalic, P. Ascher, D. Atanasov, D. Beck, J. Bieroń, K. Blaum, Ch. Borgmann, M. Breitenfeldt, L. Capponi, T. E. Cocolios, T. Day Goodacre, X. Derkx, H. De Witte, J. Elseviers, D. V. Fedorov, V. N. Fedosseev, S. Fritzsche, L. P. Gaffney, S. George, L. Ghys, F. P. Heßberger, M. Huyse, N. Imai, Z. Kalaninová, D. Kisler, U. Köster, M. Kowalska, S. Kreim, J. F. W. Lane, V. Liberati, D. Lunney, K. M. Lynch, V. Manea, B. A. Marsh, S. Mitsuoka, P. L. Molkanov, Y. Nagame, D. Neidherr, K. Nishio, S. Ota, D. Pauwels, L. Popescu, D. Radulov, E. Rapisarda, J. P. Revill, M. Rosenbusch, R. E. Rossel, S. Rothe, K. Sandhu, L. Schweikhard, S. Sels, V. L. Truesdale, C. Van Beveren, P. Van den Bergh, P. Van Duppen, Y. Wakabayashi, K. D. A. Wendt, F. Wienholtz, B. W. Whitmore, G. L. Wilson, R. N. Wolf, and K. Zuber.
Inverse odd-even staggering in nuclear charge radii and possible octupole collectivity in $^{217,218,219}\text{At}$ revealed by in-source laser spectroscopy.
Phys. Rev. C, 99:054317, May 2019.
- [74] H-Jürgen Kluge and Wilfried Nörtershäuser.
Lasers for nuclear physics.
Spectrochimica Acta Part B: Atomic Spectroscopy, 58(6):1031–1045, 2003.
- [75] R.-D. Herzberg, P. T. Greenlees, P. A. Butler, G. D. Jones, M. Venhart, I. G. Darby, S. Eeckhautd, K. Eskola, T. Grahn, C. Gray-Jones, F. P. Hessberger, P. Jones, R. Julin, S. Juutinen, S. Ketelhut, W. Korten, M. Leino, A.-P. Leppänen, S. Moon, M. Nyman, R. D. Page, J. Pakarinen, A. Pritchard, P. Rahkila, J. Sarén, C. Scholey, A. Steer, Y. Sun, Ch. Theisen, and J. Uusitalo.

BIBLIOGRAPHY

- Nuclear isomers in superheavy elements as stepping stones towards the island of stability.
Nature, 422:896–899, 2006.
- [76] Zygmunt Patyk, Adam Sobiczewski, Peter Armbruster, and Karl-Heinz Schmidt.
Shell effects in the properties of the heaviest nuclei.
Nuclear Physics A, 491(2):267–280, 1989.
- [77] Albert Einstein.
Ist die Trägheit eines Körpers von seinem Energieinhalt abhängig?
Annalen der Physik, 323(13):639–641, 1905.
- [78] RF Ruiz and AR Vernon.
Emergence of simple patterns in many-body systems: from macroscopic objects to the atomic nucleus.
The European Physical Journal A, 56(5):1–17, 2020.
- [79] I Angeli and K P Marinova.
Correlations of nuclear charge radii with other nuclear observables.
Journal of Physics G: Nuclear and Particle Physics, 42(5):055108, mar 2015.
- [80] I Angeli, Yu P Gangrsky, K P Marinova, I N Boboshin, S Yu Komarov, B S Ishkhanov, and V V Varlamov.
 N and Z dependence of nuclear charge radii.
Journal of Physics G: Nuclear and Particle Physics, 36(8):085102, jun 2009.
- [81] M. Dworschak, G. Audi, K. Blaum, P. Delahaye, S. George, U. Hager, F. Herfurth, A. Herlert, A. Kellerbauer, H.-J. Kluge, D. Lunney, L. Schweikhard, and C. Yazidjian.
Restoration of the $N = 82$ shell gap from direct mass measurements of $^{132,134}\text{Sn}$.
Phys. Rev. Lett., 100:072501, Feb 2008.
- [82] K. Rutz, M. Bender, T. Bürvenich, T. Schilling, P.-G. Reinhard, J. A. Maruhn, and W. Greiner.
Superheavy nuclei in self-consistent nuclear calculations.
Phys. Rev. C, 56:238–243, Jul 1997.
- [83] K. L. Jones, A. S. Adekola, D. W. Bardayan, J. C. Blackmon, K. Y. Chae, K. A. Chipps, J. A. Cizewski, L. Erikson, C. Harlin, R. Hatarik, R. Kapler, R. L. Kozub, J. F. Liang, R. Livesay, Z. Ma, B. H. Moazen, C. D. Nesaraja, F. M. Nunes, S. D. Pain, N. P. Patterson, D. Shapira, J. F. Shriner, M. S. Smith, T. P. Swan, and J. S. Thomas.
The magic nature of ^{132}Sn explored through the single-particle states of ^{133}Sn .
Nature, 465(7297):454–457, may 2010.

BIBLIOGRAPHY

- [84] C. Gorges, L. V. Rodríguez, D. L. Balabanski, M. L. Bissell, K. Blaum, B. Cheal, R. F. Garcia Ruiz, G. Georgiev, W. Gins, H. Heylen, A. Kanellakopoulos, S. Kaufmann, M. Kowalska, V. Lagaki, S. Lechner, B. Maaß, S. Malbrunot-Ettenauer, W. Nazarewicz, R. Neugart, G. Neyens, W. Nörtershäuser, P.-G. Reinhard, S. Sailer, R. Sánchez, S. Schmidt, L. Wehner, C. Wraith, L. Xie, Z. Y. Xu, X. F. Yang, and D. T. Yordanov.
Laser spectroscopy of neutron-rich tin isotopes: A discontinuity in charge radii across the $N = 82$ shell closure.
Phys. Rev. Lett., 122:192502, May 2019.
- [85] O. Sorlin and M.-G. Porquet.
Nuclear magic numbers: New features far from stability.
Progress in Particle and Nuclear Physics, 61(2):602–673, 2008.
- [86] M. Bender, G. F. Bertsch, and P.-H. Heenen.
Global study of quadrupole correlation effects.
Phys. Rev. C, 73:034322, Mar 2006.
- [87] Philip Walker and George Dracoulis.
Energy traps in atomic nuclei.
Nature, 399(6731):35–40, 1999.
- [88] O. R. Smits, P. Indelicato, W. Nazarewicz, M. Piibeleht, and P. Schwerdtfeger.
Pushing the limits of the periodic table – a review on atomic relativistic electronic structure theory and calculations for the superheavy elements, 2023.
- [89] P-G Reinhard.
Estimating the relevance of predictions from the Skyrme–Hartree–Fock model.
Physica Scripta, 91(2):023002, dec 2015.
- [90] J. Dobaczewski, A.V. Afanasjev, M. Bender, L.M. Robledo, and Yue Shi.
Properties of nuclei in the nobelium region studied within the covariant, skyrme, and gogny energy density functionals.
Nuclear Physics A, 944:388–414, 2015.
Special Issue on Superheavy Elements.
- [91] A. Sobczewski, I. Muntian, and Z. Patyk.
Problem of “deformed” superheavy nuclei.
Phys. Rev. C, 63:034306, Feb 2001.
- [92] Paul-Gerhard Reinhard and Witold Nazarewicz.
Nuclear charge densities in spherical and deformed nuclei: Toward precise calculations of charge radii.
Phys. Rev. C, 103:054310, May 2021.
- [93] A Ghiorso, SG Thompson, GH Higgins, BG Harvey, and GT Seaborg.

BIBLIOGRAPHY

- Evidence for subshell at $N = 152$.
Physical Review, 95(1):293, 1954.
- [94] G. Audi, A.H. Wapstra, and C. Thibault.
The AME2003 atomic mass evaluation: (II). tables, graphs and references.
Nuclear Physics A, 729(1):337–676, 2003.
The 2003 NUBASE and Atomic Mass Evaluations.
- [95] E Minaya Ramirez, D Ackermann, Klaus Blaum, M Block, Ch Droese, Ch E Düllmann, M Dworschak, M Eibach, Sergey Eliseev, E Haettner, et al.
Direct mapping of nuclear shell effects in the heaviest elements.
Science, 337(6099):1207–1210, 2012.
- [96] Ch. Theisen, P.T. Greenlees, T.-L. Khoo, P. Chowdhury, and T. Ishii.
In-beam spectroscopy of heavy elements.
Nuclear Physics A, 944:333–375, 2015.
Special Issue on Superheavy Elements.
- [97] K. Hauschild, A. Lopez-Martens, A. V. Yeremin, O. Dorvaux, S. Antalic, A. V. Belozero, Ch. Briançon, M. L. Chelnokov, V. I. Chepigin, D. Curien, B. Gall, A. Görden, V. A. Gorshkov, M. Guttormsen, F. Hanappe, A. P. Kabachenko, F. Khalfallah, A. C. Larsen, O. N. Malyshev, A. Minkova, A. G. Popeko, M. Rousseau, N. Rowley, S. Saro, A. V. Shutov, S. Siem, L. Stuttgè, A. I. Svirikhin, N. U. H. Syed, Ch. Theisen, and M. Venhart.
High- K , $t_{1/2} = 1.4(1)$ ms, isomeric state in ^{255}Lr .
Phys. Rev. C, 78:021302, Aug 2008.
- [98] Albert Ghiorso, Kari Eskola, Pirkko Eskola, and Matti Nurmi.
Isomeric states in ^{250}Fm and ^{254}No .
Phys. Rev. C, 7:2032–2036, May 1973.
- [99] F. P. Heßberger, S. Antalic, B. Sulignano, D. Ackermann, S. Heinz, S. Hofmann, B. Kindler, J. Khuyagbaatar, I. Kojouharov, P. Kuusiniemi, M. Leino, B. Lommel, R. Mann, K. Nishio, A. G. Popeko, Š. Šáro, B. Streicher, J. Uusitalo, M. Venhart, and A. V. Yeremin.
Decay studies of K isomers in ^{254}No .
The European Physical Journal A, 43(1):55–66, 2009.
- [100] S. K. Tandel, T. L. Khoo, D. Seweryniak, G. Mukherjee, I. Ahmad, B. Back, R. Blinstrup, M. P. Carpenter, J. Chapman, P. Chowdhury, C. N. Davids, A. A. Hecht, A. Heinz, P. Ikin, R. V. F. Janssens, F. G. Kondev, T. Lauritsen, C. J. Lister, E. F. Moore, D. Peterson, P. Reiter, U. S. Tandel, X. Wang, and S. Zhu.
K isomers in ^{254}No : Probing single-particle energies and pairing strengths in the heaviest nuclei.
Phys. Rev. Lett., 97:082502, Aug 2006.
- [101] Ackermann, Dieter.

BIBLIOGRAPHY

- Nuclear structure of superheavy nuclei - state of the art and perspectives (@ S3).
EPJ Web Conf., 193:04013, 2018.
- [102] Julien Piot, B. Gall, O. Dorvaux, P. Greenlees, N. Rowley, L. Andersson, Daniel Cox, F. Dechery, T. Grahn, Karl Hauschild, Greg Henning, Andrej Herzáň, R. Herzberg, F. Hessberger, Ulrika Jakobsson, Pete Jones, R. Julin, S. Juutinen, Steffen Ketelhut, and Juha Uusitalo.
In-beam spectroscopy with intense ion beams: Evidence for a rotational structure in Fm-246.
Physical Review C, 85, 04 2012.
- [103] Steffen Ketelhut.
Rotational Structures and High-K Isomerism in $^{248,250}\text{Fm}$.
PhD thesis, University of Jyväskylä, 2010.
- [104] R.-D. Herzberg and D. M. Cox.
Spectroscopy of actinide and transactinide nuclei.
Radiochimica Acta, 99(7-8):441–457, 2011.
- [105] P T Greenlees.
Pushing the limits: Nuclear structure of heavy elements.
Journal of Physics: Conference Series, 381(1):012022, sep 2012.
- [106] M Leino, H Kankaanpää, R-D Herzberg, AJ Chewter, FP Heßberger, Y Le Coz, F Becker, PA Butler, JFC Cocks, O Dorvaux, K. Eskola, J. Gerl, P.T. Greenlees, K. Helariutta, M. Houry, G.D. Jones, P. Jones, R. Julin, S. Juutinen, H. Kettunen, T.L. Khoo, A. Kleinböhl, W. Kortén, P. Kuusiniemi, R. Lucas, M. Muikku, P. Nieminen, R.D. Page, P. Rahkila, P. Reiter, A. Savelius, Ch. Schlegel, Ch. Theisen, W.H. Trzaska, and H.-J. Wollersheim.
In-beam study of ^{254}No .
The European Physical Journal A-Hadrons and Nuclei, 6(1):63–69, 1999.
- [107] P T Greenlees.
Understanding the nuclear structure of heavy elements.
Physica Scripta, 2013(T152):014016, 2013.
- [108] Paul J. Karol, Robert C. Barber, Bradley M. Sherrill, Emanuele Vardaci, and Toshimitsu Yamazaki.
Discovery of the element with atomic number $Z = 118$ completing the 7th row of the periodic table (iupac technical report).
Pure and Applied Chemistry, 88(1-2):155–160, 2016.
- [109] Kenta Hotokezaka, Paz Beniamini, and Tsvi Piran.
Neutron star mergers as sites of r-process nucleosynthesis and short gamma-ray bursts.
International Journal of Modern Physics D, 27(13):1842005, 2018.
- [110] JE Bigelow, BL Corbett, LJ King, SC McGuire, and TM Sims.

BIBLIOGRAPHY

- Production of transplutonium elements in the high flux isotope reactor.
ACS Publications, 1981.
- [111] Frank Rösch.
Nuclear-and Radiochemistry.
Walter de Gruyter GmbH & Company, KG, 2014.
- [112] R. Bass.
Fusion of heavy nuclei in a classical model.
Nuclear Physics A, 231(1):45–63, 1974.
- [113] W. Reisdorf.
Analysis of fissionability data at high excitation energies.
Zeitschrift für Physik A Atoms and Nuclei, 300(2):227–238, 1981.
- [114] W Reisdorf and M Schädel.
How well do we understand the synthesis of heavy elements by heavy-ion induced fusion?
Zeitschrift für Physik A Hadrons and Nuclei, 343(1):47–57, 1992.
- [115] Oliver T. Kaleja.
High-precision mass spectrometry of nobelium, lawrencium and rutherfordium isotopes and studies of long-lived isomers with SHIPTRAP.
PhD thesis, Mainz, 2020.
- [116] Yu.Ts. Oganessian.
Synthesis and decay properties of heaviest nuclei with ^{48}Ca -induced reactions.
Nuclear Physics A, 787(1):343–352, 2007.
Proceedings of the Ninth International Conference on Nucleus-Nucleus Collisions.
- [117] P. Armbruster.
On the production of superheavy elements.
Annual Review of Nuclear and Particle Science, 50(1):411–479, 2000.
- [118] R.-D. Herzberg and P.T. Greenlees.
In-beam and decay spectroscopy of transfermium nuclei.
Progress in Particle and Nuclear Physics, 61(2):674–720, 2008.
- [119] A. Türler, H. R. von Gunten, J. D. Leyba, D. C. Hoffman, D. M. Lee, K. E. Gregorich, D. A. Bennett, R. M. Chasteler, C. M. Gannett, H. L. Hall, R. A. Henderson, and M. J. Nurmia.
Actinide production from the interactions of ^{40}Ca and ^{44}Ca with ^{248}Cm and a comparison with the $^{48}\text{Ca}+^{248}\text{Cm}$ system.
Phys. Rev. C, 46:1364–1382, Oct 1992.
- [120] G. N. Flerov, S. M. Polikanov, V. L. Mikheev, V. I. Ilyushchenko, M. B. Miller, and V. A. Shchegolev.
Synthesis of isotopes of fermium with mass numbers 247 and 246.
Soviet Atomic Energy, 22:434–437, 1967.

BIBLIOGRAPHY

- [121] J. Khuyagbaatar, F. P. Heßberger, S. Hofmann, D. Ackermann, H. G. Burkhard, S. Heinz, B. Kindler, I. Kojouharov, B. Lommel, R. Mann, J. Maurer, and K. Nishio.
 α decay of $^{243}\text{Fm}_{143}$ and $^{245}\text{Fm}_{145}$, and of their daughter nuclei.
Phys. Rev. C, 102:044312, Oct 2020.
- [122] J. Khuyagbaatar, S. Hofmann, F. P. Heßberger, D. Ackermann, H. G. Burkhard, S. Heinz, B. Kindler, I. Kojouharov, B. Lommel, R. Mann, J. Maurer, K. Nishio, and Yu. Novikov.
Spontaneous fission of neutron-deficient fermium isotopes and the new nucleus ^{241}Fm .
The European Physical Journal A, 37:177–183, 2008.
- [123] G Münzenberg, W Faust, S Hofmann, P Armbruster, K Güttner, and H Ewald.
The velocity filter SHIP, a separator of unslowed heavy ion fusion products.
Nuclear Instruments and Methods, 161(1):65–82, 1979.
- [124] J. Dilling, D. Ackermann, J. Bernard, F.P. Hessberger, S. Hofmann, W. Hornung, H.J. Kluge, E. Lamour, M. Maier, R. Mann, G. Marx, R.B. Moore, G. Münzenberg, W. Quint, D. Rodriguez, M. Schädel, J. Schönfelder, G. Sikler, C. Toader, L. Vermeeren, C. Weber, G. Bollen, O. Engels, D. Habs, P. Thirolf, H. Backe, A. Dretzke, W. Lauth, W. Ludolphs, and M. Sewtz.
The SHIPTRAP project: A capture and storage facility at GSI for heavy radionuclides from SHIP.
Hyperfine Interactions, 127(1):491–496, 2000.
- [125] H. Backe, W. Lauth, M. Block, and M. Laatiaoui.
Prospects for laser spectroscopy, ion chemistry and mobility measurements of superheavy elements in buffer-gas traps.
Nuclear Physics A, 944:492–517, 2015.
Special Issue on Superheavy Elements.
- [126] S. Raeder, D. Ackermann, H. Backe, R. Beerwerth, J. C. Berengut, M. Block, A. Borschevsky, B. Cheal, P. Chhetri, Ch. E. Düllmann, V. A. Dzuba, E. Eliav, J. Even, R. Ferrer, V. V. Flambaum, S. Fritzsche, F. Giacoppo, S. Götz, F. P. Heßberger, M. Huyse, U. Kaldor, O. Kaleja, J. Khuyagbaatar, P. Kunz, M. Laatiaoui, F. Lautenschläger, W. Lauth, A. K. Mistry, E. Minaya Ramirez, W. Nazarewicz, S. G. Porsev, M. S. Safronova, U. I. Safronova, B. Schuetrumpf, P. Van Duppen, T. Walther, C. Wraith, and A. Yakushev.
Probing sizes and shapes of nobelium isotopes by laser spectroscopy.
Phys. Rev. Lett., 120:232503, Jun 2018.
- [127] P. Chhetri.
Laser spectroscopy of Nobelium Isotopes.
PhD thesis, Technische Universität Darmstadt, 2018.

BIBLIOGRAPHY

- [128] Sigurd Hofmann and Gottfried Münzenberg.
The discovery of the heaviest elements.
Reviews of Modern Physics, 72(3):733, 2000.
- [129] M. Asai, F.P. Heßberger, and A. Lopez-Martens.
Nuclear structure of elements with $100 \leq Z \leq 109$ from alpha spectroscopy.
Nuclear Physics A, 944:308–332, 2015.
Special Issue on Superheavy Elements.
- [130] P. A. Butler, R. D. Humphreys, P. T. Greenlees, R.-D. Herzberg, D. G. Jenkins, G. D. Jones, H. Kankaanpää, H. Kettunen, P. Rahkila, C. Scholey, J. Uusitalo, N. Amzal, J. E. Bastin, P. M. T. Brew, K. Eskola, J. Gerl, N. J. Hammond, K. Hauschild, K. Helariutta, F.-P. Heßberger, A. Hürstel, P. M. Jones, R. Julin, S. Juutinen, A. Keenan, T.-L. Khoo, W. Korten, P. Kuusiniemi, Y. Le Coz, M. Leino, A.-P. Leppänen, M. Muikku, P. Nieminen, S. W. Ødegård, T. Page, J. Pakarinen, P. Reiter, G. Sletten, Ch. Theisen, and H.-J. Wollersheim.
Conversion electron cascades in ${}_{102}^{254}\text{No}$.
Phys. Rev. Lett., 89:202501, Oct 2002.
- [131] Xiaofei Yang, the COLLAPS, and CRIS collaboration.
Precision laser spectroscopy technique for exotic radioactive beams at cern-isolde.
Journal of Physics: Conference Series, 1024(1):012031, may 2018.
- [132] Phillip Imgram, Kristian König, Jörg Krämer, Tim Ratajczyk, Bernhard Maaß, Patrick Müller, Felix Sommer, and Wilfried Nörtershäuser.
High-precision collinear laser spectroscopy at the collinear apparatus for laser spectroscopy and applied physics (coala).
Hyperfine Interactions, 241:1–8, 2020.
- [133] Rainer Neugart, Jonathan Billowes, ML Bissell, Klaus Blaum, B Cheal, KT Flanagan, Gerda Neyens, W Nörtershäuser, and DT Yordanov.
Collinear laser spectroscopy at isolde: new methods and highlights.
Journal of Physics G: Nuclear and Particle Physics, 44(6):064002, 2017.
- [134] M. Sewtz, H. Backe, A. Dretzke, G. Kube, W. Lauth, P. Schwamb, K. Eberhardt, C. Grüning, P. Thörle, N. Trautmann, P. Kunz, J. Lassen, G. Passler, C. Z. Dong, S. Fritzsche, and R. G. Haire.
First observation of atomic levels for the element fermium ($Z=100$).
Phys. Rev. Lett., 90:163002, Apr 2003.
- [135] Wolfgang Demtröder.
Laserspektroskopie, Grundlagen und Techniken , überarb. und erw. Aufl.
Springer-Verlag, 2007.
- [136] M. Sewtz.
Optische Spektroskopie an Fermium ($Z=100$).
PhD thesis, Johannes Gutenberg-Universität Mainz, 2003.

BIBLIOGRAPHY

- [137] R. Loudon.
The Quantum Theory of Light.
Clarendon Press, Oxford, 3rd ed., 2006.
- [138] Lambda Physik.
FL 2002 Operators Manual, Rev. 1, Tech. rep.,.
Lambda Physik GmbH, D-37079 Göttingen, 1982.
- [139] Zhenxu Bai, Zhongan Zhao, Menghan Tian, Duo Jin, Yajun Pang, Sensen Li, Xiusheng Yan, Yulei Wang, and Zhiwei Lu.
A comprehensive review on the development and applications of narrow-linewidth lasers.
Microwave and Optical Technology Letters, 64(12):2244–2255, 2022.
- [140] Klaus D. A. Wendt, Klaus Blaum, Christopher Geppert, Peter Müller, Wilfried Nörtershäuser, Annette Schmitt, Philipp Schumann, Norbert Trautmann, and Bruce A. Bushaw.
Laser based techniques for ultra trace isotope production, spectroscopy and detection.
In Z. Błaszczak, B. Markov, and K. Marinova, editors, *Laser 2004*, pages 147–157, Berlin, Heidelberg, 2006. Springer Berlin Heidelberg.
- [141] K-H Weber and Craig J Sansonetti.
Accurate energies of nS, nP, nD, nF, and nG levels of neutral cesium.
Physical Review A, 35(11):4650, 1987.
- [142] F. Lautenschläger, P. Chhetri, D. Ackermann, H. Backe, M. Block, B. Cheal, A. Clark, C. Droese, R. Ferrer, F. Giacoppo, S. Götz, F.P. Heßberger, O. Kaleja, J. Khuyagbaatar, P. Kunz, A.K. Mistry, M. Laatiaoui, W. Lauth, S. Raeder, Th. Walther, and C. Wraith.
Developments for resonance ionization laser spectroscopy of the heaviest elements at SHIP.
Nuclear Instruments and Methods in Physics Research Section B: Beam Interactions with Materials and Atoms, 383:115–122, 2016.
- [143] Tobias Murböck, Sebastian Raeder, Premaditya Chhetri, Katerine Diaz, Mustapha Laatiaoui, Francesca Giacoppo, and Michael Block.
Filament studies for laser spectroscopy on lawrencium.
Hyperfine Interactions, 241(1):1–9, 2020.
- [144] Earl McDaniel and Edward Mason.
The mobility and diffusion of ions in gases.
John Wiley & Sons, New York, 1973.
- [145] C. L. Wilkins and S. Trimpin.
Ion Mobility Spectrometry - Mass Spectrometry, Theory and Application.
CRC Press, Inc., Boca Raton, London, New York, 2011.
- [146] Larry A. Viehland, Tamar Skaist, Chetana Adhikari, and William F. Siems.

BIBLIOGRAPHY

- Accurate zero-field mobilities of atomic ions in the rare gases for calibration of ion mobility spectrometers.
International Journal for Ion Mobility Spectrometry, 20(1):1–9, 2017.
- [147] Earl McDaniel and Edward Mason.
Transport Properties of Ions in Gases.
John Wiley & Sons, New York, 1988.
- [148] L. Viehland and E. Mason.
Tables of transport collision integrals for (n, 6,4) ion-neutral potentials.
Atomic data and nuclear data tables, 1975.
- [149] L. A. Viehland.
Gaseous Ion Mobility, Diffusion, and Reaction.
Springer Series on Atomic, Optical, and Plasma Physics, 2018.
- [150] M. Laatiaoui.
Development of an Ion Mobility Spectrometer for Heavy Element Research.
PhD thesis, Ludwig–Maximilians–Universität München, 2009.
- [151] Mass spectrometry : A foundation course, 2004.
- [152] Lester R. Morss.
The Chemistry of the Actinide and Transactinide Elements.
Dordrecht, third edition edition, 2006.
- [153] A. Ghiorso, S. G. Thompson, G. H. Higgins, G. T. Seaborg, M. H. Studier, P. R. Fields, S. M. Fried, H. Diamond, J. F. Mech, G. L. Pyle, J. R. Huizenga, A. Hirsch, W. M. Manning, C. I. Browne, H. L. Smith, and R. W. Spence.
New elements einsteinium and fermium, atomic numbers 99 and 100.
Phys. Rev., 99:1048–1049, Aug 1955.
- [154] S. G. Thompson, A. Ghiorso, B. G. Harvey, and G. R. Choppin.
Transcurium isotopes produced in the neutron irradiation of plutonium.
Phys. Rev., 93:908–908, Feb 1954.
- [155] Bernard G. Harvey, Stanley G. Thompson, Albert Ghiorso, and Gregory R. Choppin.
Further production of transcurium nuclides by neutron irradiation.
Phys. Rev., 93:1129–1129, Mar 1954.
- [156] Hugo Atterling, Wilhelm Forsling, Lennart W. Holm, Lars Melander, and Björn Åström.
Element 100 produced by means of cyclotron-accelerated oxygen ions.
Phys. Rev., 95:585–586, Jul 1954.
- [157] J. Tuli.
Evaluated nuclear structure data files (ENSDF) data base.
<https://www.nndc.bnl.gov/ensdf/>, 2022.

BIBLIOGRAPHY

- [158] G. Audi, F. G. Kondev, and S. Naimi.
The nubase2016 evaluation of nuclear properties.
Chinese Physics C, 41(3):030001, mar 2017.
- [159] Sven Richter.
Implementierung der Laserionenquellenfalle LIST bei ISOLDE und Validierung der Spezifikationen Effizienz und Selektivität.
PhD thesis, Mainz, 2015.
- [160] Steven Nothhelfer.
Advances in laser spectroscopy of superheavy elements : resonance ionization spectroscopy on $^{253,254,255}\text{Es}$ and a new gas-jet based high-resolution spectroscopy setup.
PhD thesis, Johannes Gutenberg-Universität Mainz, Mainz, 2022.
- [161] S. Nothhelfer, Th. E. Albrecht-Schönzart, M. Block, P. Chhetri, Ch. E. Düllmann, J. G. Ezold, V. Gadelshin, A. Gaiser, F. Giacoppo, R. Heinke, T. Kieck, N. Kneip, M. Laatiaoui, Ch. Mokry, S. Raeder, J. Runke, F. Schneider, J. M. Sperling, D. Studer, P. Thörle-Pospiech, N. Trautmann, F. Weber, and K. Wendt.
Nuclear structure investigations of $^{253-255}\text{Es}$ by laser spectroscopy.
Phys. Rev. C, 105:L021302, Feb 2022.
- [162] Felix Weber, Christoph Emanuel Düllmann, Vadim Gadelshin, Nina Kneip, Stephan Oberstedt, Sebastian Raeder, Jörg Runke, Christoph Mokry, Petra Thörle-Pospiech, Dominik Studer, Norbert Trautmann, and Klaus Wendt.
Probing the atomic structure of californium by resonance ionization spectroscopy.
Atoms, 10(2), 2022.
- [163] Felix Weber, Thomas E. Albrecht-Schönzart, Saleh O. Allehabi, Sebastian Berndt, Michael Block, Holger Dorrer, Christoph E. Düllmann, Vladimir A. Dzuba, Julie G. Ezold, Victor V. Flambaum, Vadim Gadelshin, Stephane Goriely, Ashley Harvey, Reinhard Heinke, Stephane Hilaire, Magdalena Kaja, Tom Kieck, Nina Kneip, Ulli Köster, Jeremy Lantis, Christoph Mokry, Danny Münzberg, Steven Nothhelfer, Stephan Oberstedt, Sophie Péru, Sebastian Raeder, Jörg Runke, Volker Sonnenschein, Matou Stemmler, Dominik Studer, Petra Thörle-Pospiech, Hideki Tomita, Norbert Trautmann, Shelley Van Cleve, Jessica Warbinek, and Klaus Wendt.
Nuclear moments and isotope shifts of the actinide isotopes $^{249-253}\text{Cf}$ probed by laser spectroscopy.
Phys. Rev. C, 107:034313, Mar 2023.
- [164] Earl F. Worden, John G. Conway, and Jean Blaise.
Energy levels of the second spectrum of curium, Cm II.
J. Opt. Soc. Am. B, 3(8):1092–1101, Aug 1986.

BIBLIOGRAPHY

- [165] Earl F. Worden, John G. Conway, and Jean Blaise.
Energy levels of neutral and singly ionized berkelium, ^{249}Bk I and ^{249}Bk II.
J. Opt. Soc. Am. B, 4(9):1358–1368, Sep 1987.
- [166] H Backe, A Dretzke, St Fritzsche, RG Haire, P Kunz, W Lauth, M Sewtz,
and N Trautmann.
Laser spectroscopic investigation of the element fermium ($Z= 100$).
In *Laser 2004*, pages 3–14. Springer, 2006.
- [167] F. Asaro, S. Bjørnholm, and I. Perlman.
Decay scheme of ^{255}Fm .
Phys. Rev., 133:B291–B300, Jan 1964.
- [168] Jessica Warbinek, Brankica Anelić, Michael Block, Premaditya Chhetri,
Arno Claessens, Rafael Ferrer, Francesca Giacoppo, Oliver Kaleja, Tom
Kieck, EunKang Kim, Mustapha Laatiaoui, Jeremy Lantis, Andrew
Mistry, Danny Münzberg, Steven Nothhelfer, Sebastian Raeder, Em-
manuel Rey-Herme, Elisabeth Rickert, Jekabs Romans, Elisa Romero-
Romero, Marine Vandebrouck, Piet Van Duppen, and Thomas Walther.
Advancing Radiation-Detected Resonance Ionization towards Heavier Ele-
ments and More Exotic Nuclides.
Atoms, 10(2), 2022.
- [169] Tetsuya K. Sato, Masato Asai, Anastasia Borschevsky, Randolf Beerwerth,
Yusuke Kaneya, Hiroyuki Makii, Akina Mitsukai, Yuichiro Nagame,
Akihiko Osa, Atsushi Toyoshima, Kazuaki Tsukada, Minoru Sakama,
Shinsaku Takeda, Kazuhiro Ooe, Daisuke Sato, Yudai Shigekawa, Shin-
ichi Ichikawa, Christoph E. Düllmann, Jessica Grund, Dennis Renisch,
Jens V. Kratz, Matthias Schädel, Ephraim Eliav, Uzi Kaldor, Stephan
Fritzsche, and Thierry Stora.
First ionization potentials of Fm, Md, No, and Lr: Verification of filling-up
of 5f electrons and confirmation of the actinide series.
Journal of the American Chemical Society, 140(44):14609–14613, 2018.
PMID: 30358998.
- [170] Exciton Luxottica.
Exalite 398 data sheet.
[https://exciton.luxottica.com/pub/media/productattach/
Datasheet/03980.pdf](https://exciton.luxottica.com/pub/media/productattach/Datasheet/03980.pdf), 2023.
- [171] A. Lopez-Martens, K. Hauschild, A. V. Yerebin, A. V. Belozarov, Ch.
Brian, M. L. Chelnokov, V. I. Chepigin, D. Curien, O. Dorvaux, B. Gall,
V. A. Gorshkov, M. Guttormsen, F. Hanappe, A. P. Kabachenko,
F. Khalfallah, A. Korichi, A. C. Larsen, O. N. Malyshev, A. Minkova,
Yu. Ts. Oganessian, A. G. Popeko, M. Rousseau, N. Rowley, R. N.
Sagaidak, S. Sharo, A. V. Shutov, S. Siem, A. I. Svirikhin, N. U. H.
Syed, and Ch. Theisen.
Detailed spectroscopy of ^{249}Fm .

BIBLIOGRAPHY

- Phys. Rev. C*, 74:044303, Oct 2006.
- [172] M. Sewtz, H. Backe, C.Z. Dong, A. Dretzke, K. Eberhardt, S. Fritzsche, C. Grüning, R.G. Haire, G. Kube, P. Kunz, J. Lassen, W. Lauth, G. Passler, P. Schwamb, P. Thörle, and N. Trautmann.
Resonance ionization spectroscopy of fermium ($Z=100$).
Spectrochimica Acta Part B: Atomic Spectroscopy, 58(6):1077–1082, 2003.
LAP-2002 INTERNATIONAL CONFERENCE ON LASER PROBING.
- [173] Sharon M. Robinson, Dennis E. Benker, Emory D. Collins, Julie G. Ezold, Jon R. Garrison, and Susan L. Hogle.
Production of Cf-252 and other transplutonium isotopes at Oak Ridge National Laboratory.
Radiochimica Acta, 108(9):737–746, 2020.
- [174] Dominik Studer.
Probing atomic and nuclear structure properties of promethium by laser spectroscopy.
PhD thesis, Mainz, 2020.
- [175] Jessica Warbinek.
To be submitted.
PhD thesis, Johannes Gutenberg-Universität Mainz.
- [176] W. Lauth, H. Backe, M. Dahlinger, I. Klaft, P. Schwamb, G. Schwickert, N. Trautmann, and U. Othmer.
Resonance ionization spectroscopy in a buffer gas cell with radioactive decay detection, demonstrated using ^{208}Tl .
Phys. Rev. Lett., 68:1675–1678, Mar 1992.
- [177] Klaus Blaum, Jens Dilling, and Wilfried Nörtershäuser.
Precision atomic physics techniques for nuclear physics with radioactive beams.
Physica Scripta, 2013(T152):014017, jan 2013.
- [178] D Berdichevsky and Florence Tondeur.
Nuclear core densities, isotope shifts, and the parametrization of the droplet model.
Zeitschrift für Physik A Atoms and Nuclei, 322(1):141–147, 1985.
- [179] William D Myers and Karl-Heinz Schmidt.
An update on droplet-model charge distributions.
Nuclear Physics A, 410(1):61–73, 1983.
- [180] T. E. Cocolios, W. Dexters, M. D. Seliverstov, A. N. Andreyev, S. Antalic, A. E. Barzakh, B. Bastin, J. Büscher, I. G. Darby, D. V. Fedorov, V. N. Fedosseyev, K. T. Flanagan, S. Franchoo, S. Fritzsche, G. Huber, M. Huyse, M. Keupers, U. Köster, Yu. Kudryavtsev, E. Mané, B. A. Marsh, P. L. Molkanov, R. D. Page, A. M. Sjoedin, I. Stefan, J. Van de

BIBLIOGRAPHY

- Walle, P. Van Duppen, M. Venhart, S. G. Zemlyanoy, M. Bender, and P.-H. Heenen.
Early onset of ground state deformation in neutron deficient polonium isotopes.
Phys. Rev. Lett., 106:052503, Feb 2011.
- [181] B. Cheal, T. E. Cocolios, and S. Fritzsche.
Laser spectroscopy of radioactive isotopes: Role and limitations of accurate isotope-shift calculations.
Phys. Rev. A, 86:042501, Oct 2012.
- [182] Bastian Schuetrumpf.
private communication.
- [183] P. Klüpfel, P.-G. Reinhard, T. J. Bürvenich, and J. A. Maruhn.
Variations on a theme by skyrme: A systematic study of adjustments of model parameters.
Phys. Rev. C, 79:034310, Mar 2009.
- [184] Jiang-Ming Yao, Simone Baroni, Michael Bender, and Paul-Henri Heenen.
Beyond-mean-field study of the possible “bubble” structure of ^{34}Si .
Phys. Rev. C, 86:014310, Jul 2012.
- [185] M. Kortelainen, J. McDonnell, W. Nazarewicz, P.-G. Reinhard, J. Sarich, N. Schunck, M. V. Stoitsov, and S. M. Wild.
Nuclear energy density optimization: Large deformations.
Phys. Rev. C, 85:024304, Feb 2012.
- [186] P.-H. Heenen, J. Skalski, A. Staszczak, and D. Vretenar.
Shapes and α - and β -decays of superheavy nuclei.
Nuclear Physics A, 944:415–441, 2015.
Special Issue on Superheavy Elements.
- [187] Jessica Warbinek, Elisabeth Rickert, Sebastian Raeder, Michael Block, Brankica Anelić, Premaditya Chhetri, Arno Claessens, Rafael Ferrer, Francesca Giacoppo, Oliver Kaleja, Tom Kieck, EunKang Kim, Mustapha Laatiaoui, Jeremy Lantis, Andrew Mistry, Danny Münzberg, Steven Nothhelfer, Emmanuel Rey-Herme, Jekabs Romans, Elisa Romero-Romero, Marine Vandebrouck, Piet Van Duppen, and Thomas Walther.
in preparation.
Nature physics.
- [188] B. Schuetrumpf, W. Nazarewicz, and P.-G. Reinhard.
Central depression in nucleonic densities: Trend analysis in the nuclear density functional theory approach.
Phys. Rev. C, 96:024306, Aug 2017.
- [189] Stephane Goriely.
private communication.

BIBLIOGRAPHY

- [190] Vitek Nazarewicz.
private communication.
- [191] F. P. Heßberger, S. Hofmann, D. Ackermann, S. Antalic, B. Kindler, I. Kojouharov, P. Kuusiniemi, M. Leino, B. Lommel, R. Mann, K. Nishio, A. G. Popeko, B. Sulignano, S. Saro, B. Streicher, M. Venhart, and A. V. Yeremin.
Alpha-gamma decay studies of ^{255}Rf , ^{251}No and ^{247}Fm .
The European Physical Journal A - Hadrons and Nuclei, 30(3), 2006.
- [192] Y. Ito, P. Schury, M. Wada, F. Arai, H. Haba, Y. Hirayama, S. Ishizawa, I. S. Kimura, D. Kaji, H. Koura, M. MacCormick, H. Miyatake, J. Y. Moon, K. Morimoto, K. Morita, M. Mukai, I. Murray, T. Niwase, K. Okada, A. Ozawa, M. Rosenbusch, A. Takamine, T. Tanaka, Y. X. Watanabe, H. Wollnik, and S. Yamaki.
First direct mass measurements of nuclides around $Z = 100$ with a multireflection time-of-flight mass spectrograph.
Physical Review Letters, 120:152501, 2018.
- [193] S. Antalic, D. Heßberger, F.P. and Ackermann, S. Heinz, S. Hofmann, Z. Kalaninova, Kindler B., Khuyagbaatar, J., Ivan Kojouharov, and et al. Kuusiniemi, Pasi.
Isomeric states in ^{253}No and ^{253}Fm .
European Physical Journal A, 47, 2011.
- [194] E.D. Donets, V.A. Shchegolev, and V.A. Ermakov.
Reactions involving evaporation of several neutrons on bombardment of $\text{U}238$ by accelerated ions of ^{18}O , ^{19}F , and ^{22}Ne .
Sov. J. Nucl. Phys., 2:723, 1966.
- [195] S. Raeder, M. Block, P. Chhetri, R. Ferrer, S. Kraemer, T. Kron, M. Laatiaoui, S. Nothhelfer, F. Schneider, P. Van Duppen, M. Verlinde, E. Verstraelen, Th. Walther, and A. Zadvornaya.
A gas-jet apparatus for high-resolution laser spectroscopy on the heaviest elements at SHIP.
Nuclear Instruments and Methods in Physics Research Section B: Beam Interactions with Materials and Atoms, 463:272–276, 2020.
- [196] R Ferrer, A Barzakh, B Bastin, R Beerwerth, M Block, Philip Creemers, H Grawe, Ruben de Groote, P Delahaye, X Fléchar, S. Franco, S. Fritzsche, L. P. Gaffney, L. Ghys, W. Gins, C. Granados, R. Heinke, L. Hijazi, M. Huyse, T. Kron, Yu. Kudryavtsev, M. Laatiaoui, N. Lecesne, M. Loiselet, F. Lutton, I. D. Moore, Y. Martínez, E. Mogilevskiy, P. Naubereit, J. Piot, S. Raeder, S. Rothe, H. Savajols, S. Sels, V. Sonnenschein, J-C Thomas, E. Traykov, C. Van Beveren, P. Van den Bergh, P. Van Duppen, K. Wendt, and A. Zadvornaya.
Towards high-resolution laser ionization spectroscopy of the heaviest elements in supersonic gas jet expansion.

BIBLIOGRAPHY

- Nature communications*, 8(1):14520, 2017.
- [197] A. Berger, J. Billowes, J. Das, S. Dutta, G. Gwinner, C.H. Holbrow, T. Köhl, T. Lauritsen, S.L. Rolston, J. Schecker, G.D. Sprouse, and F. Xu.
A resonance cell for on-line optical spectroscopy of accelerator produced radioactive atoms.
Nuclear Instruments and Methods in Physics Research Section A: Accelerators, Spectrometers, Detectors and Associated Equipment, 311(1):224–239, 1992.
- [198] JR Beene, CE Bemis Jr, JP Young, and SD Kramer.
Study of the fission isomer ^{240m}Am (SF) using laser-induced nuclear polarization.[Cross section of ^{238}U (^7Li , $5n$) at 48 MeV].
Technical report, Oak Ridge National Lab., TN (USA), 1980.
- [199] H. Backe, K. Eberhardt, R. Feldmann, M. Hies, H. Kunz, W. Lauth, R. Martin, H. Schöpe, P. Schwamb, M. Sewtz, P. Thörle, N. Trautmann, and S. Zauner.
A compact apparatus for mass selective resonance ionization spectroscopy in a buffer gas cell.
Nuclear Instruments and Methods in Physics Research Section B: Beam Interactions with Materials and Atoms, 126(1):406–410, 1997.
International Conference on Electromagnetic Isotope Separators and Techniques Related to Their Applications.
- [200] T.E. Cocolios, R.P. de Groote, J. Billowes, M.L. Bissell, I. Budinčević, T. Day Goodacre, G.J. Farooq-Smith, V.N. Fedosseev, K.T. Flanagan, S. Franchoo, R.F. Garcia Ruiz, W. Gins, H. Heylen, T. Kron, R. Li, K.M. Lynch, B.A. Marsh, G. Neyens, R.E. Rossel, S. Rothe, A.J. Smith, H.H. Stroke, K.D.A. Wendt, S.G. Wilkins, and X. Yang.
High-resolution laser spectroscopy with the Collinear Resonance Ionisation Spectroscopy (CRIS) experiment at CERN-ISOLDE.
Nuclear Instruments and Methods in Physics Research Section B: Beam Interactions with Materials and Atoms, 376:284–287, 2016.
Proceedings of the XVIIth International Conference on Electromagnetic Isotope Separators and Related Topics (EMIS2015), Grand Rapids, MI, U.S.A., 11-15 May 2015.
- [201] C. Y. Chen, Y. M. Li, K. Bailey, T. P. O’Connor, L. Young, and Z.-T. Lu.
Ultrasensitive isotope trace analyses with a Magneto-Optical Trap.
Science, 286(5442):1139–1141, 1999.
- [202] C. J. Campbell, A. G. Radnaev, and A. Kuzmich.
Wigner crystals of ^{229}Th for optical excitation of the nuclear isomer.
Phys. Rev. Lett., 106:223001, Jun 2011.
- [203] Giorgio Visentin, Mustapha Laatiaoui, Larry A Viehland, and Alexei A Buchachenko.

BIBLIOGRAPHY

- Mobility of the singly-charged lanthanide and actinide cations: Trends and perspectives.
Frontiers in Chemistry, 8:438, 2020.
- [204] Elisa Romero Romero, Michael Block, Biswajit Jana, Eunkang Kim, Steven Nothhelfer, Sebastian Raeder, Harry Ramanantoanina, Elisabeth Rickert, Jonas Schneider, Philipp Sikora, et al.
A progress report on Laser Resonance Chromatography.
Atoms, 10(3):87, 2022.
- [205] Robert Eichler, NV Aksenov, AV Belozarov, GA Bozhikov, VI Chepigin, SN Dmitriev, R Dressler, HW Gäggeler, VA Gorshkov, Florian Haenssler, M. G. Itkis, A. Laube, V. Ya. Lebedev, O. N. Malyshev, Yu. Ts. Oganessian, O. V. Petrushkin, D. Piguet, P. Rasmussen, S. V. Shishkin, A. V. Shutov, A. I. Svirikhin, E. E. Tereshatov, G. K. Vostokin, M. Wegrzecki, and A. V. Yereimin.
Chemical characterization of element 112.
Nature, 447(7140):72–75, 2007.
- [206] Alexander Yakushev, Jacklyn M. Gates, Andreas Türler, Matthias Schädel, Christoph E. Düllmann, Dieter Ackermann, Lise-Lotte Andersson, Michael Block, Willy Bröchle, Jan Dvorak, Klaus Eberhardt, Hans G. Essel, Julia Even, Ulrika Forsberg, Alexander Gorshkov, Reimar Graeger, Kenneth E. Gregorich, Willi Hartmann, Rolf-Dietmar Herzberg, Fritz P. Heßberger, Daniel Hild, Annett Hübner, Egon Jäger, Jadambaa Khuyagbaatar, Birgit Kindler, Jens V. Kratz, Jörg Krier, Nikolaus Kurz, Bettina Lommel, Lorenz J. Niewisch, Heino Nitsche, Jon Petter Omtvedt, Edward Parr, Zhi Qin, Dirk Rudolph, Jörg Runke, Brigitta Schausten, Erwin Schimpf, Andrey Semchenkov, Jutta Steiner, Petra Thörle-Pospiech, Juha Uusitalo, Maciej Wegrzecki, and Norbert Wiehl.
Superheavy element flerovium (element 114) is a volatile metal.
Inorganic Chemistry, 53(3):1624–1629, 2014.
PMID: 24456007.
- [207] S Fritzsche.
Large-scale accurate structure calculations for open-shell atoms and ions.
Physica Scripta, 2002(T100):37, Jan 2002.
- [208] A Türler.
Gas phase chemistry experiments with transactinide elements.
Radiochimica Acta, 72(1):7–18, 1996.
- [209] Matthias Schädel.
Aqueous chemistry of transactinides.
Radiochimica Acta, 89(11-12):721–728, 2001.
- [210] H.W. Ellis, E.W. McDaniel, D.L. Albritton, L.A. Viehland, S.L. Lin, and E.A. Mason.

BIBLIOGRAPHY

- Transport properties of gaseous ions over a wide energy range. Part II.
Atomic Data and Nuclear Data Tables, 22(3):179–217, 1978.
- [211] Yueyang Zhong, Suk-Joon Hyung, and Brandon T Ruotolo.
Ion mobility–mass spectrometry for structural proteomics.
Expert Review of Proteomics, 9(1):47–58, 2012.
PMID: 22292823.
- [212] Rainer A Dressler, Johannes PM Beijers, Henning Meyer, Stephen M Penn,
Veronica M Bierbaum, and Stephen R Leone.
Laser probing of ion velocity distributions in drift fields: Parallel and per-
pendicular temperatures and mobility for Ba⁺ in He.
The Journal of chemical physics, 89(8):4707–4715, 1988.
- [213] Paul R. Kemper Manuel J. Manard.
Reduced mobilities of lanthanide cations measured using high-resolution
ion mobility mass spectrometry with comparisons between experiment
and theory.
International Journal of Mass Spectrometry, 412(14):14–19, 2017.
- [214] Yehia Ibrahim, Edreese Alsharaeh, Ridha Mabrouki, Paul Momoh, Enli
Xie, and M. Samy El-Shall.
Ion mobility of ground and excited states of laser-generated transition metal
cations.
The Journal of Physical Chemistry A, 112(6):1112–1124, 2008.
PMID: 18205338.
- [215] GT Seaborg.
The chemical and radioactive properties of the heavy elements.
Chem. Eng. News, 23:2190, 1945.
- [216] Manuel J. Manard and Paul R. Kemper.
Reduced mobilities of lanthanide cations measured using high-resolution
ion mobility mass spectrometry with comparisons between experiment
and theory.
International Journal of Mass Spectrometry, 412:14–19, 2017.
- [217] Alexei A. Buchachenko and Larry A. Viehland.
Mobility of singly-charged lanthanide cations in rare gases: Theoretical
assessment of the state specificity.
The Journal of Chemical Physics, 140(11):114309, 2014.
- [218] Achim Dretzke.
*Untersuchungen zu ionenchemischen Reaktionen und Mobilitätsmessungen
an schweren Elementen in einer Puffergaszelle.*
PhD thesis, Johannes Gutenberg-Universität Mainz, 2003.
- [219] H Backe, A Dretzke, R Horn, T Kolb, W Lauth, R Repnow, M Sewtz, and
N Trautmann.

BIBLIOGRAPHY

- Ion mobility measurements and ion chemical reaction studies at heavy elements in a buffer gas cell.
In *Laser 2004*, pages 77–84. Springer, 2006.
- [220] Gary L Glish and Richard W Vachet.
The basics of mass spectrometry in the twenty-first century.
Nature reviews drug discovery, 2(2):140–150, 2003.
- [221] Raymond E. March and John F. J. Todd.
Quadrupole Ion Trap Mass Spectrometry, Volume 165, Second Edition.
John Wiley Sons, Inc., 2005.
- [222] Jonas Schneider.
Entwicklungen für Ionenmobilitätsspektroskopie an Aktiniden, 2019.
- [223] Wolfgang R. Plaß, Timo Dickel, and Christoph Scheidenberger.
Multiple-reflection time-of-flight mass spectrometry.
International Journal of Mass Spectrometry, 349-350:134–144, 2013.
100 years of Mass Spectrometry.
- [224] G. Münzenberg.
Development of mass spectrometers from Thomson and Aston to present.
International Journal of Mass Spectrometry, 349-350:9–18, 2013.
100 years of Mass Spectrometry.
- [225] Klaus Blaum.
High-accuracy mass spectrometry with stored ions.
Physics Reports, 425(1):1–78, 2006.
- [226] Dr. Sjuts Optotechnik GmbH.
<http://www.sjuts.com>, 2022.
- [227] Balzers.
Quadrupol-Massenspektrometer QMS 311, Betriebsanweisung (BK800013BD), Tech. rep.
Balzers AG, FL-9496 Balzers, Fürstentum Liechtenstein.
- [228] P.R. Kemper and M.T. Bowers.
A hybrid double-focusing mass spectrometer-high-pressure drift reaction cell to study thermal energy reactions of mass-selected ions.
J. Am. Soc. Mass Spectrom., 1:197–207, 1990.
- [229] Ch. Icedman et al.
Ion Mobility Studies of Electronically Excited States of Atomic Transition Metal Cations: Development of an Ion Mobility Source for Guided Ion Beam Experiments.
J. Am. Soc. Mass Spectrom., 18:1196, 2007.
- [230] Continuum.
Continuum Powerlite Precision II 9000 Data Sheet.
2004.

BIBLIOGRAPHY

- [231] GWU-Lasertechnik Vertriebsgesellschaft mbH.
Data Sheet: VisIR2.
2000.
- [232] Georg A. Reider.
Photonik - Eine Einführung in die Grundlagen, 3. Auflage.
Springer-Verlag Wien, 2012.
- [233] A. Clark.
Laser driven resonance ionisation of ytterbium.
HGS-HIRE Summer Student Program, Book of Reports, 2014.
- [234] K. Eberhardt, Ch. E. Düllmann, R. Haas, Ch. Mokry, J. Runke, P. Thörle-Pospiech, and N. Trautmann.
Actinide targets for fundamental research in nuclear physics.
AIP Conference Proceedings, 1962(1):030009, 2018.
- [235] N. Trautmann and H. Folger.
Preparation of actinide targets by electrodeposition.
Nuclear Instruments and Methods in Physics Research Section A: Accelerators, Spectrometers, Detectors and Associated Equipment, 282(1):102–106, 1989.
- [236] R. Haas, S. Lohse, Ch.E. Düllmann, K. Eberhardt, C. Mokry, and J. Runke.
Development and characterization of a Drop-on-Demand inkjet printing system for nuclear target fabrication.
Nuclear Instruments and Methods in Physics Research Section A: Accelerators, Spectrometers, Detectors and Associated Equipment, 874:43–49, 2017.
- [237] Danny Münzberg.
private communication.
- [238] FP Hessberger.
Gsi experiments on synthesis and nuclear structure investigations of the heaviest nuclei.
The European Physical Journal D, 45:33–37, 2007.
- [239] A Borschevsky, E Eliav, MJ Vilkas, Y Ishikawa, and U Kaldor.
Transition energies of atomic lawrencium.
The European Physical Journal D, 45(1):115–119, 2007.
- [240] E. V. Kahl, S. Raeder, E. Eliav, A. Borschevsky, and J. C. Berengut.
Ab initio calculations of the spectrum of lawrencium.
Phys. Rev. A, 104:052810, Nov 2021.
- [241] V. A. Dzuba, M. S. Safronova, and U. I. Safronova.
Atomic properties of superheavy elements no, lr, and rf.
Phys. Rev. A, 90:012504, Jul 2014.
- [242] S Fritzsche, CZ Dong, F Koike, and A Uvarov.

BIBLIOGRAPHY

- The low-lying level structure of atomic lawrencium ($Z=103$): energies and absorption rates.
The European Physical Journal D, 45:107–113, 2007.
- [243] Harry Ramanantoanina, Anastasia Borschevsky, Michael Block, and Mustapha Laatiaoui.
Electronic structure of Rf^+ ($Z=104$) from ab initio calculations.
Phys. Rev. A, 104:022813, Aug 2021.
- [244] G. Bortels and P. Collaers.
Analytical function for fitting peaks in alpha-particle spectra from Si detectors.
International Journal of Radiation Applications and Instrumentation. Part A. Applied Radiation and Isotopes, 38(10):831–837, 1987.
- [245] M. Sewtz.
Entwicklung eines HF-Quadrupols für ein Ionentransportsystem, 1997.
- [246] W. Paul and M. Raether.
Das elektrische Massenfilter.
Rev. Mod. Phys., 140:262–273, 1955.
- [247] Wolfgang Paul.
Electromagnetic traps for charged and neutral particles.
Rev. Mod. Phys., 62:531–540, 1990.
- [248] G. Werth F. Major, V. Gheorghe.
Charged Particle Traps.
Springer-Verlag Berlin Heidelberg New York, 2005.
- [249] H. Schöpe.
Entwicklung eines Systems zum massenselektiven Nachweis von Ionen nach Resonanzionisation in einer Puffergaszelle, 1992.
- [250] P. Schwamb.
Entwicklung eines Detektors zum direkten massenselektiven Ionennachweis nach Resonanzionisationspektroskopie in einer Puffergaszelle.
PhD thesis, Johannes Gutenberg-Universität Mainz, Institut für Kernphysik, 1996.
- [251] S. Young J. Sansonetti, W. Martin.
Handbook of basic atomic spectroscopic data.
2009.

Acknowledgments

personal data

Publications

- 2022 Warbinek, Jessica, et al., *Advancing Radiation-Detected Resonance Ionization towards Heavier Elements and More Exotic Nuclides*, *Atoms* 10.2 (2022): 41.
- 2022 Romero Romero, Elisa, et al., *A progress report on Laser Resonance Chromatography*, *Atoms* 10.3 (2022): 87.
- 2020 E. Rickert et al., *Ion Mobilities for Heaviest Element Identification* *Hyperfine Interactions*, 241 (2020): 1-8.

Conferences, Schools and Trainings

personal data

personal data

Curriculum Vitae

personal data

personal data

personal data

personal data